Government of Western Australia

Department of
Mines and Petroleum

REPORT
146

PRESSURE–TEMPERATURE–TIME EVOLUTION OF THE MUTHERBUKIN TECTONIC EVENT, CAPRICORN OROGEN

by FJ Korhonen, SP Johnson, IR Fletcher, B Rasmussen, S Sheppard, JR Muhling, DJ Dunkley, MTD Wingate, MP Roberts, and CL Kirkland

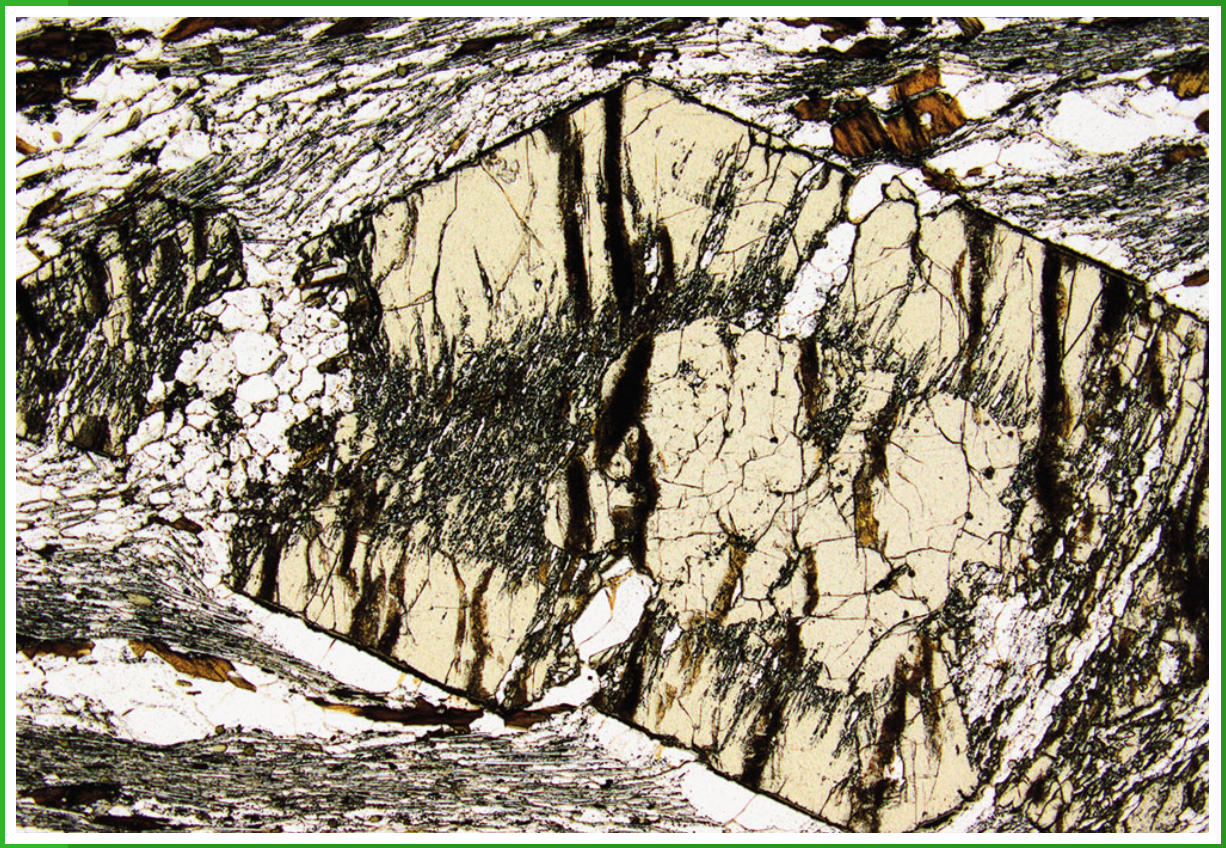

Geological Survey of Western Australia

Government of **Western Australia**
Department of **Mines and Petroleum**

REPORT 146

PRESSURE–TEMPERATURE–TIME EVOLUTION OF THE MUTHERBUKIN TECTONIC EVENT, CAPRICORN OROGEN

by
FJ Korhonen, SP Johnson, IR Fletcher[1], B Rasmussen[1], S Sheppard[1], JR Muhling[1,2], DJ Dunkley[1], MTD Wingate, MP Roberts[2], CL Kirkland[1]

1 Department of Applied Geology, Curtin University, GPO Box U1987, Perth WA 6845

2 Centre for Microscopy, Characterisation and Analysis, The University of Western Australia, 35 Stirling Highway, Crawley WA 6009

Perth 2015

Geological Survey of Western Australia

REFERENCE
The recommended reference for this publication is:
Korhonen, FJ, Johnson, SP, Fletcher IR, Rasmussen, B, Sheppard, S, Muhling, JR, Dunkley, DJ, Wingate, MTD, Roberts, MP, Kirkland, CL 2015, Pressure–temperature–time evolution of the Mutherbukin Tectonic Event, Capricorn Orogen: Geological Survey of Western Australia, Report 146, 64p.

National Library of Australia Cataloguing-in-Publication entry:

Creator:	Korhonen, F. J., author.
Title:	Pressure–temperature–time evolution of the Mutherbukin Tectonic Event: a model for Mesoproterozoic intraplate reworking of the Capricorn Orogen
ISBN:	9781741686074 (ebook)
Series:	Report (Geological Survey of Western Australia) ; 146.
Subjects:	Geology--Western Australia--Gascoyne Region. Geological surveys--Western Australia--Gascoyne Region.
Other Authors/Contributors:	Johnson, S. P., author. Fletcher, I. R., author. Rasmussen, Birger, author. Sheppard, S., author. Muhling, J. R. (Janet R.), author. Dunkley. D. J., author. Wingate, M. T. D. (Michael Thomas David), author. Roberts. M. P., author. Kirkland, C. L., author. Geological Survey of Western Australia, issuing body.
Dewey Decimal Classification:	559.41

ISSN 1834–2280

U–Th–Pb measurements were conducted using the SHRIMP II ion microprobes at the John de Laeter Centre of Isotope Research at Curtin University in Perth, Australia. The authors acknowledge the facilities, and the scientific and technical assistance of the Australian Microscopy & Microanalysis Research Facility at the Centre for Microscopy, Characterisation and Analysis, The University of Western Australia, a facility funded by the university, and state and Commonwealth governments.

EXPLORATION INCENTIVE SCHEME

John de Laeter Centre
Isotope Research for the Earth and Environment

Curtin University

The University of Western Australia
Achieving International Excellence

Grid references in this publication refer to the Geocentric Datum of Australia 1994 (GDA94). Locations mentioned in the text are referenced using Map Grid Australia (MGA) coordinates, Zone 50. All locations are quoted to at least the nearest 100 m.

Copy editor: K Coyle
Cartographer: M Prause
Desktop publisher: RL Hitchings
Printed by Images on Paper, Perth, Western Australia

Published 2015 by Geological Survey of Western Australia
This Report is published in digital format (PDF) and is available online at <www.dmp.wa.gov.au/GSWApublications>.

Further details of geological publications and maps produced by the Geological Survey of Western Australia are available from:
Information Centre | Department of Mines and Petroleum | 100 Plain Street | EAST PERTH | WESTERN AUSTRALIA 6004
Telephone: +61 8 9222 3459 Facsimile: +61 8 9222 3444 **www.dmp.wa.gov.au/GSWApublications**

Cover photograph: Photomicrograph of staurolite-bearing semipelitic schist from the Nick Belt, under plane polarized light. Field of view is 5 mm. Euhedral porphyroblast of staurolite (pale yellow) showing an irregular inclusion-free core surrounded by a thick inclusion-rich rim within a fine-grained matrix of quartz, muscovite and minor biotite.

Contents

Appendices

Figures

Tables

Pressure–temperature–time evolution of the Mutherbukin Tectonic Event, Capricorn Orogen

by

FJ Korhonen, SP Johnson, IR Fletcher[1], B Rasmussen[1], S Sheppard[1], JR Muhling[1,2], DJ Dunkley[1], MTD Wingate, MP Roberts[2], CL Kirkland[1]

Abstract

The Mutherbukin Tectonic Event represents a protracted period of Mesoproterozoic reworking of the Capricorn Orogen and offers significant insight into the tectonic drivers and heat sources during the evolution of long-lived intraplate orogens and their relationships with mineral systems. Mineral assemblages and tectonic fabrics related to this event occur within a 50 km-wide fault-bound corridor in the central part of the Gascoyne Province. This zone preserves a crustal profile, with greenschist facies rocks in the north grading to upper amphibolite facies rocks in the south. Upper crustal rocks across the region also record evidence for faulting and hydrothermal fluid flow at this time, including zones of mineralization. The earliest event in some samples pre-dates the Mutherbukin Tectonic Event and records high-temperature, low-pressure contact metamorphism related to emplacement of Paleoproterozoic granites. However, sensitive high resolution ion microprobe (SHRIMP) U–Pb dating of accessory phases, integrated with phase equilibria modelling and garnet chemistry, reveals a dominant history of prolonged transpression and crustal thickening between c. 1320 and 1270 Ma. The thermal effects of this event persisted for up to 100 Ma, with estimates of peak metamorphism defining an apparent thermal gradient of 45°C km^{-1}. The absence of Mutherbukin-aged magmatism is consistent with residual lithologies at depth. The heat source was primarily thickening of radiogenic crust, and peak metamorphism was terminated by transtension and crustal thinning from c. 1210 to 1170 Ma. Samples from a narrow fault-bound lens within Paleoproterozoic granites preserve a polyphase evolution, characterized by punctuated cycles of Mesoproterozoic crustal thickening and thinning. The contrasting pressure–temperature–time histories in different parts of the orogen suggest that parts of the crust were decoupled during the Mutherbukin Tectonic Event. Fluid flow and hydrothermal alteration in the upper crust was synchronous with these deformation and metamorphic events, indicating a strong, dynamic link between events in the middle and upper crust. These relationships are critical for understanding mineral systems in the province and for constraining where and when mineral deposits might form.

KEYWORDS: garnet zoning, geochronology, intraplate reworking, metamorphism, phase equilibria modelling, structural geology, thermal modelling

1 Department of Applied Geology, Curtin University, GPO Box U1987, Perth WA 6845

2 Centre for Microscopy, Characterisation and Analysis, The University of Western Australia, 35 Stirling Highway, Crawley WA 6009

Introduction

The Capricorn Orogen in central Western Australia is one of the longest-lived intraplate systems in the world, but the tectonic drivers and heat sources contributing to its prolonged evolution are not well understood. The orogen records the assembly of the Archean Pilbara and Yilgarn Cratons with the Glenburgh Terrane to form the West Australian Craton (Fig. 1; Tyler and Thorne, 1990; Cawood and Tyler, 2004; Occhipinti et al., 2004; Sheppard et al., 2010a, b; Johnson et al., 2011c, 2013b; Johnson, 2013). The amalgamation occurred during the 2215–2145 Ma Ophthalmian and 2005–1950 Ma Glenburgh Orogenies (Occhipinti et al., 2004; Sheppard et al., 2010b; Johnson et al., 2011c, 2013b), and was followed by one billion years of episodic continental reworking and reactivation (Sheppard et al., 2010b; Johnson et al., 2013b). Each of these events can provide important insight into the prolonged evolution of an intraplate orogen and its relationship with mineral systems.

The orogen includes the deformed margins of the Pilbara and Yilgarn Cratons, granitic and medium- to high-grade metamorphic rocks of the Gascoyne Province, and numerous variably deformed Proterozoic sedimentary basins, including the Mesoproterozoic Edmund and Collier Basins that unconformably overlie the province. Based on the distribution of reworking events, the Gascoyne Province has been divided into several east–southeasterly trending structural and metamorphic domains, or zones (Fig. 2; Sheppard et al., 2010b), each of which is characterized by a distinct geological history. These crustal zones are bounded by major faults or shear zones, but none is interpreted to be an exotic terrane. Rather, each zone reflects a different response to the multiple reworking events that distinguish the Gascoyne Province from other units in the Capricorn Orogen (Sheppard et al., 2010b). Building on the current program of remapping in the Gascoyne Province by the Geological Survey of Western Australia (GSWA), including U–Pb zircon and phosphate geochronology and detailed geophysical surveys across the orogen (Johnson et al., 2011a; 2013b; Dentith et al., 2014), the Gascoyne Province provides an ideal natural laboratory to investigate reworking of a long-lived intraplate orogen.

The oldest reworking events in the Gascoyne Province include the 1820–1770 Ma Capricorn Orogeny (Sheppard et al., 2010a) and the 1680–1620 Ma Mangaroon Orogeny (Sheppard et al., 2005), both of which are characterized by widespread deformation, regional metamorphism, and granite magmatism. Following these orogenic events, the subsequent reworking episodes resulted in deformation, metamorphism, and sedimentation, with little or no magmatism (Sheppard et al., 2010b). These events include the Mesoproterozoic Mutherbukin Tectonic Event (1320–1170 Ma), the Neoproterozoic Edmundian Orogeny (1030–955 Ma), and the c. 570 Ma Mulka Tectonic Event. Although the Capricorn Orogen has experienced several reworking events, it is the later Mesoproterozoic Mutherbukin Tectonic Event that provides significant insight into the potential for radiogenic heating as a driving force for intraplate reworking because there is no widespread magmatism and no evidence for an elevated mantle contribution to the crustal thermal gradient at that time.

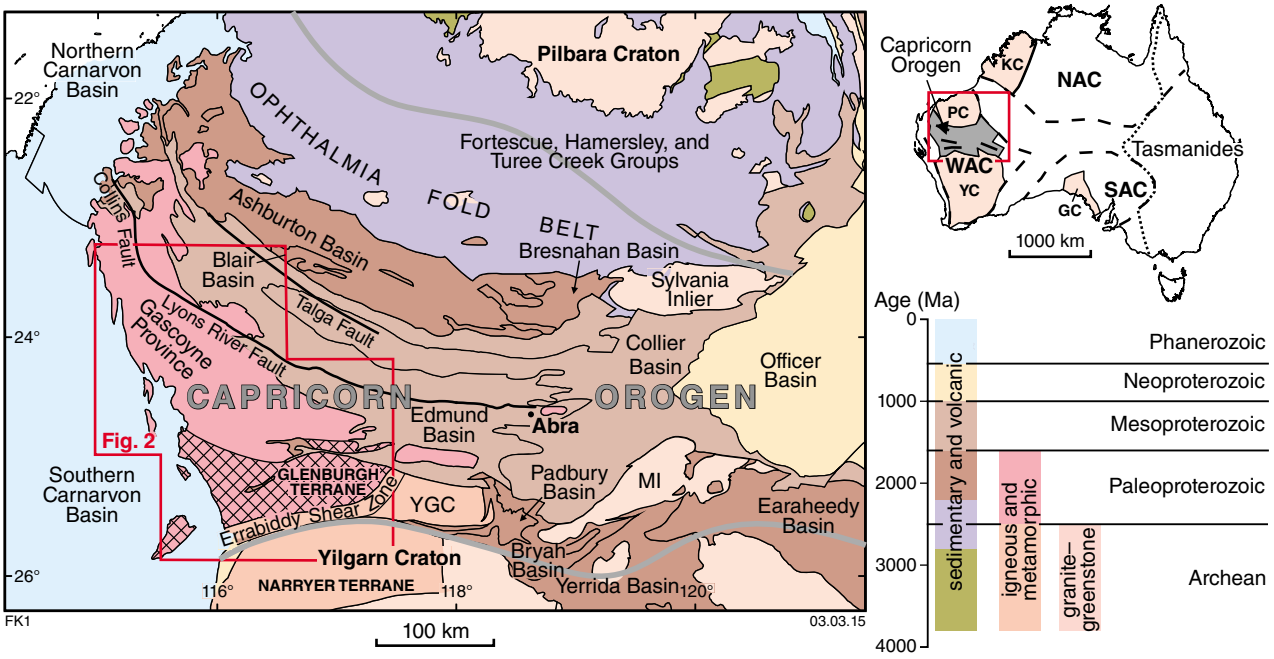

Figure 1. **Elements of the Capricorn Orogen and surrounding cratons and basins; modified from Sheppard et al. (2010a) and Martin and Thorne (2004). Inset shows location of the Capricorn Orogen, Paleoproterozoic (NAC = North Australian Craton; SAC = South Australian Craton; WAC = West Australian Craton; KC = Kimberley Craton), and Archean (YC = Yilgarn Craton; PC = Pilbara Craton; GC = Gawler Craton) crustal elements. Other abbreviations: YGC = Yarlarweelor Gneiss Complex; MI = Marymia Inlier; modified from Myers et al. (1996)**

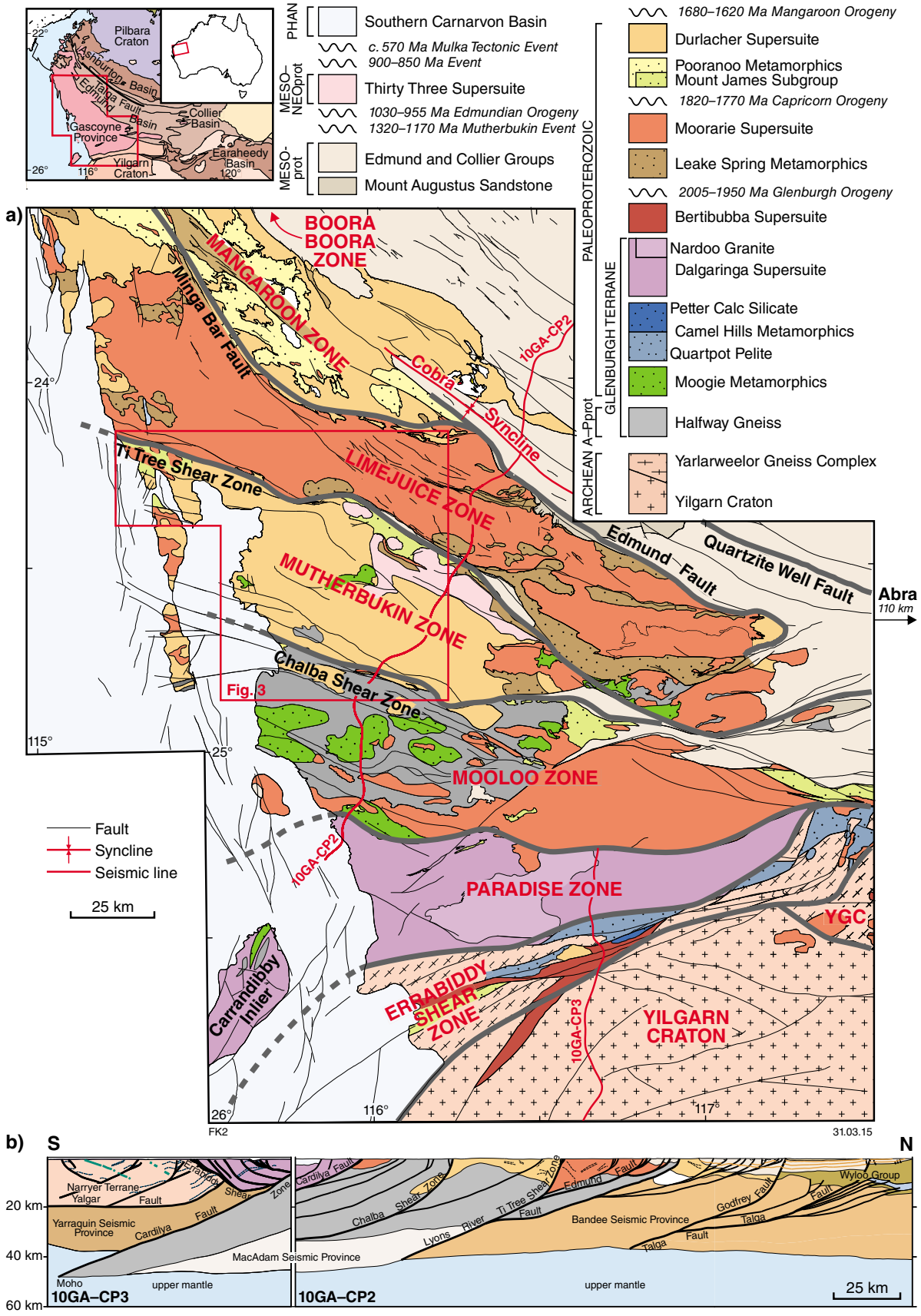

Figure 2. **Geology of the Gascoyne Province: a) Simplified geologic map showing division of the region into structural–metamorphic zones; b) geological cross-section through the Gascoyne Province, combining deep crustal seismic lines 10GA–CP2 and 10GA–CP3 (Johnson et al., 2013b). Abbreviation: YGC = Yarlarweelor Gneiss Complex**

The Mutherbukin Tectonic Event is best preserved in the central part of the Gascoyne Province (Mutherbukin Zone; Figs 2 and 3), although low-grade metamorphism and hydrothermal activity of this age have also affected parts of the overlying Mesoproterozoic Edmund Group (Rasmussen et al., 2010a; Pirajno et al., 2010; Johnson et al., 2011d; Zi et al., 2015). This event represents a protracted period of intraplate reactivation. However, understanding the significance and tectonic setting of the event has been complicated by a number of factors, including: 1) a broad spread of Mesoproterozoic dates of unknown geologic significance ranging from c. 1320 to 1170 Ma from low- to medium-grade metasedimentary and meta-igneous units; 2) the difficulty in defining the precise distribution of Mutherbukin-aged fabrics and faults because they are indistinguishable from coaxial structures, particularly fabrics formed during the 1030–955 Ma Edmundian Orogeny (Sheppard et al., 2007); and 3) a lack of information regarding kinematics and the pressure (*P*)–temperature (*T*) conditions of metamorphism.

In this study, sensitive high resolution ion microprobe (SHRIMP) U–Th–Pb age data from monazite, xenotime, and zircon are reported from several localities in the Mutherbukin Zone. The monazite and xenotime age data are retrieved from grains individually selected from thin sections so that the results can be integrated with quantitative phase equilibria modelling and garnet chemistry. The results are also compared with recent age data constraints for deformation and hydrothermal alteration in the upper crustal rocks, including zones of mineralization. The integrated data are used to assess the overall *P*–*T*–time (*t*) evolution of the Mutherbukin Tectonic Event and to provide an estimate of the evolving thermal gradient of the crust during orogenesis. A model is proposed for the heat sources of metamorphism and tectonic driving forces of the event. These constraints are also critical for understanding the timing and generation of hydrothermal or metamorphic fluids in the deep crust and their transport to the upper crust where, in a mineral systems setting (Wyborn et al., 1994; McCuaig and Hronsky, 2014), they may play an important role in mineralization or remobilization of pre-existing mineral deposits.

Mutherbukin Zone

In the Gascoyne Province, metamorphic mineral assemblages and tectonic fabrics related to the Mutherbukin Tectonic Event occur within a 50 km-wide corridor, bounded to the north by the Ti Tree Shear Zone and to the south by the Chalba Shear Zone (Johnson et al., 2011a; 2013b). These south-dipping, crustal-scale structures delineate the margins of the Mutherbukin Zone, and separate it from the older Limejuice Zone to the north and the Mooloo Zone to the south (Fig. 2).

The Mutherbukin Zone is dominated by late Paleoproterozoic granites of the Davey Well batholith, part of the 1680–1620 Ma Durlacher Supersuite. The majority of the batholith is made up of the 1670–1648 Ma Davey Well Granite. Isolated lenses of metasedimentary schist, part of the 1840–1810 Ma Leake Spring Metamorphics (Sheppard et al., 2010b), are exposed along a northwest-trending belt ~65 km long and 10 km wide within the batholith (Fig. 3a). The largest exposure of schist is ~20 km long and 5 km wide in the western part of the Mutherbukin Zone, which is referred to as the 'Nick Belt' (Williams, 1985). The schists show a gradational change in metamorphic assemblages across the axis of the belt, with magnetite-bearing schists in the north grading to andalusite-bearing schists, and garnet- and staurolite-bearing schists in the south. These differences in metamorphic assemblages have been interpreted to reflect an increasing degree of metamorphism toward the south (e.g. Johnson et al., 2011a), away from the Ti Tree Shear Zone. Lenses of very low grade sedimentary rocks of the 1680–1455 Ma Edmund Group along the Ti Tree Shear Zone in the central and eastern parts of the Mutherbukin Zone ('Ti Tree Syncline'; Fig. 3a) are also consistent with this interpretation. In the southern part of the Mutherbukin Zone, upper amphibolite facies granitic gneisses of the Durlacher Supersuite locally preserve evidence for in situ melting.

Deep crustal seismic imaging shows that the Davey Well batholith ranges in thickness from ~1.8 km in the centre of the Mutherbukin Zone to ~11.5 km at its northern contact where it is truncated by the Ti Tree Shear Zone (Fig. 2b; Johnson et al., 2011a; 2013b). The batholith has a concave basal contact with the underlying basement, inferred to be part of the Glenburgh Terrane, the oldest exposed crust in the Gascoyne Province (e.g. Occhipinti et al., 2004; Sheppard et al., 2004; Johnson et al., 2010, 2011e). This shape suggests that it has been folded during the Mutherbukin Tectonic Event. Based on the seismic survey, the Glenburgh Terrane extends to a depth of ~30 km in the Mutherbukin Zone, and the present-day Moho occurs at a depth of ~40–45 km (Fig. 2b; Korsch et al., 2011; Johnson et al., 2011a; 2013b).

Structural setting

The main expression of the Mutherbukin Tectonic Event in the Gascoyne Province is a strong subvertical schistosity in pelitic and semipelitic rocks of the Leake Spring Metamorphics, and a widely developed foliation or gneissic banding within metamorphosed granites. These steeply dipping fabrics trend east–southeast (Fig. 3b) and are coaxial with the main structural elements of the province. The metasedimentary schists and gneissic granites also contain a well-developed, shallow east-plunging mineral lineation that is parallel to the hinges of millimetre- to kilometre-scale shear-related folds (Fig. 3c).

In the Nick Belt, the lower grade schists carry a strong foliation (S_{1u}) defined by aligned muscovite blades and flattened quartz grains. A variably developed lineation (L_{1u}) is defined by 1–5 mm-long, elongate magnetite and andalusite porphyroblasts. Locally the L_{1u} lineation is overgrown by cm-scale, tabular andalusite porphyroblasts (now pseudomorphed by quartz and muscovite) which are either randomly oriented or parallel to a weak crenulation cleavage (S_{2u}). In higher strain zones, these porphyroblasts are partially flattened within a composite S_{1u}–S_{2u} fabric, showing sinistral (transtensional) shear sense movements

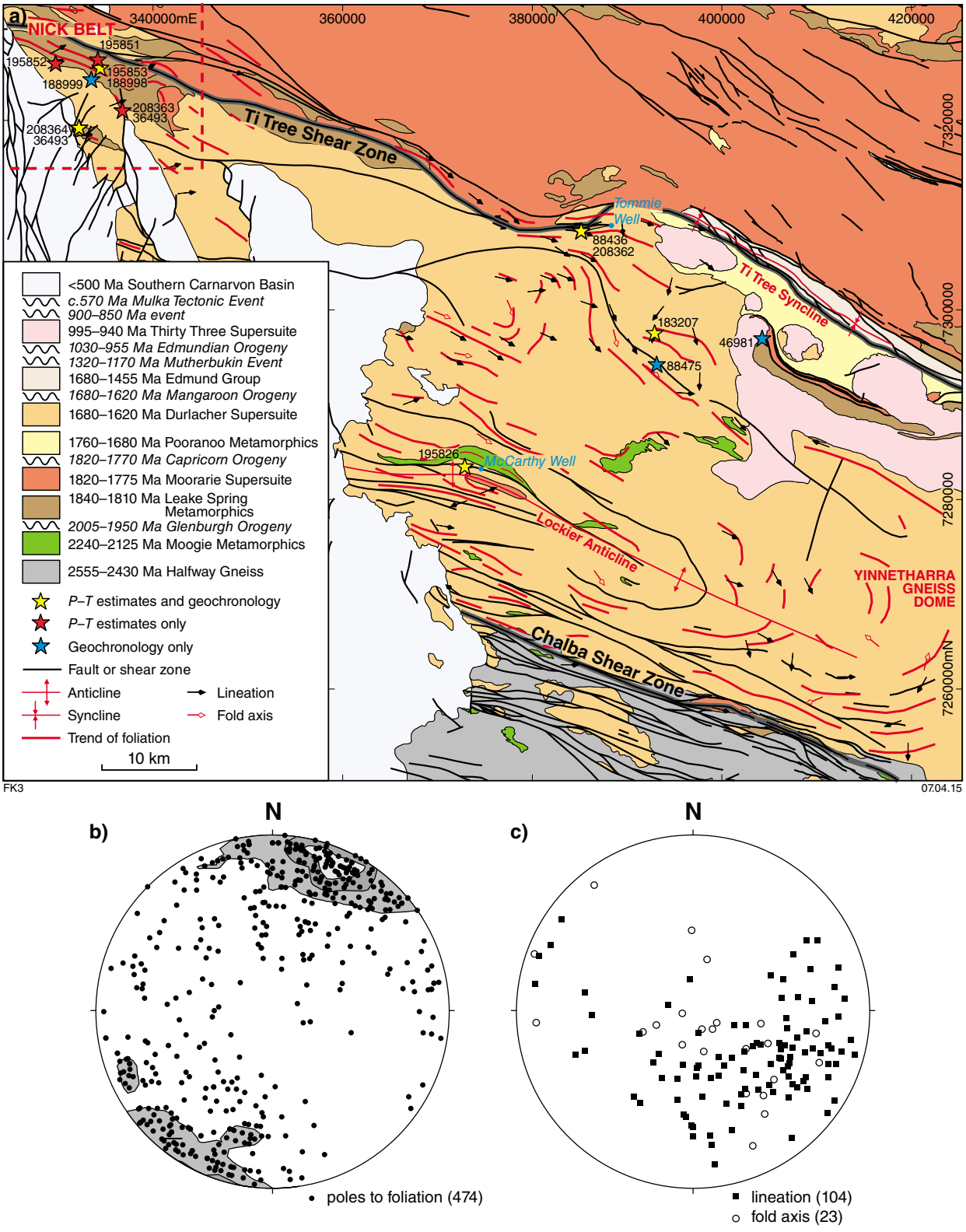

Figure 3. **Geology of the Mutherbukin Zone: a) Simplified geologic map of the Mutherbukin Zone. Stars show sample locations and type of analyses. Dashed box shows approximate limit of the Nick Belt; b) field data from the Mutherbukin Zone showing poles to foliation (n = 474); c) field data from the Mutherbukin Zone showing lineation (n = 104) and fold axes (n = 23)**

along a shallow east-plunging lineation (L_{2u}) that is parallel to the L_{1u} fabric. In the southern, higher grade part of the Nick Belt, the S_{1u}–L_{1u} fabric is overprinted by randomly oriented, coarse-grained staurolite and garnet porphyroblasts. Locally the main S_{1u} schistosity is preserved as inclusion trails within the porphyroblasts. Commonly the inclusion trails are curved so that toward the edges of the porphyroblasts they are parallel to the dominant, moderate to steeply south-dipping S_2 fabric (possibly S_{2u}). This implies that staurolite and garnet grew during progressive deformation; that is, S_1 and S_2 may represent a single event.

At Tommie Well (Fig. 3a), medium-grade metasedimentary schists and mafic amphibolites of the Leake Spring Metamorphics show a similar, but not identical, structural evolution to those in the southern part of the Nick Belt. In the schists, an early, steep S_1 fabric (possibly equivalent to S_{1u}) is preserved within randomly oriented staurolite or garnet porphyroblasts, or both. Locally the elongate staurolite porphyroblasts have been rotated subparallel to a weak- to moderately-developed crenulation cleavage (locally S_3). The amphibolites show a weak to moderate schistosity that is parallel with lithological contacts as well as with the main S_2 foliation in the schists. An early S_1 fabric at high angles to the main S_2 schistosity is locally preserved in the cores of 0.5–5 mm garnet porphyroblasts.

In the southwestern part of the Mutherbukin Zone, lithologies of the Davey Well batholith have been folded about a gently southeast-plunging regional-scale fold hinge. This structure forms the Lockier Anticline, a 45 km-long and 10 km-wide sheath fold (Fig. 3a), which is imaged in the deep crustal seismic data as a broad anticlinal structure (Fig. 2b; Johnson et al., 2011b; 2013b). It can be traced to the southeast where it is expressed as a broad dome about 30 km across, known as the 'Yinnetharra Gneiss Dome' (Williams, 1986). In the hinge zone of these structures, the rocks are strongly deformed and carry pervasive L to L–S fabrics, whereas in the limbs of the fold the rocks carry mostly S–L fabrics. Throughout the Mutherbukin Zone, all the linear fabrics (both L_{1u} and L_{2u}) are parallel to the fold hinge of the Lockier Anticline (Fig. 3a).

In the hinge zone of the Lockier Anticline around McCarthy Well (MGA 372898E 7283465N) on LOCKIER (Fig. 3a; Johnson et al., 2011b), the structural history is well preserved and the relative and absolute timing of fabric development can be constrained. Coarse-grained, porphyritic biotite-rich rocks of the Davey Well Granite have been strongly and heterogeneously deformed at high metamorphic grade. The earliest fabric preserved is an intense gneissic fabric (S_{1u}) which has flattened and sheared formerly round K-feldspar phenocrysts into flat, elongate lenses producing an intense, shallow east-plunging stretching lineation (L_{1u}). Associated sigma and delta shear sense indicators indicate dextral transpression (Fig. 4a), with regional-scale top-to-the-west transport. The S_{1u} gneissic fabric is truncated at a low to moderate angle by narrow, steeply-dipping extensional (or transtensional) shear zones (S_{2u}) that host small pockets and veins of massive biotite pegmatite (Fig. 4b). The biotite pegmatite veins commonly have diffuse contacts with the surrounding gneisses (Fig. 4c), and also form in extensional boudin necks (Fig. 4d) implying that they developed by melting of the granitic host in situ. Where the S_{2u} extensional fabric is well developed, it is coaxial with the S_{1u} gneissic fabric, forming a single composite fabric (S_{1u}–S_{2u}). Outcrops 500 m to the southwest (at MGA 372455E 7283333N) show evidence for a larger melt fraction; however, at this locality the S_{2u} leucocratic veins are openly folded with zones of former melt extraction parallel to the fold axial planes, suggesting that folding accompanied in situ melting. A further 20 m to the west, the S_{2u} leucocratic veins, which define an intense composite S_{1u}–S_{2u} gneissic fabric, are folded into a series of 10–25 cm-scale gently east-plunging sheath folds (F/L_{2u}). These observations indicate that high-grade metamorphism, melting and regional-scale sheath folding during D_{2u} transtension were all approximately coeval.

Sample descriptions

Fourteen samples were collected from 11 localities for geochronology or phase equilibria modelling. A sample summary is provided in Table 1; sample locations are shown in Figure 3a. The outcrop setting and petrography for each of the samples is described below. Although distinct fabrics may be described (e.g. S_1, S_2), these observations are only appropriate for individual samples, and may not relate to discrete deformation or metamorphic events or be directly comparable between samples.

Nick Belt

In the northern Nick Belt, north-dipping muscovite–chlorite schists contain mm- to cm-scale magnetite porphyroblasts defining a strong east-plunging lineation (GSWA 195851; Fig. 4e). Some layers also contain sparse cm-scale knots of former andalusite, now preserved as aggregates of muscovite–quartz, which are oriented orthogonal or oblique to the foliation and show evidence for dextral rotation (top to the west) within the foliation plane. The proportion of magnetite decreases and andalusite increases toward the south. In the central portion of the Nick Belt, andalusite-bearing schists locally contain a crenulation cleavage oriented parallel to the cm-scale andalusite porphyroblasts (GSWA 195853, 188998, 188999). These fabrics are orthogonal or oblique to the lineation defined by magnetite, where present (Fig. 4f). The andalusite porphyroblasts may also preserve inclusion trails that are broadly orthogonal to the main S_1 fabric. These trails indicate sinistral rotation (top to the east) during formation of the crenulation cleavage. A small lens of andalusite–garnet-bearing schist (GSWA 195852) occurs south of the andalusite-bearing schist, although this unit is not continuous along the length of the Nick Belt. The southern portion of the Nick Belt is characterized by the appearance of randomly oriented staurolite porphyroblasts, which may also contain fine-grained andalusite that define a moderate east-plunging lineation (GSWA 208363; Fig. 4g). An isolated lens of staurolite-bearing schist also occurs within

metamorphosed granites of the Davey Well Granite about 4 km to the south (Fig. 3a). This body is about 6 km long and 1 km wide, and represents the southernmost exposure of metasedimentary schist near the Nick Belt. The schists in this exposure contain muscovite, chlorite, abundant andalusite which defines an east-plunging lineation, variable amounts of randomly distributed garnet, and rare randomly oriented staurolite (GSWA 36493, 208364).

GSWA 195851: semipelitic schist, Nick Belt

Magnetite porphyroblasts up to 1.5 mm in size contain thin exsolution lamellae. The porphyroblasts are commonly flattened with quartz and chlorite pressure shadows (Fig. 5a). Some grains also show evidence of rotation. The peak metamorphic assemblage is inferred to be chlorite–muscovite–magnetite–quartz(–plagioclase–ilmenite).

GSWA 195852: semipelitic schist, Nick Belt

This sample contains a fine-grained matrix of chlorite–muscovite–biotite with thin elongate quartz stringers and flattened magnetite, which lack the exsolution lamellae observed in the other samples. Trace reddish-brown rutile is also observed. The groundmass commonly sweeps into quartz augen up to 5 mm in size, and the quartz stringers may be folded axial planar to the foliation in the groundmass (Fig. 5b). There are a few porphyroblasts of chlorite and magnetite, some showing evidence of rotation, and garnet porphyroblasts up to 3 mm. The garnet contains abundant fractures with chlorite (+ other very fine-grained phases) and iron oxide staining. There are also aligned inclusions of quartz(–magnetite) parallel to the fabric in the groundmass (Fig. 5c). The peak metamorphic assemblage is inferred to be garnet–chlorite–muscovite–biotite–magnetite–quartz(–rutile–plagioclase).

GSWA 195853, 188998: semipelitic schist, Nick Belt

Magnetite porphyroblasts up to 1 mm in size are also present in these samples. Quartz pressure shadows are most common, although a few magnetite porphyroblasts are mantled by chlorite. The samples also contain a few cm-sized chlorite(–muscovite) clots and aggregates of muscovite–quartz–chlorite–magnetite, in which chlorite and magnetite are minor phases. A relict of andalusite is preserved in one of these aggregates (Fig. 5d), consistent with the interpretation that the aggregates represent retrograde pseudomorphs after andalusite. These aggregates are commonly kinked, with chlorite and muscovite concentrated in the fold hinge. Small grains of ilmenite (sensu lato) are also observed in the matrix. The peak metamorphic assemblage in these samples is inferred to be chlorite–andalusite–muscovite–magnetite–ilmenite–quartz(–plagioclase).

GSWA 188999: semipelitic schist, Nick Belt

This sample contains larger polycrystalline quartz clasts and is less deformed than the other samples. Muscovite and chlorite define the foliation, with thin quartz seams commonly folded axial planar to the foliation. There are abundant small grains of hematite with exsolved ilmenite and lesser amounts of magnetite. These Fe–Ti oxides lack pressure shadows. There are also a few mm-sized clots of chlorite(–muscovite–quartz). Based on these observations, the peak metamorphic assemblage is inferred to be chlorite–muscovite–magnetite–ilmenite–quartz (–plagioclase).

GSWA 208363: staurolite schist, Nick Belt

This sample is characterized by euhedral staurolite porphyroblasts up to 1.5 cm long. The porphyroblasts contain abundant inclusions of quartz and rounded Fe–Ti oxides that are aligned at an oblique angle to, and truncated by, the external foliation which wraps around the staurolite porphyroblasts (Fig. 5e). Some staurolite porphyroblasts have rotated inclusion trails that can be followed into polycrystalline quartz stringers in the host (Fig. 5f). The groundmass is composed of well-foliated muscovite–biotite–quartz–Fe–Ti oxides and some lenses of an altered 'cloudy' phase, presumably sericite replacement of plagioclase. The peak metamorphic assemblage is inferred to be staurolite–biotite–muscovite–quartz–plagioclase–ilmenite(–magnetite).

GSWA 208364, 36493: pelitic schist, Nick Belt

These samples contain porphyroblasts of staurolite, garnet and biotite. Staurolite prisms up to 1 cm long and flakes of biotite 3 mm across are randomly oriented in a fine-grained schistose quartz matrix with minor muscovite and fine-grained altered plagioclase. Sparse Fe–Ti oxides are scattered throughout the groundmass. The staurolite porphyroblasts contain abundant aligned quartz inclusions. The inclusion trails are generally aligned at a high angle to, and truncated by, the external fabric, although some inclusion trails suggest rotation during growth. The foliation also wraps around euhedral garnet porphyroblasts up to 2 mm in size. The porphyroblasts are strongly altered, and contain inclusions of rounded quartz. Garnet in direct contact with staurolite generally maintains a euhedral shape and appears to have grown at the expense of staurolite (Fig. 5g). Based on these observations, the peak metamorphic assemblage is interpreted to be staurolite–garnet–muscovite–biotite–quartz(–plagioclase–ilmenite–magnetite).

FK4

30.03.15

Figure 4. (left) Field photographs from the Mutherbukin Zone: a) Rotated K-feldspar porphyroclasts in fine-grained, strongly sheared metamonzogranite are generally consistent with dextral transpression (top to the west) associated with the oldest (S_1) fabric; b) granitic gneiss representing the highest grade sample analysed in this study (GSWA 195826) with cm-scale K-feldspar augen defining a composite S_1–S_2 fabric and concordant to slightly discordant lenticular leucosomes with well-developed biotite selvedges; c) an example of granitic gneiss containing leucocratic patches with diffuse margins that are in petrologic continuity with the leucocratic layering in the gneiss; d) thin amphibolite and finer grained granitic layers aligned with the S_1 fabric are boudinaged with leucosome accumulation in interboudin partitions, suggestive of the crystallization of former melt during localized S_2 transtension; e) north-dipping muscovite–chlorite schists in the northern Nick Belt with mm- to cm-scale magnetite porphyroblasts defining a strong east-plunging lineation; f) muscovite–chlorite schists with cm-scale andalusite porphyroblasts oriented orthogonal to oblique to the lineation defined by magnetite; g) randomly oriented staurolite porphyroblasts within andalusite-bearing schists in the southern Nick Belt; h) interlayered garnet amphibolite and subordinate calc-silicate gneiss adjacent to staurolite(–garnet) schists at the Tommie Well locality

Tommie Well

About 50 km southeast of the Nick Belt, garnet- and staurolite-bearing pelitic schists (GSWA 88436) outcrop as a narrow fault-bound lens within the Davey Well Granite (Fig. 3a). The exposure grades from staurolite-rich, garnet-poor lithologies to garnet-rich, staurolite-poor lithologies on a decametre scale, suggesting minor compositional variability inherited from the sedimentary protolith. The schists show evidence for two metamorphic fabrics. The first fabric (S_1) is crenulated and folded by an easterly trending, upright schistosity (S_2), which is the dominant fabric in the rocks. In some instances the S_1 fabric is obliterated in the matrix, being preserved only as folded inclusion trails within cm-scale staurolite porphyroblasts. This locality also contains a small exposure of interlayered garnet amphibolite and subordinate calc-silicate gneiss (Fig. 4h). The garnet porphyroblasts in the amphibolite also locally preserve the older S_1 fabric, which is slightly oblique to the main S_2 foliation (GSWA 208362).

GSWA 88436: staurolite schist, Tommie Well

The fine-grained matrix is composed of quartz–muscovite–biotite with minor plagioclase and Fe–Ti oxides. The groundmass is well-foliated and in some places crenulated. Staurolite porphyroblasts (1 to 2 cm in size) contain abundant aligned inclusions of quartz(–minor Fe–Ti oxides–biotite). Some of the larger quartz inclusions in the staurolite porphyroblasts may also contain very fine-grained chlorite laths. The foliation in the matrix wraps around staurolite porphyroblasts and truncates their internal fabric, defined by the quartz inclusions (Fig. 5h). Small scattered garnet porphyroblasts are observed in outcrop, but obvious garnet is not present in this sample. The peak metamorphic assemblage for this sample is inferred to be staurolite–biotite–muscovite–magnetite–ilmenite–quartz(–plagioclase).

GSWA 208362: garnet amphibolite, Tommie Well

This sample contains a fine-grained foliated matrix dominated by hornblende, with lesser amounts of quartz, plagioclase, and titanite. Euhedral garnet porphyroblasts ranging from 2 to 8 mm in size make up to 15–20% of the thin section (Fig. 6a). The foliation wraps around the garnet porphyroblasts and truncates the weak internal fabric defined by fine-grained inclusions of rounded quartz, titanite, minor hornblende and trace ilmenite. The inclusion phases are similar to the matrix, although comprise significantly less hornblende and more titanite. In some garnets, an inclusion-rich core domain mimics the overall grain shape and is surrounded by a rim domain with fewer inclusions (Fig. 6a). The peak metamorphic assemblage for this sample is interpreted to be garnet–hornblende–plagioclase–quartz–titanite(–ilmenite).

Additional localities

Four additional samples were collected south–southeast of Tommie Well (Fig. 3a). Sample GSWA 183207 was collected from a small intrusion of metamorphosed Tetlow Granite, an alkaline phase within the Davey Well batholith. The sample is a gneissic leucocratic tonalite with a strong L-tectonite fabric defined by clots of metamorphic garnet–epidote. About 3.5 km south of this locality, a sample of metasomatized muscovite–tourmaline–quartz–biotite schist (GSWA 88475) was collected from the margin of a zoned pegmatite dyke. The pegmatite contains a 3 m-wide orthoclase-rich core with a 2 m-wide metasomatized margin. The dyke cuts the S_1 layering in the host schists, and appears to plunge parallel to F_2 crenulation fabrics in the schists. Tourmaline porphyroblasts in the schist overgrow the S_1 fabric and are commonly subparallel to the crenulation hinge but locally may also cut it. The easternmost sample is an andalusite-bearing schist from the Nardoo Well area (GSWA 46981). The sample was collected from the core of a major Edmundian Orogeny-aged (1030–955 Ma) F_2 fold. The highest grade sample from this study is a granitic gneiss collected from McCarthy Well, within the core of the Lockier Anticline (GSWA 195826). At this locality, the gneiss generally contains strongly deformed cm-scale K-feldspar augen defining an east-plunging lineation and locally contains discrete leucocratic patches up to 30 cm long and 5 cm wide.

GSWA 88475: metasomatic schist, New Well 10

This sample was collected 17 km southeast of the Tommie Well locality. It is composed of a fine-grained matrix of muscovite–quartz–biotite. Splays of tourmaline are up to 2 cm across.

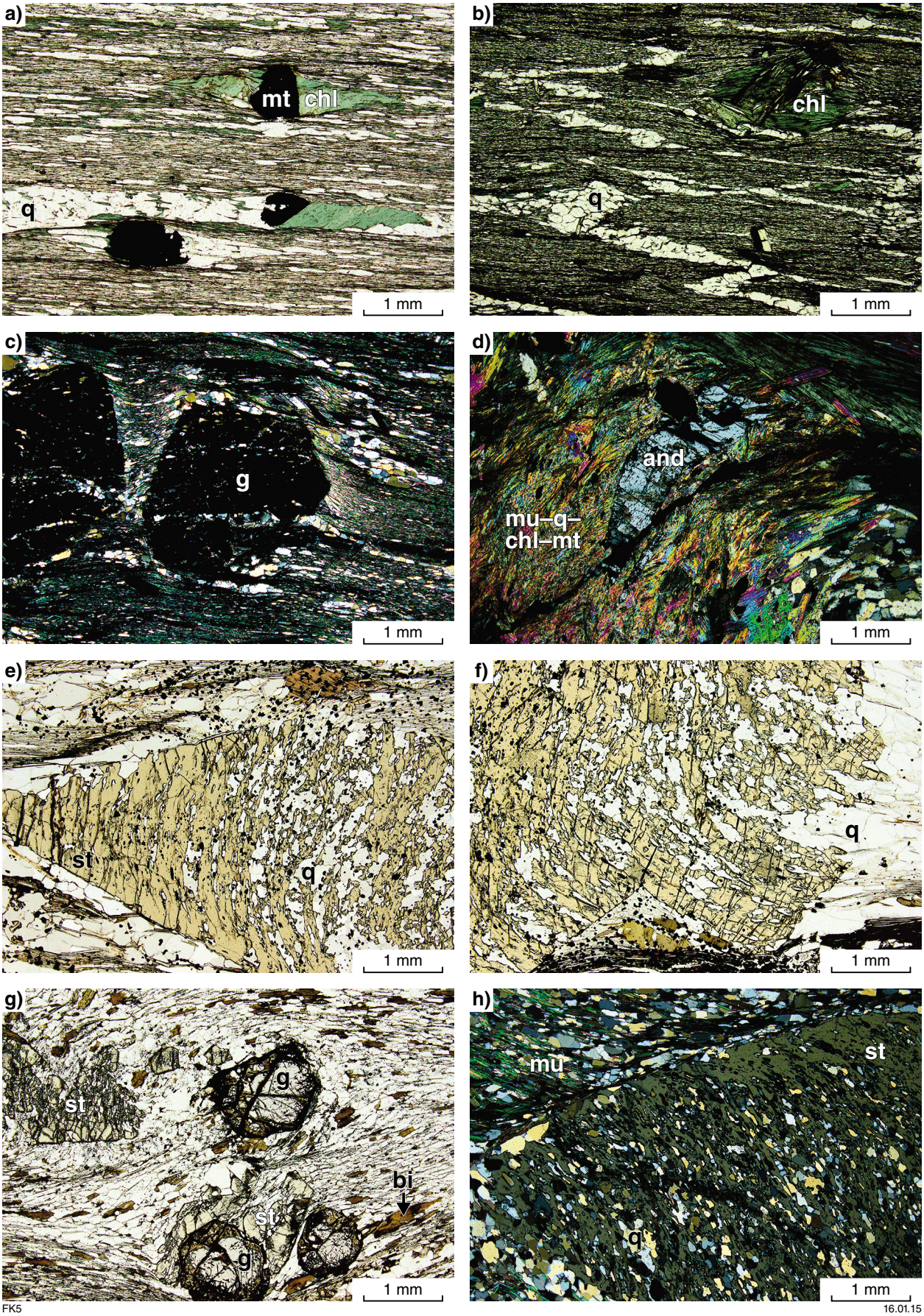
a)
mt
chl
q
1 mm
b)
chl
q
1 mm
c)
g
1 mm
d)
and
mu–q–
chl–mt
1 mm
e)
st
q
1 mm
f)
q
1 mm
g)
st
g
bi
st
g
1 mm
h)
mu
st
q
1 mm
FK5
16.01.15

Figure 5. (left) Photomicrographs from the metasedimentary schist samples: a) Magnetite porphyroblasts in muscovite–chlorite schist are commonly flattened with quartz and chlorite pressure shadows (GSWA 195851; plane polarized light); b) fine-grained groundmass of chlorite–muscovite–biotite with chlorite porphyroblasts and quartz stringers folded axial planar to the foliation (GSWA 195852; plane polarized light); c) garnet porphyroblasts up to 3 mm in size with aligned inclusions of quartz and minor magnetite, parallel to the fabric in the groundmass (GSWA 195852; crossed polarized light); d) large (2 cm-sized) aggregate of muscovite–quartz–chlorite–magnetite, with relict of andalusite, indicating that the aggregates represent retrograde pseudomorphs after andalusite. These porphyroblasts are commonly kinked, with chlorite and muscovite concentrated in the fold hinge (GSWA 195853; crossed polarized light); e) euhedral staurolite porphyroblasts up to 1.5 cm in length with abundant inclusions of quartz and rounded Fe–Ti oxides that are aligned at an oblique angle and truncated by the external foliation which wraps around the staurolite porphyroblasts (GSWA 208363; plane polarized light); f) some staurolite porphyroblasts have rotated inclusion trails that can be followed into polycrystalline quartz stringers in the host (GSWA 208363; plane polarized light); g) garnet in direct contact with staurolite generally maintains a euhedral shape and appears to have grown at the expense of staurolite (GSWA 208364; plane polarized light); h) the foliation in the matrix wraps around a staurolite porphyroblast and truncates the internal fabric, defined by the quartz inclusions (GSWA 88436; crossed polarized light)

GSWA 46981: pelitic schist, Nardoo Well

This sample was collected from the Nardoo Well area (Sheppard et al., 2007), about 22 km southeast of the Tommie Well locality. The sample comprises andalusite–chlorite–biotite–quartz–muscovite–Fe–Ti oxides. The fine-grained schistose matrix generally wraps around andalusite and biotite porphyroblasts.

GSWA 183207: metamorphosed alkaline granite, New Well

This rock is a heterogeneous granoblastic granofels comprising sodic plagioclase–clinopyroxene–quartz–epidote–titanite–lime-green garnet–Fe–Ti oxides. The main accessory minerals are hornblende, apatite, and altered allanite. Most of the rock is a plagioclase-rich micromosaic with grains about 1 mm in diameter. Quartz occurs as small rounded inclusions in plagioclase and as discrete grains to 2 mm in diameter. Irregular calc-silicate aggregates contain green clinopyroxene (ferrosalite or hedenbergite) as poikiloblastic and embayed grains up to 3 or 4 mm long, garnet, epidote, and coarse-grained titanite (Fig. 6b), as well as minor bluish-green hornblende. Small inclusions of hornblende are also common in clinopyroxene (Fig. 6c). Coarse-grained titanite may have embayed and ragged edges, extending into smaller recrystallized grains closely associated with euhedral epidote (Fig. 6c). Thin quartz films are observed around euhedral epidote. Cores of altered probable allanite up to 1.5 mm long are rimmed by coarse epidote. Magnetite grains up to 2 mm have narrow rims of hematite. Based on these observations, the peak metamorphic assemblage for this sample is inferred to be clinopyroxene–epidote–titanite–garnet–magnetite–plagioclase–quartz. Hornblende is mainly preserved as inclusions in clinopyroxene and may not be part of the peak metamorphic assemblage.

GSWA 195826: monzogranitic gneiss, McCarthy Well

The sample is a medium-grained metamonzogranite, composed of K-feldspar–quartz–plagioclase–biotite–titanite with accessory sericite–chlorite–epidote–zircon (Fig. 6d). K-feldspar (microcline) is mainly unaltered, and occurs as anhedral crystals, from 0.5 to 2 mm long, intergrown with quartz and plagioclase. Plagioclase occurs as unaltered, anhedral, unzoned crystals from 0.5 to 2 mm long. Biotite crystals are typically well-formed, randomly oriented, and unaltered, although some grains are embayed and resorbed with thin films of quartz along grain boundaries (Fig. 6e,f), consistent with incipient melting. Biotite is associated with rounded titanite crystals that are up to 2 mm long and contain inclusions of apatite prisms and small biotite plates. Granophyre is locally developed along quartz–feldspar grain boundaries. Alteration is minimal and restricted to sericite in some K-feldspar crystals and minor chloritization of biotite. The peak inferred metamorphic assemblage for this sample is K-feldspar–plagioclase–titanite–quartz–biotite–melt(–epidote–Fe–Ti oxides).

Garnet chemistry

Garnet compositions and element distribution maps from two metasedimentary schist samples in the Nick Belt (GSWA 195852 and 208364) and from the garnet amphibolite at Tommie Well (GSWA 208362) were obtained with a JEOL 8530F Hyperprobe at the Centre for Microscopy, Characterisation and Analysis, The University of Western Australia. Quantitative point analyses were collected using an accelerating voltage of 15 kV, a beam current of 20 nA, and a 1 μm beam diameter. Counting times were typically 20 s on peak and 10 s on background. The standards employed for instrument calibration were commercially available metals, oxides, silicates and phosphates, and the Armstrong/Love Scott (Armstrong, 1988) Φ–ρ–z matrix correction routine was used. Ferric iron contents were determined using the stoichiometric method of Schumacher (1991). Wavelength-dispersive (WD) quantitative maps were also obtained for one grain from GSWA 208362. Operating conditions were 40 degrees take-off angle, accelerating voltage of 15 kV and beam current of 80 nA. The beam was fully focused with a dwell time per pixel of 20 ms and a 2 x 2 μm pixel dimension. On-peak counting times were 20 s and mean atomic number background and matrix corrections were used. The algorithm utilized was that of Armstrong/Love Scott (Armstrong, 1988). Image processing was performed offline with CalcImage® software. Garnet images and line traverses are shown in Figure 7; selected quantitative maps from GSWA 208362 are shown in Figure 8. Representative garnet compositions and maps are provided in Appendix 1.

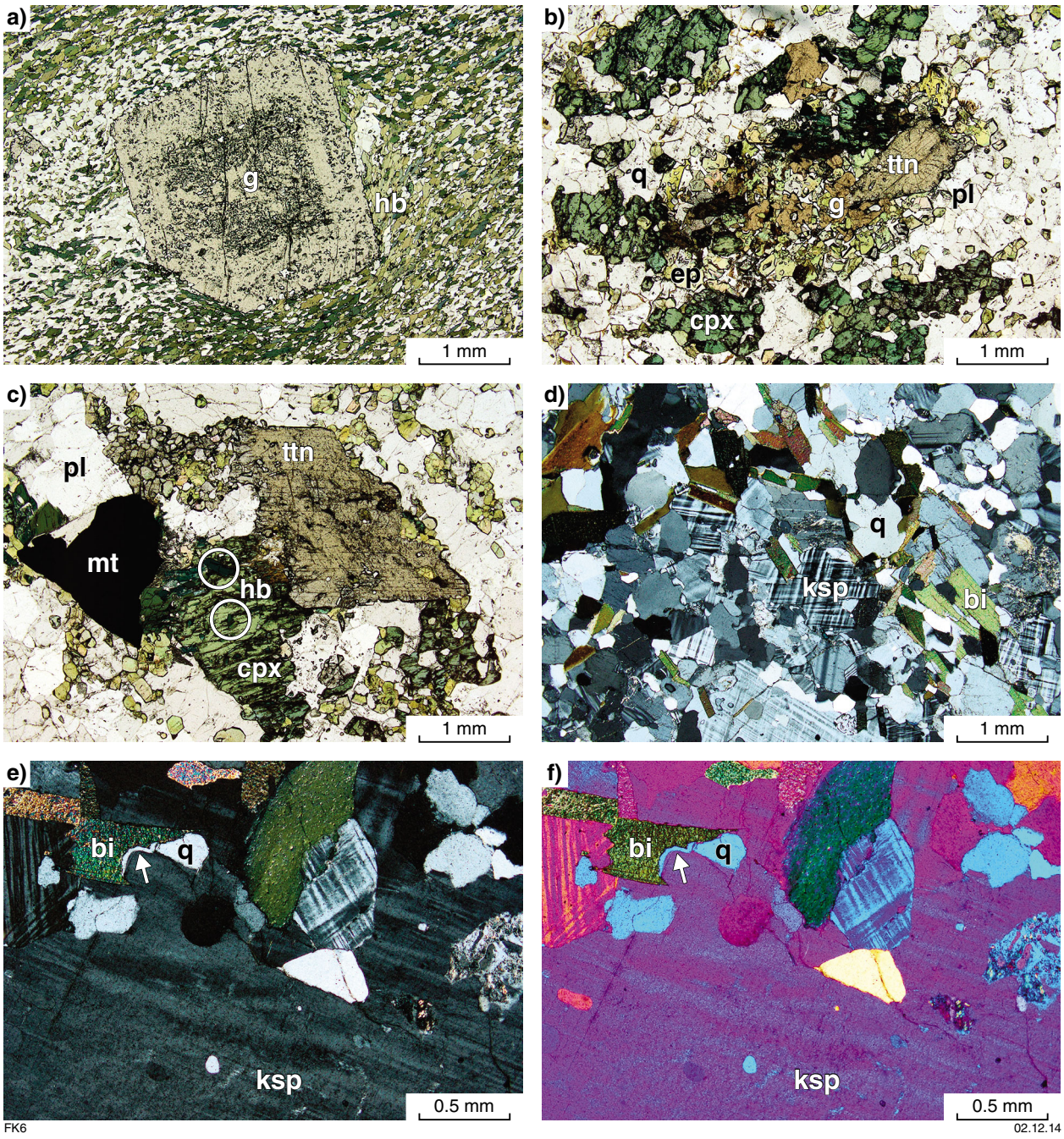

Figure 6. **Photomicrographs from other samples in this study: a) Garnet amphibolite from Tommie Well with hornblende and lesser amounts of quartz, plagioclase, and titanite. The foliation wraps around euhedral garnet porphyroblasts and truncates the weak internal fabric defined by fine-grained inclusions of rounded quartz, titanite, minor hornblende and trace ilmenite. Some garnets contain an inclusion-rich core domain which mimics the overall grain shape, surrounded by a rim domain with fewer inclusions (GSWA 208362, grain 3; plane polarized light); b) irregular calc-silicate aggregates comprising poikiloblastic, embayed green clinopyroxene, garnet, epidote, and coarse-grained titanite, with minor bluish-green hornblende (GSWA 183207; plane polarized light); c) small inclusions of hornblende (denoted by circles) occur in clinopyroxene, and coarse-grained titanite has embayed and ragged edges, extending into smaller recrystallized grains closely associated with euhedral epidote (GSWA 183207; plane polarized light); d) groundmass of metamonzogranite, composed mainly of K-feldspar, quartz, plagioclase, biotite and titanite (GSWA 195826; crossed polarized light); e) embayed biotite grain with thin film of quartz (shown by arrow), consistent with breakdown of biotite and incipient melting (GSWA 195826; crossed polarized light); f) same field of view as e), but with quartz plate inserted to highlight the quartz film (in blue)**

Garnet compositions and zoning

GSWA 195852: semipelitic schist, Nick Belt

Garnet porphyroblasts in this sample are highly altered and stained with iron oxides. Abundant fractures filled with chlorite and other very fine-grained phases penetrate the porphyroblasts (Fig. 7a). The compositions are generally almandine- and spessartine-rich (Fig. 7b), with X_{Alm} (=Fe^{2+} / [Fe^{2+} + Mg + Ca + Mn]) contents ranging from 0.58 to 0.70 and X_{Sps} (=Mn/ [Fe^{2+} + Mg + Ca + Mn]) ranging from 0.17 to 0.27. X_{Prp} (=Mg/ [Fe^{2+} + Mg + Ca + Mn]) and X_{Grs} (=Ca / [Fe^{2+} + Mg + Ca + Mn]) are more constant, with values of 0.07–0.09, and 0.05–0.07, respectively. Although primary core and rim compositions have likely been affected by the pervasive alteration and fracturing, the cores generally have higher X_{Alm} and lower X_{Sps} compared with the rims (Fig. 7b).

GSWA 208364: pelitic schist, Nick Belt

Garnet porphyroblasts in this sample have altered rims and a few thin fractures (Fig. 7c,e). The unaltered relics show progressive zoning, and are dominated by almandine- and spessartine-rich compositions (Fig. 7d,f): X_{Alm} increases from 0.62 to 0.75 from core to the edge adjacent to the alteration rim, and X_{Sps} decreases from 0.28 to 0.08. X_{Prp} and X_{Grs} contents are low (<0.1) and show very subtle increases from core to rim, with values of, respectively, 0.06 – 0.10 and 0.05 – 0.07.

GSWA 208362: garnet amphibolite, Tommie Well

Euhedral garnet porphyroblasts in this sample show more complex zoning than the two metasedimentary schist samples from the Nick Belt. X-ray composition maps and line traverses conducted across two grains show slight differences (Figs 7g–j and 8), which could be due to cut effects across the grains. The grains are strongly zoned in X_{Alm} and X_{Grs} contents; X_{Sps} shows a gradual decrease from 0.30 in the cores to 0.10 in the rims and X_{Prp} values are between 0.02 and 0.04 (Fig. 7h,j). The most well-defined zoning is preserved in grain 3, with four distinct domains based on X_{Alm} and X_{Grs} contents and the presence or absence of inclusion phases (Figs 7j and 8). The innermost core (garnet I) is subrounded and contains abundant inclusions of quartz. This domain has a composition of $Alm_{39–43}Grs_{30–33}Sps_{22–27}Prp_3$. The core is mantled by an inclusion-rich domain (garnet II) up to 40 μm in width. Inclusion phases in garnet II are dominated by quartz, hornblende and titanite, with trace epidote, albite and chlorite. Garnet II contains the highest X_{Grs} and lowest X_{Alm} observed in the grain, with a compositional peak of $Alm_{36}Grs_{41}Sps_{21}Prp_2$. The change in composition between garnet I and garnet II is gradational, suggesting progressive growth or diffusion gradients across the interface. Garnet II is surrounded by a thin (~15 μm wide) rim of garnet III, which contains sparse inclusions of quartz and titanite. Garnet III is characterized by a sharp decrease in X_{Grs} and increase in X_{Alm}. The outermost rim (garnet IV) is up to 40 μm wide and hosts numerous inclusions of quartz and titanite. Abundant hornblende, which makes up a significant proportion of the surrounding matrix, is notably absent in garnet IV. This domain generally defines a euhedral shape that mimics the shapes of garnet II and garnet III. The composition of garnet IV ranges from $Alm_{48}Grs_{30}Sps_{19}Prp_3$ at the inner contact with garnet III to $Alm_{54}Grs_{31}Sps_{11}Prp_4$ at the outer rim.

U–Pb geochronology

Monazite, xenotime, and zircon U–Th–Pb isotope data were collected using the SHRIMP at the John de Laeter Centre for Isotope Research, Curtin University, in Perth, Western Australia. Monazite was analysed from six metasedimentary schist samples; xenotime was also analysed from three of these samples. Polished thin sections were examined using back-scattered electron (BSE) microscopy to identify suitable grains for SHRIMP geochronology. Portions of the thin sections containing grains large enough (>10 μm) for ion microprobe analysis were drilled out to preserve the petrographic context of the grains, and cast in 25 mm epoxy mounts. Unless otherwise indicated, results for each sample were obtained during a single analytical session. Descriptions of analytical techniques and U–Th–Pb isotope data tables for the phosphate phases are provided in Appendix 2. Back-scattered electron images and compositional X-ray maps of selected grains are shown in Figures 9 and 10, respectively; Tera–Wasserburg concordia diagrams for the phosphates are provided in Figure 11. Separated zircons from one sample of granitic gneiss were also analysed using the SHRIMP (Wingate et al., 2013). Isotope data tables for zircon are provided in Appendix 3; analytical techniques are described in Wingate and Kirkland (2013). Dates are based on $^{207}Pb^*/^{206}Pb^*$ ratios (Pb* indicates radiogenic Pb). Results for individual analyses in data tables (Appendices 2 and 3) are quoted with 1-sigma (1σ) uncertainties; mean dates are quoted below with 95% (tσ√MSWD) confidence intervals. Data are placed into different groups, including Groups M, M2, and M3 for data reflecting successive metamorphic events, Group P for data that may represent mixtures of monazite of different ages, possible younger monazite growth or recrystallization, or loss of radiogenic Pb, and Group D for data excluded due to discordance or high common Pb. Age results for all the samples are summarized in Table 1.

In situ U–Pb geochronology of monazite and xenotime

GSWA 188998: semipelitic schist, Nick Belt

Twenty-eight analyses of 15 monazite grains were performed. The grains range in size from 20 to 60 μm and have rounded to euhedral shapes. They are generally elongate and aligned within the foliation (Fig. 9a). Some grains also occur within quartz, typically adjacent to grain boundaries or cracks. Nine analyses with >12%

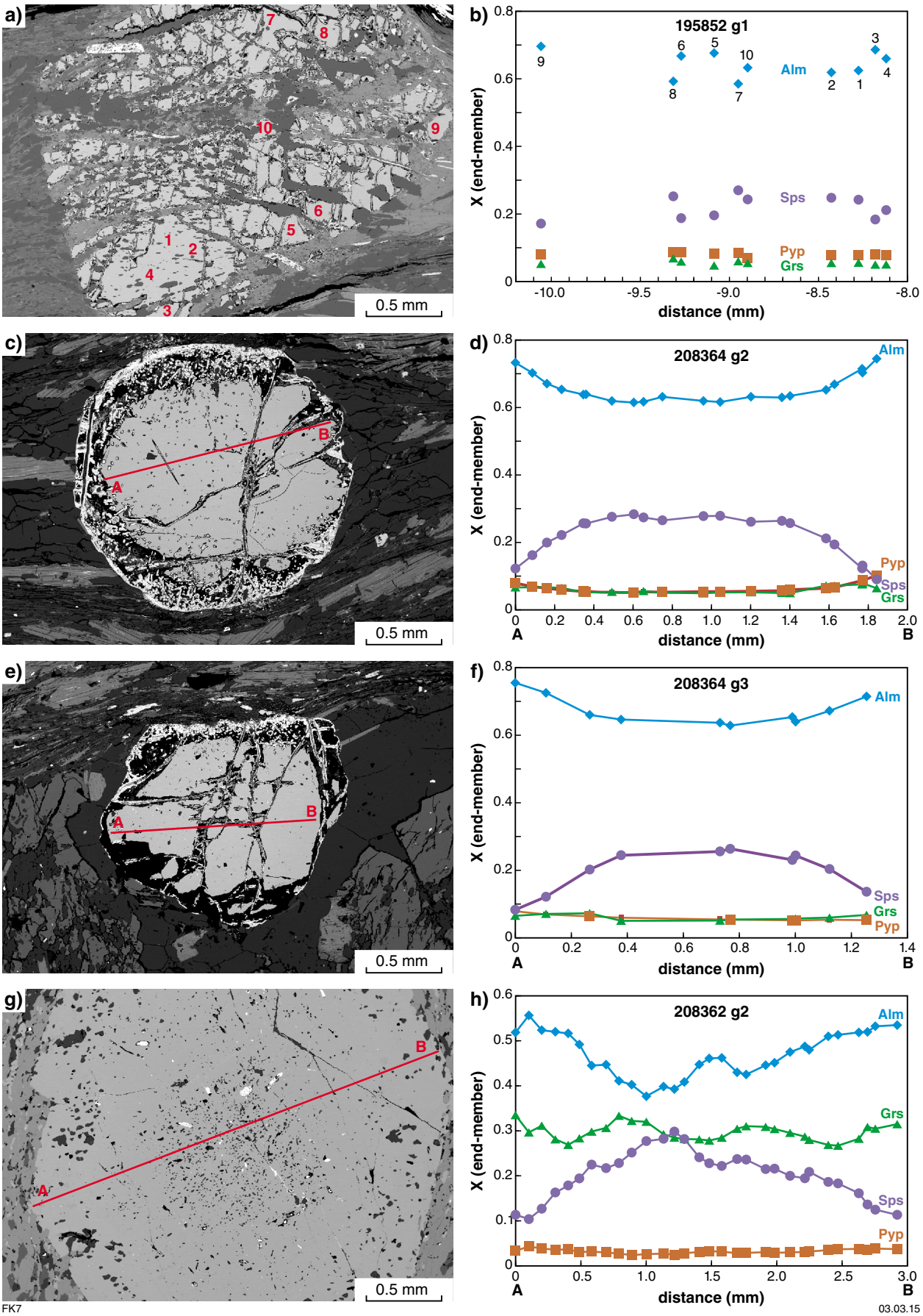
a)
7
8
10
9
6
5
1
2
4
3
0.5 mm
b)
195852 g1
6
5
10
3
9
Alm
8
7
2
1
4
Sps
Pyp
Grs
X (end-member)
distance (mm)
c)
B
A
0.5 mm
d)
208364 g2
Alm
Pyp
Sps
Grs
X (end-member)
A
B
distance (mm)
e)
B
A
0.5 mm
f)
208364 g3
Alm
Sps
Grs
Pyp
X (end-member)
A
B
distance (mm)
g)
B
A
0.5 mm
h)
208362 g2
Alm
Grs
Sps
Pyp
X (end-member)
A
B
distance (mm)
FK7
03.03.15

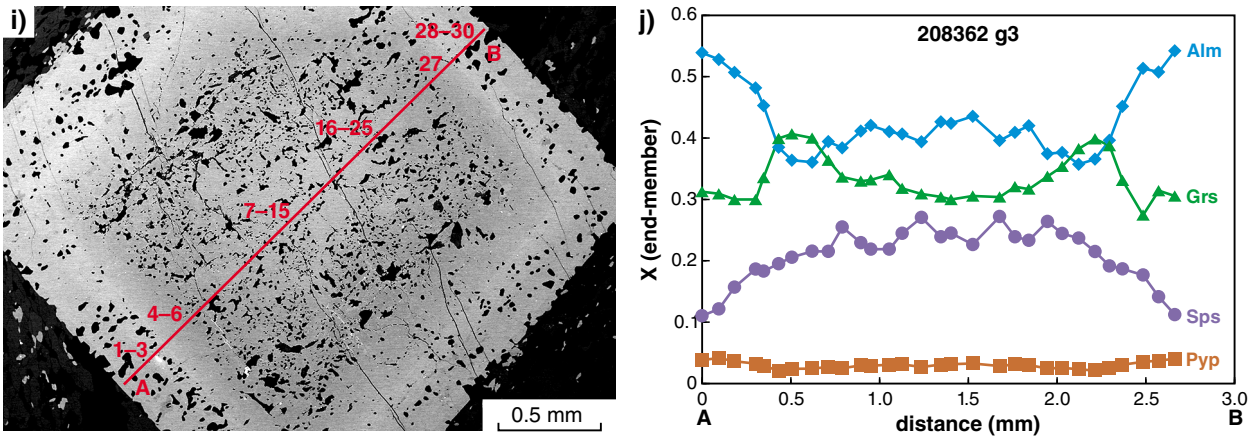

Figure 7. (left and above) Analysed garnet grains showing line traverses and compositions: a) Back-scattered electron image (BSE) of grain 1, GSWA 195852; b) spot analyses; c) BSE image of grain 2, GSWA 208364; d) line traverse; e) BSE image of grain 3, GSWA 208364; f) line traverse; g) BSE image of grain 2, GSWA 208362; h) line traverse; i) BSE image of grain 3, GSWA 208362; j) line traverse

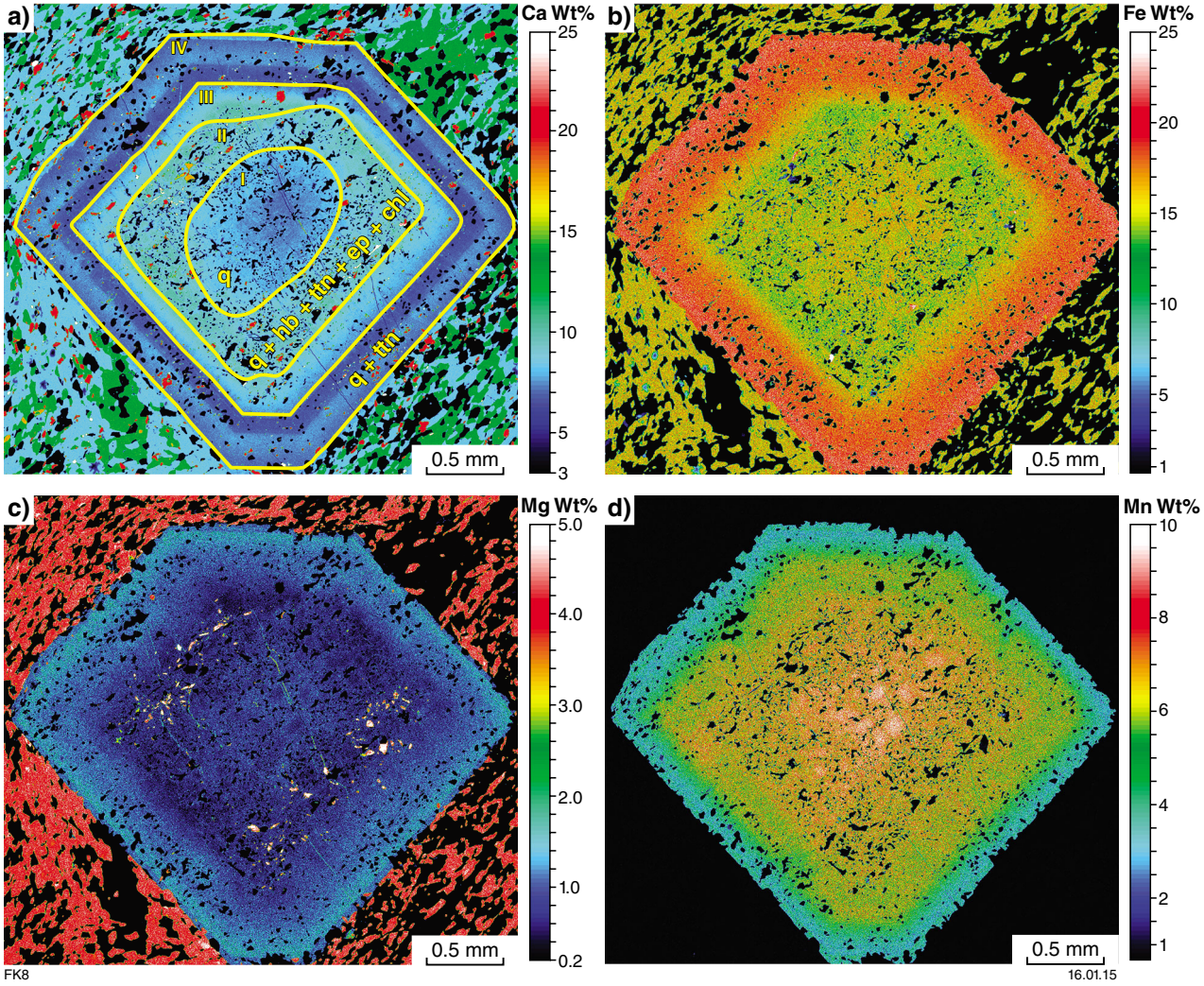

Figure 8. Selected quantitative element maps from grain 3, GSWA 208362 (Fig. 7i,j), with four distinct domains (garnet I, II, III, IV) based on X_{Alm} and X_{Grs} contents and the presence or absence of inclusion phases: a) Ca elemental map; b) Fe elemental map; c) Mg elemental map; d) Mn elemental map

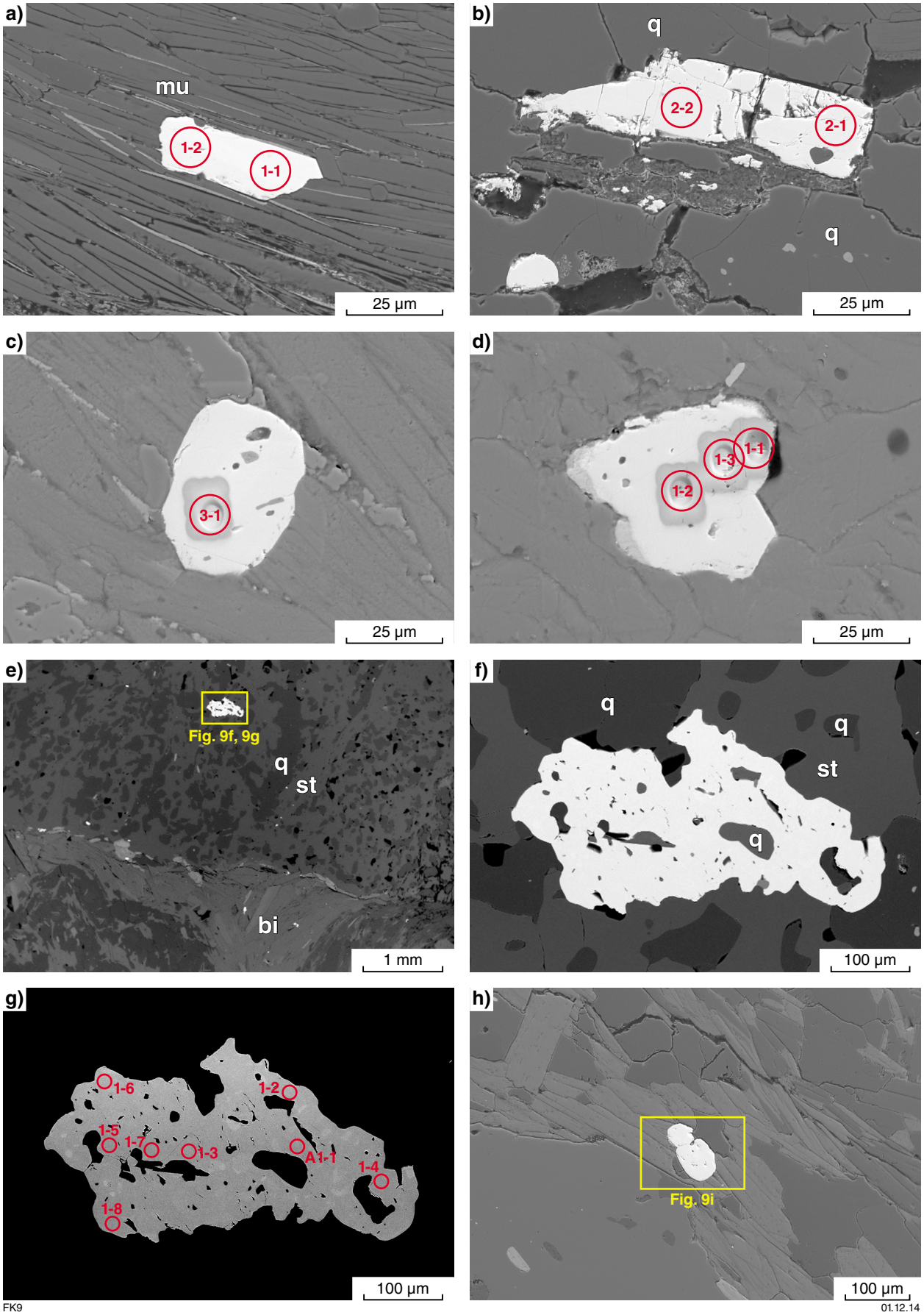
a)
mu
1-2
1-1
25 µm
b)
q
2-2
2-1
q
25 µm
c)
3-1
25 µm
d)
1-3
1-1
1-2
25 µm
e)
Fig. 9f, 9g
q
st
bi
1 mm
f)
q
q
st
q
100 µm
g)
1-6
1-2
1-5
1-7
1-3
A1-1
1-4
1-8
100 µm
h)
Fig. 9i
100 µm
FK9
01.12.14

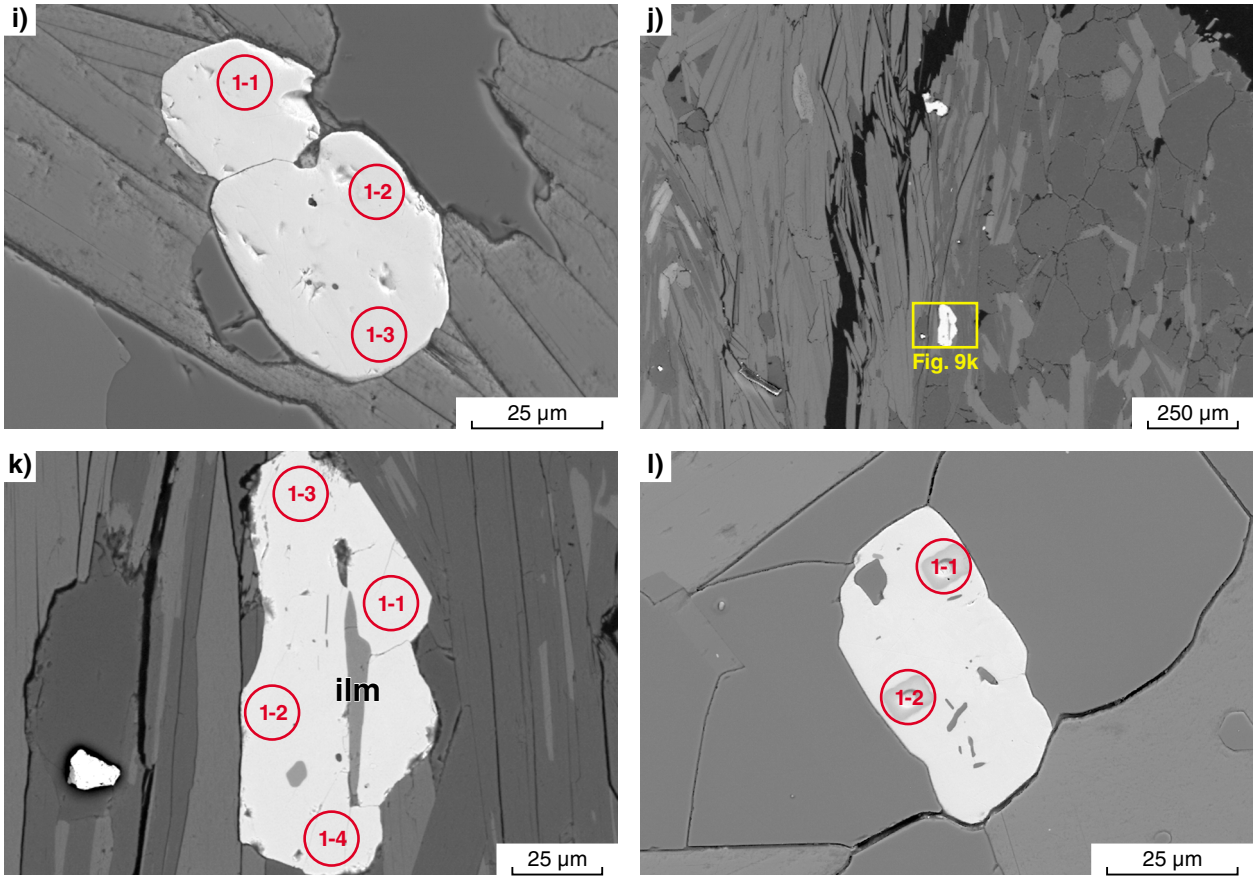

Figure 9. **(left and above) BSE images of selected monazite grains: a) GSWA 188998 (grain I); b) GSWA 188999 (grain D.2); c) GSWA 36493 (grain E3); d) GSWA 36493 (grain B1); e–g) GSWA 88436 (grain A1) — g) shows high contrast image of f) to highlight compositional domains within grain; h–i) GSWA 88436 (grain L1); j–k) GSWA 88436 (grain B1); l) GSWA 46981 (grain G). The location of SHRIMP analysis sites are shown along with the analysis number. SHRIMP U–Pb data for these samples are provided in Appendix 2**

discordance and with >2% common ^{206}Pb (f204 in data tables) are excluded (Group D). The remaining 19 analyses yield a wide spread of ^{207}Pb*/^{206}Pb* dates ranging from 1796 ± 65 to 1218 ± 13 Ma, and can be divided into three groups, based on ^{207}Pb*/^{206}Pb* ratios (Fig. 11a, Table 1).

The seven oldest analyses (Group M) yield a weighted mean ^{207}Pb*/^{206}Pb* date of 1750 ± 35 Ma (MSWD = 0.2). Two analyses of separate grains (Group M2), which indicate low common Pb, higher U (~2000 ppm) and Th (~62000 ppm) contents than other analyses, and are <5% discordant, yield a ^{207}Pb/^{206}Pb date of 1220 ± 18 Ma (MSWD = 0.2). The remaining 10 analyses (Group P) yield ^{207}Pb*/^{206}Pb* dates of 1589–1291 Ma and are dispersed beyond analytical precision.

The overall trend most likely represents a mixing array. However, the data are dispersed beyond a two-component mixing array, and intercept ages cannot be reliably calculated. Considering the relatively high common Pb contents of most analyses, recent Pb loss is a probable cause of dispersion beyond the mixing line. The date of 1750 ± 35 Ma for the seven analyses in Group M can be interpreted only as a minimum age for monazite growth, because the analyses are up to 12% discordant. The date of 1220 ± 18 Ma for the two analyses in Group M2 can be interpreted as a younger episode of monazite growth and modification, and is similar to the well-defined ages of monazite growth obtained from other samples in this study. The older dates for Group M analyses were obtained in part from monazite aligned with the mineral foliation; hence, the development of the foliation is possibly associated with the 1750 ± 35 Ma age component.

GSWA 188999: semipelitic schist, Nick Belt

Monazite grains in this sample are typically up to 50 µm in size and have subrounded to euhedral shapes. Most grains occur within quartz aggregates or adjacent to chlorite laths (Fig. 9b); some grains have ragged and altered grain boundaries. Twenty-seven analyses of 10 monazite grains were analysed (Fig. 11b). Three analyses >5% discordant (Group D) are not considered further. The remaining 24 analyses (Group M) yield a weighted mean ^{207}Pb*/^{206}Pb* date of 1187 ± 7 Ma (MSWD = 1.5; Table 1). This date is interpreted as the age of monazite growth during metamorphism.

GSWA 36493: pelitic schist, Nick Belt

Monazite occurs as rounded, euhedral to anhedral grains about 100 µm across, and contains inclusions of minerals found in the surrounding matrix (Fig. 9c,d). Compositional mapping shows that the grains generally have uniform La and Y contents and Th-rich cores (Fig. 10a–f). Nineteen analyses of seven monazite grains were analysed during two analytical sessions (Fig. 11c). Two analyses >5% discordant (Group D) are not considered further. The remaining 17 analyses yield $^{207}Pb^*/^{206}Pb^*$ dates of 1245–1190 Ma. The oldest analysis, with the highest Th content, yields a $^{207}Pb^*/^{206}Pb^*$ date that is just significantly older than the mean. Sixteen analyses (Group M) indicate a weighted mean $^{207}Pb^*/^{206}Pb^*$ date of 1206 ± 6 Ma (MSWD = 0.84; Table 1). Including the old outlier changes the weighted mean $^{207}Pb^*/^{206}Pb^*$ date to 1209 ± 8 Ma (MSWD = 1.4). The date of 1206 ± 6 Ma for 16 analyses in Group M is interpreted as the age of monazite growth during metamorphism.

GSWA 88436: staurolite schist, Tommie Well

Monazite in this sample typically occurs as rounded and interstitial grains up to 60 µm in size, containing inclusions of minerals found in the surrounding matrix. One monazite included within staurolite is up to 400 µm across; this grain has irregular margins with the staurolite host and overgrows rounded quartz included in the staurolite, suggesting that the monazite and staurolite are intergrown (grain 1425A; Fig. 9e–g). However, most of the analysed monazites occur within the fine-grained matrix (Fig. 9h,i) or in pressure shadows (Fig. 9j,k), with the exception of four grains that occur as inclusions in staurolite porphyroblasts (grains 1425A and -D.2, grains 0673K.1 and -K.2). The monazites exhibit very little zoning in La and Y content, but commonly display patchy Th zoning, including thin Th-rich overgrowths in some grains (Fig. 10g–i). Thirty-nine analyses were obtained from 25 monazites during three sessions; the petrographic setting of each grain and its results are provided in Appendix 2. All data indicate <1% common ^{206}Pb, and only one analysis (Group D) is >5% discordant (Fig. 11d). The remaining 38 analyses can be divided into three groups, based on their $^{207}Pb^*/^{206}Pb^*$ ratios (Table 1).

Twenty-three analyses of 11 monazites (Group M) yield $^{207}Pb^*/^{206}Pb^*$ dates (1σ) ranging from 1295 ± 12 to 1263 ± 13 Ma. The analyses were located in coarse-grained monazite intergrown with staurolite (Fig. 9e–g), as well as in smaller monazite inclusions within staurolite, grains associated with quartz and biotite within the matrix, and grains aligned with the foliation. These analyses define a weighted mean $^{207}Pb^*/^{206}Pb^*$ date of 1281 ± 3 Ma (MSWD = 1.2), interpreted as the age of staurolite growth and fabric development during peak metamorphism.

Seven analyses of five monazites (Group M2) yield $^{207}Pb^*/^{206}Pb^*$ dates (1σ) of 1251 ± 7 to 1234 ± 5 Ma, with a weighted mean of 1243 ± 7 Ma (MSWD = 0.76). These analyses were located mainly in grains aligned with the foliation (Fig. 9h,i) or associated with biotite, although one analysis (0673K.2-2) from an inclusion in staurolite yields a $^{207}Pb^*/^{206}Pb^*$ date of 1247 ± 15 Ma (1σ). The weighted mean date of 1243 ± 7 Ma is interpreted as the age of monazite growth during a younger metamorphic event, although the possibility that the overall age spread from c. 1295 to 1234 Ma represents protracted growth during a single event cannot be excluded.

Nine analyses of nine monazites (Group P) yield $^{207}Pb^*/^{206}Pb^*$ dates (1σ) of 1215 ± 5 to 1143 ± 7 Ma that are dispersed beyond analytical precision (MSWD = 13). These analyses were located in grains aligned with the matrix foliation or within biotite-rich pressure shadows surrounding staurolite (Fig. 9j,k). The oldest date in this group (1215 ± 5 Ma, 1σ) is from an analysis (1425A.1-3) of the monazite intergrown with staurolite. This analysis is not associated with distinct chemical zoning and the date is interpreted to reflect Pb loss. The other dates may reflect the timing of the latest stages of fabric development or, alternatively, may represent mixtures of monazite of different ages, implying monazite growth younger than 1200 Ma, or possibly Pb-loss.

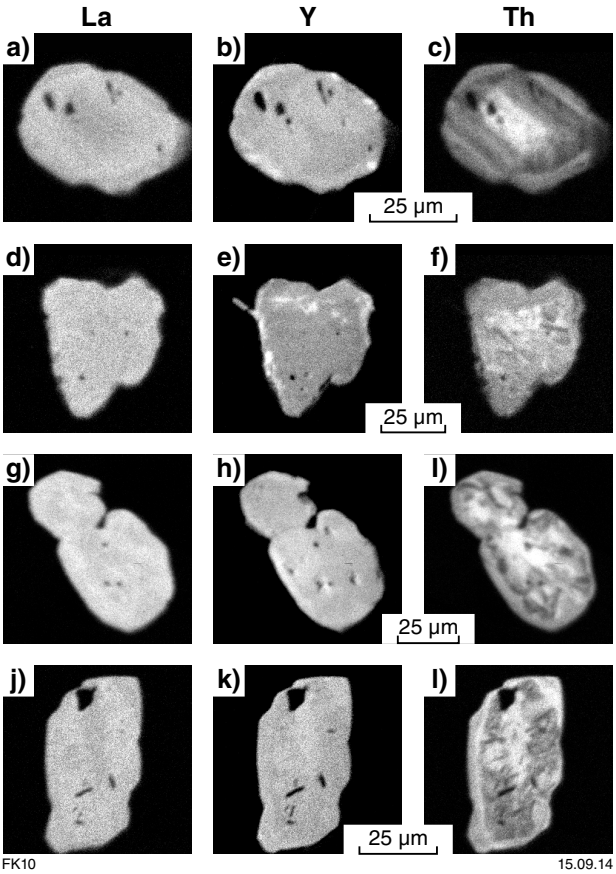

Figure 10. Compositional X-ray maps of selected monazite grains: a–c) La, Y, Th maps, respectively, from GSWA 36493 (grain E3); d–f) La, Y, Th maps from GSWA 36493 (grain B1); g–i) La, Y, Th maps from GSWA 88436 (grain L1); j–l) La, Y, Th maps from GSWA 46981 (grain G)

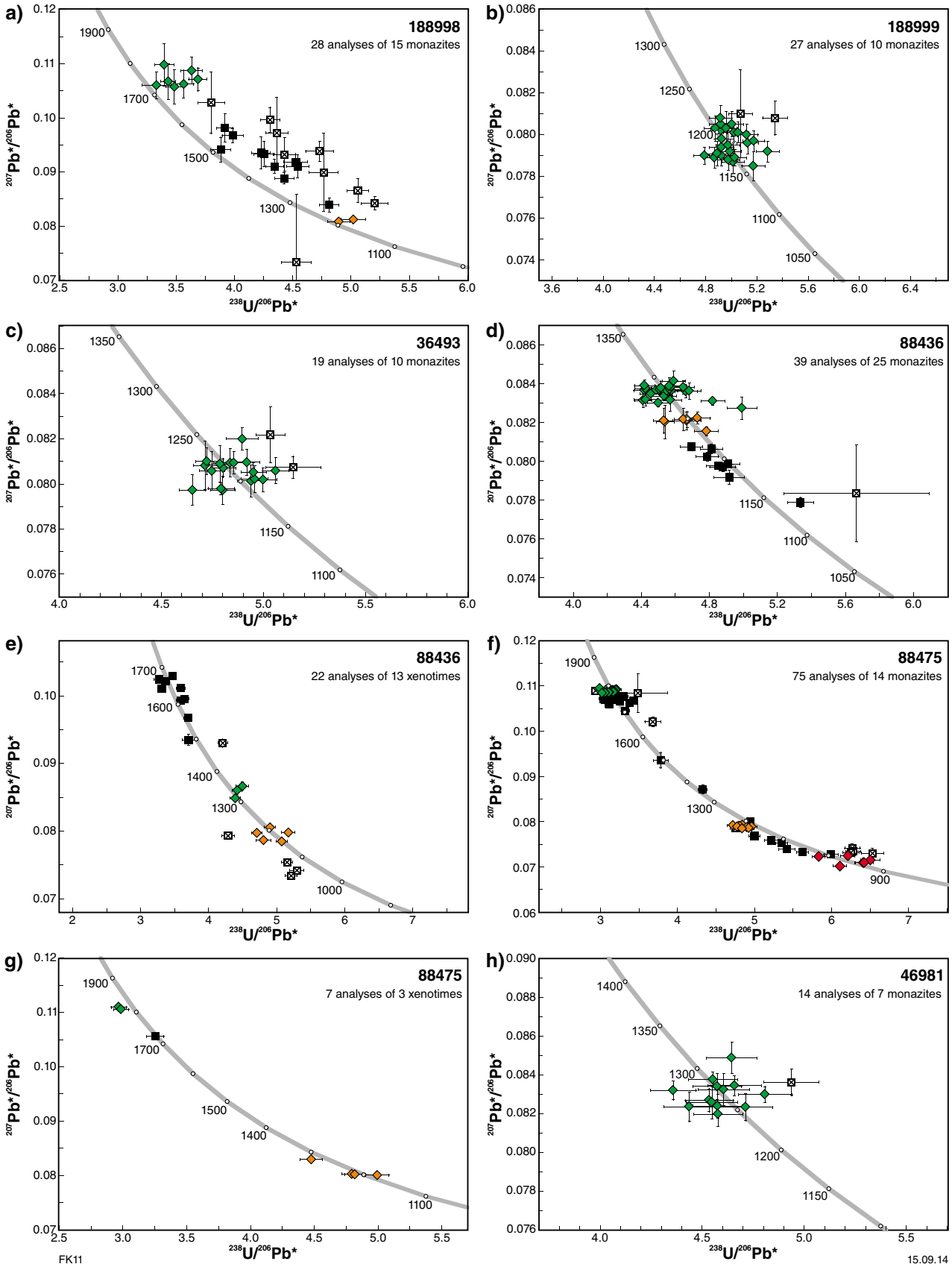

Figure 11. U–Pb concordia diagrams for monazite and xenotime. Green, orange and red diamonds correspond to metamorphic grains. Black squares are typically dispersed beyond analytical precision. Data >5% discordant are shown as squares with crosses. SHRIMP U–Pb data for these samples are provided in Appendix 2 (continued on page 20)

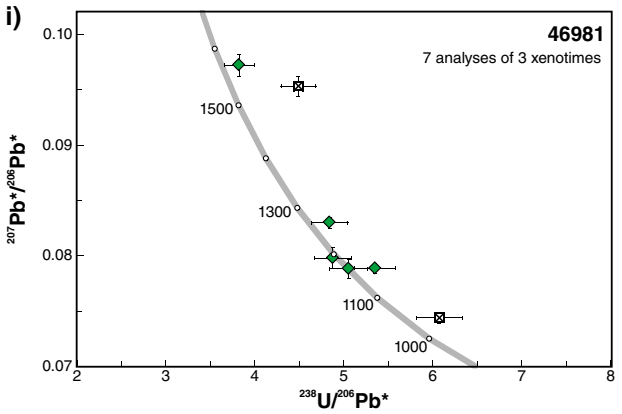

Figure 11. (continued) U–Pb concordia diagrams for monazite and xenotime. Green, orange and red diamonds correspond to metamorphic grains. Black squares are typically dispersed beyond analytical precision. Data >5% discordant are shown as squares with crosses. SHRIMP U–Pb data for these samples are provided in Appendix 2

Twenty-two analyses were also conducted of 13 xenotime grains from this sample (Fig. 11e). The grains are subhedral, rounded, 30–80 µm across, and generally occur along grain boundaries and within matrix phases. Five analyses >5% discordant (Group D) are not considered further. The remaining 17 analyses can be divided into three groups (Table 1), based on their $^{207}Pb^*/^{206}Pb^*$ ratios, although within each group the analyses are dispersed beyond analytical precision. Three analyses of three grains (Group M) yield $^{207}Pb^*/^{206}Pb^*$ dates between 1353 ± 13 and 1312 ± 7 Ma. Five analyses of five grains (Group M2) yield $^{207}Pb^*/^{206}Pb^*$ dates between 1210 ± 7 and 1159 ± 7 Ma. Nine analyses (Group P) yield $^{207}Pb^*/^{206}Pb^*$ dates of 1677–1497 Ma. The dates of 1353–1312 Ma for three analyses in Group M are interpreted to reflect the time of xenotime growth during either prograde metamorphism or an early metamorphic event. The dates of 1210–1159 Ma for five analyses in Group M2 are interpreted as the timing of xenotime growth during either retrograde metamorphism or a separate metamorphic event. Dates of c. 1670 Ma for the three oldest analyses in Group P are similar to the age of the Davey Well Granite that surrounds the schists at the Tommie Well locality, suggesting xenotime growth during intrusion of the granites and subsequent recrystallization.

GSWA 88475: metasomatic schist, New Well 10

The monazite grains in this sample are up to 400 µm in size, although most are less than 100 µm. The grains are typically concentrated in layers within the schistose fabric and have subrounded to subhedral shapes. Seventy-five analyses of 13 monazite grains were performed during three analytical sessions (Fig. 11f). All analyses indicate <1% common ^{206}Pb; eight analyses >6% discordant (Group D) are not considered further. The remaining 67 analyses yield $^{207}Pb^*/^{206}Pb^*$ dates (1σ) ranging from 1790 ± 5 to 933 ± 10 Ma, and can be divided into four groups, based on their $^{207}Pb^*/^{206}Pb^*$ ratios (Table 1).

Twenty-four analyses (Group M) yield a weighted mean $^{207}Pb^*/^{206}Pb^*$ age of 1780 ± 2 Ma (MSWD = 1.2). Ten analyses (Group M2) yield a weighted mean $^{207}Pb^*/^{206}Pb^*$ age of 1171 ± 4 Ma (MSWD = 1.3). Six analyses of four grains (Group M3) yield a weighted mean $^{207}Pb^*/^{206}Pb^*$ age of 958 ± 16 Ma (MSWD = 3.0). The analyses in Group M3 indicate lower U (≤6000 ppm) contents and higher Th/U than those in Group M2 (≥10 000 ppm U); the relatively high value of MSWD indicates minor dispersion of $^{207}Pb^*/^{206}Pb^*$ dates, although the mean of 958 ± 16 Ma is supported by an independently calibrated weighted mean $^{208}Pb/^{232}Th$ age of 967 ± 26 (MSWD = 0.2) for the same analyses. The mean $^{207}Pb^*/^{206}Pb^*$ dates for Groups M, M2, and M3 are interpreted to represent three distinct episodes of monazite growth or modification during metamorphism. Twenty-seven analyses (Group P) yield $^{207}Pb^*/^{206}Pb^*$ dates of 1770–1007 Ma that are dispersed beyond analytical precision, and are interpreted to reflect mixtures of monazite of different ages.

Twelve analyses were conducted of seven sites in two xenotime grains (Fig. 11g). The xenotime grains are subhedral, rounded, and 60–100 µm across. Both grains have high U contents (>7000 ppm) typical of magmatic xenotime, but yield very different ages. One grain was analysed during two separate sessions; four analyses (Group M) from two spots (including duplicate analyses) yield a weighted mean $^{207}Pb^*/^{206}Pb^*$ date of 1805 ± 9 Ma (MSWD = 1.3; Table 1). The third spot in this grain yielded younger dates (1725 and 1620 Ma) during the two sessions, possibly reflecting fine-scale recrystallization. Data for the second grain indicate $^{207}Pb^*/^{206}Pb^*$ dates (1σ) ranging from 1269 ± 9 to 1182 ± 7 Ma; although they are dispersed (MSWD = 15), they include significant changes in $^{207}Pb^*/^{206}Pb^*$ between duplicated analyses of single sites. This dispersion implies fine-scale recrystallization and consequent age mixing with at least some recrystallization ≤1200 Ma. The older age group may represent an episode of xenotime growth, but the data are not interpreted further.

GSWA 46981: pelitic schist, Nardoo Well

Monazite occurs as anhedral grains up to 100 µm across (Fig. 9l), intergrown with biotite or Fe–Ti oxide minerals and rich in inclusions. The monazites exhibit very little zoning in La and Y content, but commonly display patchy Th zoning with thin overgrowths in some grains (Fig. 10j–l). Fourteen analyses were conducted of seven monazite grains (Fig. 11h). The analyses define a weighted mean $^{207}Pb^*/^{206}Pb^*$ date of 1272 ± 9 Ma (MSWD = 1.3; Table 1), interpreted as the time of monazite growth during metamorphism. One of the 14 analyses is >7% discordant, but excluding it does not change the result significantly (1271 ± 10 Ma; MSWD = 1.3).

Three small (<50 µm) xenotime grains were analysed, all of which are intergrown with adjacent minerals.

Seven analyses from these grains yield a wide spread of $^{207}Pb^*/^{206}Pb^*$ dates (Fig. 11i), ranging from 1572 ± 19 to 1168 ± 22 Ma (1σ). At least two, and possibly all three, of these grains include xenotime of differing ages. Data from two grains suggest final recrystallization at c. 1170 Ma, but none of the ages is well defined.

U–Pb zircon geochronology

GSWA 195826: monzogranitic gneiss, McCarthy Well

Zircons isolated from this sample of Davey Well Granite are colourless to dark brown or opaque, and mainly subhedral and slightly rounded. The crystals are up to 700 µm long, and elongate, with aspect ratios up to 6:1. Most consist of concentrically-zoned cores overgrown by low-uranium rims, many of which are in turn overgrown by high-uranium rims. A cathodoluminescence (CL) image of representative zircons is shown in Figure 12a.

The geochronology of this sample was conducted by Wingate et al. (2013). Forty-three analyses were obtained from 28 zircons; results are provided in Appendix 3. The analyses are concordant to slightly discordant (Fig. 12b). Eight analyses are >10% discordant or indicate high common Pb ($f204$ >1%), and one analysis is interpreted to represent a mixture of core and rim material. The dates obtained from these nine analyses (Group D) are considered not to be geologically significant. The remaining analyses (n = 34) can be divided into four groups (Table 1), based on their uranium and thorium contents, Th/U and $^{207}Pb^*/^{206}Pb^*$ ratios, and locations within the crystals.

Group I comprises 12 analyses of 12 zircon cores, which yield a weighted mean $^{207}Pb^*/^{206}Pb^*$ date of 1664 ± 8 Ma (MSWD = 1.4). These analyses indicate mainly moderate uranium and thorium concentrations and moderate Th/U ratios. Group M is defined by five analyses of five low-uranium zircon rims, which yield a weighted mean $^{207}Pb^*/^{206}Pb^*$ date of 1321 ± 40 Ma (MSWD = 0.61). These analyses indicate very low uranium and thorium concentrations and very low Th/U ratios. Group M2 comprises 13 analyses of four high-uranium zircon rims, which yield a weighted mean $^{207}Pb^*/^{206}Pb^*$ date of 1200 ± 3 Ma (MSWD = 1.3). These analyses indicate very high uranium concentrations, very low thorium concentrations, and very low Th/U ratios. Group P is based on four analyses of three zircons. Two analyses of a low-uranium rim yield $^{207}Pb^*/^{206}Pb^*$ dates of c. 1188 and 1113 Ma, and two analyses of two zircon cores yield dates of c. 1628 and 1544 Ma.

The date of 1664 ± 8 Ma for the 12 analyses in Group I is interpreted as the magmatic crystallization age of the granite protolith. The date of 1321 ± 40 Ma for the five analyses in Group M is interpreted as the age of a metamorphic event. The date of 1200 ± 3 Ma for the 13 analyses in Group M2 is interpreted as the age of a second metamorphic event. The dates of 1628–1113 Ma for the four analyses in Group P are interpreted to reflect ancient loss of radiogenic Pb.

Phase equilibria modelling

The conditions of metamorphism and the microstructural evolution of nine samples across the Mutherbukin Zone are investigated using pseudosections based on bulk rock chemical compositions. These samples include five metasedimentary schist samples from the Nick Belt, one metasedimentary schist sample and one garnet-bearing amphibolite from Tommie Well, one sample of metamorphosed alkaline granite, and a sample of granitic gneiss. The modelled samples are closely associated with samples selected for geochronology; they are either the same samples or samples collected from the same

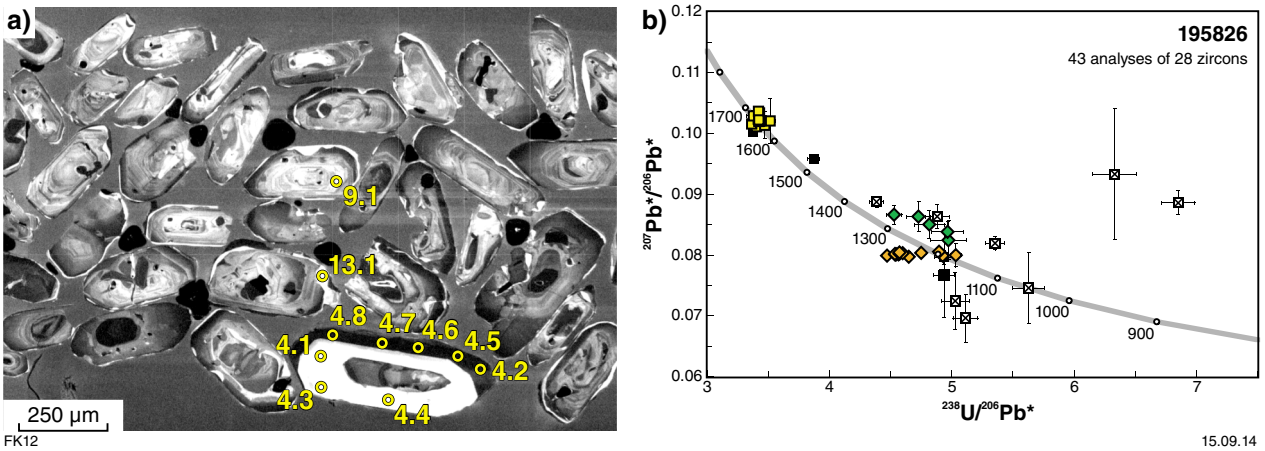

Figure 12. Results of U–Pb zircon geochronology from GSWA 195826 (from Wingate et al., 2013): a) Cathodoluminescence image of representative zircons. Numbered circles indicate the approximate locations of analysis sites; b) U–Pb analytical data. Yellow squares indicate Group I (magmatic zircons); green diamonds indicate Group M (metamorphic zircon rims); orange diamonds indicate Group M2 (younger metamorphic rims); black squares indicate Group P (radiogenic Pb loss); crossed squares indicate Group D (discordance >10%, high common Pb ($f204$ >1%), or core-rim mixture). One highly discordant and imprecise analysis in Group D is not shown. SHRIMP U–Pb data for this sample is provided in Appendix 3

locality. Locations for the modelled samples are shown in Figure 3a. Calculated pseudosections for each of the samples are provided in Appendix 4; the results of the nine samples are summarized in Figure 13 and Table 1.

The bulk chemical compositions were determined by X-ray fluorescence spectroscopy (Table 2) at ALS Chemex, Australia, together with loss on ignition (LOI). FeO contents were analysed by Fe^{2+} titration also at ALS Chemex, Australia, and Fe_2O_3 contents were calculated by difference. All data, as well as additional analytical details, are also available from the Geological Survey of Western Australia's GeoChem database (http://geochem.dmp.wa.gov.au/geochem/).

Thermodynamic calculations were performed using THERMOCALC 3.33 (Powell and Holland, 1988; updated June 2009) and the internally consistent thermodynamic dataset of Holland and Powell (1998; dataset tcds55, created in November 2003). The chemical systems and corresponding activity–composition (*a–x*) models were based on the most appropriate model system available for each sample. Although a revised thermodynamic dataset (Holland and Powell, 2011) and updated *a–x* models for metapelitic systems (White et al., 2014a, b) have recently become available, at the time the calculations for this study were performed, the updated *a–x* models were only calibrated for metapelitic compositions in the manganese-free chemical system NCKFMASHTO (Na_2O–CaO–K_2O–FeO–MgO–Al_2O_3–SiO_2–H_2O–TiO_2–Fe_2O_3). Therefore, for the calculations to be comparable between chemical systems appropriate for the range of samples considered in this study, the modelling uses the dataset of Holland and Powell (1998) and *a–x* models compatible with that dataset. The phases and abbreviations considered in the modelling and the corresponding *a–x* models appropriate for each system are listed in Appendix 4.

Phase relations for granite with evidence for in situ partial melting (GSWA 195826) were modelled in the chemical system NCKFMASHTO, which is the most appropriate system for melt-bearing equilibria (White et al., 2001, 2007, 2011, 2014a). The metamorphosed alkaline granite sample (GSWA 183207) contains low K_2O (<0.25 mol.%, Table 2) and no evidence for K_2O-bearing phases; therefore, subsolidus phase relations for this sample were calculated in the mafic system NCFMASHTO (Na_2O–CaO–FeO–MgO–Al_2O_3–SiO_2–H_2O–TiO_2–Fe_2O_3). Subsolidus phase relations for the metasedimentary schist samples were calculated in the chemical system MnNCKFMASHTO (MnO–Na_2O–CaO–K_2O–FeO–MgO–Al_2O_3–SiO_2–H_2O–TiO_2–Fe_2O_3). These calculations included MnO, because even a small amount of Mn can have an important effect on stabilizing garnet to lower pressures than is predicted by modelling in MnO-free systems (e.g. Mahar et al., 1997; Tinkham et al., 2001; White et al., 2014b). Similarly, the garnet amphibolite (GSWA 208362) contains appreciable MnO (~0.45 mol.%, Table 2); therefore, calculations for this sample were performed in the mafic system Na_2O–CaO–FeO–MgO–Al_2O_3–SiO_2–H_2O–TiO_2–Fe_2O_3 with Mn-bearing end-members used for garnet and ilmenite (MnNCFMASHTO).

Subsolidus mineral assemblages for the metasedimentary schists, the garnet amphibolite, and the alkaline granite are considered to have equilibrated in the presence of a pure H_2O supercritical volatile phase. Therefore, these samples were modelled in an H_2O-saturated system. The H_2O content used in the modelling of the granite with evidence for incipient melting (GSWA 195826) was adjusted so that the final phase assemblage is stable just above the solidus, assumed to reflect the conditions at which this assemblage would have been in equilibrium with the last remnants of melt (e.g. White et al., 2004; Diener et al., 2008).

The appropriate O (for Fe^{3+}) content for the metasedimentary schist samples was evaluated using T–M_O diagrams, which allow the effect of Fe_2O_3 on the phase equilibria to be assessed over the range from all Fe as Fe^{2+} to all Fe as Fe^{3+} (e.g. Diener and Powell, 2010; Korhonen et al., 2012). The schist samples considered in this study show evidence for significant weathering and retrograde oxidation; therefore, the Fe_2O_3:FeO proportion determined by Fe^{2+} titration will likely be a maximum value. Uncertainty in Fe^{3+} content and its potential effect on the phase equilibria is illustrated in more detail below for GSWA 88436; the results for each sample are also described. The granite samples are less weathered than the schist samples, and the Fe_2O_3:FeO proportion determined by Fe^{2+} titration was shown to be a suitable estimate of O content. Therefore, the *P–T* pseudosections were constructed using this value.

P–T–X pseudosections

GSWA 195851: semipelitic schist, Nick Belt

A T–M_O pseudosection at 4 kbar (Fig. 4.1a) was used to determine the appropriate O content for GSWA 195851. The selected pressure of 4 kbar was considered a reasonable estimate for initial modelling based on the preserved greenschist facies assemblage. The variation in M_O corresponds to a range of possible O contents from a very low value (= 7% Fe as Fe^{3+}) to the O content determined by Fe^{2+} titration (= 62% Fe as Fe^{3+}). The observed metamorphic assemblage comprising chlorite–muscovite–magnetite–ilmenite–quartz–plagioclase (–inferred H_2O) is stable at temperatures above 480°C at M_O contents >0.35. Hematite is predicted to be stable at higher M_O contents, although sparse hematite observed in thin section is interpreted to be a post-peak phase related to alteration. Based on the predicted mineral assemblages across the range of Fe^{3+} contents, a M_O value of 0.1 (= 12% Fe as Fe^{3+}; grey bar in Fig. 4.1a) was selected as the best estimate of Fe^{3+} content during peak metamorphism.

The *P–T* pseudosection for GSWA 195851 allows the mineral assemblages to be evaluated over a range of pressure and temperature (Fig. 4.1b), and was constructed using the adjusted O content constrained by the T–M_O pseudosection. The peak assemblage (chl–mu–mt–ilm–q–pl–H_2O) is predicted to be stable within a temperature range of 460–550°C at pressures below 6.4 kbar

Table 1. Summary of samples analysed in this study

Sample	*GSWA Site ID*	*Easting*	*Northing*	*Sample description*	*Peak metamorphic assemblage*	*P–T estimate*[a]	*SHRIMP U–Pb geochronology*	
							Mineral	Age (Ma)
Western part of study area: Nick Belt (north to south)								
195851	SPJGAS001256	334171	7326433	semipelitic schist	chl–mu–mt–ilm–q–pl (+ H_2O)	460–550°C, < 6.4 kbar	–	
195852	SPJGAS001543	329736	7326032	semipelitic schist	g–bi–chl–mu–q–mt–ru (+ H_2O)	500–560°C, 3.4 – 5.2 kbar	–	
195853	SPJGAS001258	334432	7325558	semipelitic schist	chl–mu–and–mt–q–pl–hem (+ H_2O)	490–570°C, > 4.6 kbar	–	
188998	SPJGAS001258	334432	7325558	semipelitic schist	chl–mu–and–mt–q–pl–hem (+ H_2O)	–	monazite	age spread from 1796 ± 65 to 1218 ± 13; 1750 ± 35 (Group M); c. 1220 (Group M2)
188999	SPJGAS001273	333487	7324334	semipelitic schist	chl–mu–mt–ilm–q ± pl (+ H_2O)	–	monazite	1187 ± 7
208363	SPJGAS001279	336792	7321056	staurolite schist	st–bi–mu–q–pl–mt–ilm (+ H_2O)	535–650°C, > 2.6 kbar	–	
36493	SJWMTS003453	332202	7319245	pelitic schist	st–g–mu–bi–q–pl ± ilm ± mt (+ H_2O)	–	monazite	1206 ± 6
208364	SPJGAS001849	332242	7319220	pelitic schist	st–g–mu–bi–q–pl ± ilm ± mt (+ H_2O)	550–635°C, 3.6 – 6.5 kbar	–	
Eastern part of study area (north to south)								
Tommie Well								
88436	SXSEUD6599	385189	7308356	staurolite schist	st–bi–mu–q–pl–ilm ± mt (+ H_2O)	550–630°C, 3.6 – 5.9 kbar	monazite	1281 ± 3 (Group M); 1243 ± 7 (Group M2); age spread from 1215 ± 5 to 1143 ± 7 (Group P)
							xenotime	three distinct spread of ages: from 1353 ± 13 to 1312 ± 7 (Group M); from 1210 ± 7 to 1159 ± 7 (Group M2); 1677–1497 (Group P)
208362	SPJGAS001847	385150	7308344	garnet amphibolite	hb–g–ttn–pl–ilm–q (+ H_2O)	565–640°C, 4.6 – 6.2 kbar	–	
Tetlow Granite, New Well								
183207	SXSEUD6681	392922	7297584	metamorphosed alkaline granite	g–cpx–ep–pl–sph–mt–q (+ H_2O)	from 500–530°C @ 2 kbar to 690–720°C @ 7 kbar	titanite	poorly defined, Mutherbukin age[b]

Table 1. continued

Sample	*GSWA Site ID*	*Easting*	*Northing*	*Sample description*	*Peak metamorphic assemblage*	*P–T estimate*[(a)]	*SHRIMP U–Pb geochronology*	
							Mineral	Age (Ma)
Metasomatized margin of pegmatite, New Well 10								
88475	SXSEUD6692	393149	7294279	metasomatic schist	mu–bi–q–tourmaline (+ H_2O)	–	monazite	age spread from 1790 ± 5 to 933 ± 10; 1780 ± 2 (Group M); 1171 ± 4 (Group M2); 958 ± 16 (Group M3)
							xenotime	1805 ± 9 (Group M); one grain with age spread from 1269 ± 9 to 1182 ± 7
Nardoo Well								
46981	SJW539	404279	7296975	pelitic schist	and–chl–mu–bi–q–ilm (+H_2O)	–	monazite	1272 ± 9
							xenotime	age spread from 1572 ± 19 to 1168 ± 22
Davey Well Granite								
195826	SXSGAS008458	372898	7283465	monzogranitic gneiss	bi–ksp–pl–ttn–ep–q–ilm–liq	> 650°C, 4.4–7 kbar	zircon	1664 ± 8 (Group I; igneous crystallization age); 1321 ± 40 (Group M; metamorphism); 1200 ± 3 (Group M2; crystallization of partial melt)

NOTES: – not applicable
(a) based on phase equilibria modelling (see text for further information)
(b) preliminary age (B Rasmussen, written comm., 6 March)
Complete U–Pb data for phosphates and zircon are provided in Appendices 1 and 2, respectively.

Table 2. Bulk compositions

Sample	*195851*	*195852*	*195853*	*208363*	*208364*	*88436*	*208362*	*183207*	*195826*
XRF whole rock compositions (wt%)									
SiO_2	57.22	60.55	56.74	56.42	68.44	63.60	49.83	63.18	68.79
TiO_2	0.97	0.94	0.83	0.79	0.69	0.70	1.49	1.10	0.82
Al_2O_3	20.85	19.78	21.05	20.87	14.14	18.41	16.14	15.28	13.15
Fe_2O_3[(a)]	5.35	4.65	8.61	11.95	6.07	2.65	2.22	3.23	2.18
FeO[(a)]	2.95	2.90	1.47	0.86	1.20	4.20	11.02	1.19	3.02
MnO	0.08	0.09	0.06	0.08	0.18	0.03	0.47	0.06	0.12
MgO	3.26	1.89	1.68	1.65	1.89	2.14	4.08	1.01	1.25
CaO	0.02	0.03	0.05	0.03	0.14	0.70	12.31	8.53	2.60
Na_2O	0.95	0.54	1.21	0.66	0.25	1.80	0.73	4.93	2.22
K_2O	3.93	4.54	4.04	3.79	3.31	3.39	0.19	0.33	4.66
LOI	3.93	3.61	3.52	2.53	3.01	1.28	0.28	0.70	0.54
Total	99.51	99.52	99.26	99.63	99.32	98.90	98.76	99.55	99.35
Normalized molar proportion used for phase equilibria modelling[(b)]									
SiO_2	66.92	70.59	66.15	66.08	77.11	71.38	54.20	67.88	73.51
TiO_2	0.86	0.82	0.73	0.70	0.59	0.59	1.22	0.88	0.65
Al_2O_3	14.37	13.59	14.46	14.41	9.39	12.18	10.34	9.67	8.28
O	0.45	0.68	2.28	0.86	0.48	0.84	0.22	1.31	0.88
FeO	7.60	6.91	8.99	11.37	6.27	6.18	11.84	3.68	4.46
MnO	0.08	0.09	0.06	0.08	0.17	0.03	0.44	–	–
MgO	5.69	3.29	2.91	2.88	3.18	3.58	6.62	1.61	2.00
CaO	0.02	0.03	0.06	0.03	0.17	0.84	14.35	9.82	2.93
Na_2O	1.08	0.61	1.37	0.75	0.27	1.95	0.77	5.14	2.31
K_2O	2.93	3.38	3.01	2.83	2.38	2.43	–		3.18
H_2O	–[(c)]	–[(c)]	–[(c)]	–[(c)]	–[(c)]	–[(c)]	–[(c)]	–[(c)]	1.81
Total	100	100	100	100	100	100	100	100	100

NOTES: (a) FeO analysed by Fe^{2+} titration; Fe_2O_3 contents calculated by difference
(b) final composition used for *P–T* pseudosection, based on adjusted FeO:Fe_2O_3 (see Appendix 4 and text for further details)
(c) assumes H_2O saturation
LOI loss on ignition

(Fig. 13). At higher pressures, garnet is predicted to be stable. The upper and lower temperature limits for the peak metamorphic assemblage are constrained by the appearance of biotite and hematite, respectively.

GSWA 195852: semipelitic schist, Nick Belt

A $T–M_O$ pseudosection at 4 kbar (Fig. 4.2a) was constructed from a very low value (= 3% Fe as Fe^{3+}) to the O content determined by Fe^{2+} titration (= 59% Fe as Fe^{3+}). The observed metamorphic assemblage of garnet–biotite–chlorite–muscovite–quartz–magnetite–rutile(–inferred H_2O) is stable at temperatures below 550°C at M_O contents <0.35, reflecting relatively reduced bulk compositions. At higher M_O contents, biotite is no longer stable, followed by the appearance and disappearance of staurolite. Andalusite is predicted to be stable at M_O contents <0.5. Based on the predicted mineral assemblages, a M_O value of 0.3 (= 20% Fe as Fe^{3+}; grey bar in Fig. 4.2a) was selected as the best estimate of Fe^{3+} content during peak metamorphism. These results confirm that the Fe_2O_3:FeO proportion based on Fe^{2+} titration is not an appropriate value to investigate the conditions during peak metamorphism, and that the samples have undergone retrograde oxidation. This approach assumes that post-peak retrogression did not have a significant effect on the mobility of other components.

The *P–T* pseudosection for this sample shows that the peak assemblage (g–bi–chl–mu–q–mt–ru–H_2O) is predicted to be stable within a temperature range of 500–560°C at pressures between 3.4 and 5.2 kbar (Figs 13 and 4.2b). Plagioclase is stable at lower pressures, although the predicted abundance in the g–bi–chl–mu–pl–q–mt–ru–H_2O field is insignificant (<0.002 mol.%), which in reality cannot be distinguished from the plagioclase-absent field at higher pressures. The stability of biotite at temperatures above 500°C defines the lower temperature limit for the peak metamorphic assemblage, whereas the stability of staurolite at temperatures above 560°C defines the upper temperature limit.

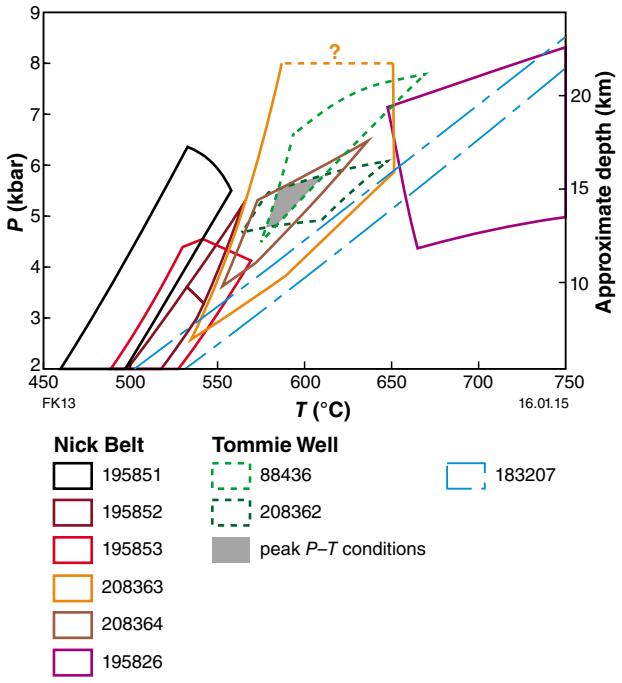

Figure 13. Summary of the phase equilibria modelling, showing the *P–T* stability field of the inferred peak assemblage for each modelled sample. See text and Appendix 4 for further information

GSWA 195853: semipelitic schist, Nick Belt

The preserved metamorphic assemblage in this sample comprises chlorite–muscovite–andalusite–magnetite–quartz–plagioclase–ilmenite/hematite(–inferred H_2O). A T–M_O pseudosection was constructed at 4 kbar from a low M_O value to the O content determined by Fe^{2+} titration (= 84% Fe as Fe^{3+}; Fig. 4.3a). The observed assemblage is stable at temperatures below 565°C between M_O contents of 0.5 and 0.98. Staurolite is stable at lower M_O contents and magnetite is not stable at higher M_O contents. Based on these observations, a M_O value of 0.6 (= 51% Fe as Fe^{3+}; grey bar in Fig. 4.3a) was determined to be an appropriate estimate of Fe^{3+} content.

The peak assemblage (chl–mu–and–mt–q–pl–hem–H_2O) is predicted to be stable at temperatures between 490 and 570°C at pressures up to 4.6 kbar (Figs 13 and 4.3b). The stability of andalusite defines the lower temperature limit and the upper pressure limit for the peak metamorphic assemblage. The stability of chlorite constrains the upper temperature limit.

GSWA 208363: staurolite schist, Nick Belt

A T–M_O pseudosection at 4 kbar (Fig. 4.4a) was constructed from a low M_O value to the O content determined by Fe^{2+} titration (= 93% Fe as Fe^{3+}). The observed metamorphic assemblage of staurolite–biotite–muscovite–quartz–plagioclase–magnetite–ilmenite (–H_2O) is stable at temperatures between 550 and 595°C for M_O contents <0.2. Ilmenite is not stable at higher M_O contents, followed by the appearance of andalusite. Based on these constraints, a M_O value of 0.1 (= 15% Fe as Fe^{3+}; grey bar in Fig. 4.4a) was selected as the best estimate of Fe^{3+} content during peak metamorphism.

The peak assemblage (st–bi–mu–q–pl–mt–ilm–H_2O) defines a broad field, with a temperature range between 535 and 650°C at pressures above 2.6 kbar (Figs 13 and 4.4b). The H_2O-saturated solidus defines the upper temperature limit and the appearance of chlorite defines the lower temperature limit. Andalusite is stable at lower pressures, whereas the upper pressure limit is not well constrained (>8 kbar; Fig. 4.4b).

GSWA 208364: pelitic schist, Nick Belt

The observed metamorphic assemblage in this sample is composed of garnet–staurolite–biotite–muscovite–plagioclase–quartz–magnetite–ilmenite. However, fine-grained plagioclase only occurs as a minor phase in the matrix; therefore, its relationship with the peak assemblage is ambiguous. The T–M_O pseudosection calculated at 4 kbar ranges from a low M_O value to the O content determined by Fe^{2+} titration (= 82% Fe as Fe^{3+}), and predicts this assemblage (+ pl–H_2O) to be stable at temperatures between 555 and 580°C for M_O contents <0.3 (Fig. 4.5a). Andalusite is stable at higher M_O contents, followed by the disappearance of staurolite. Based on these constraints, a M_O value of 0.15 (= 15% Fe as Fe^{3+}; grey bar in Fig. 4.5a) was used to construct the P–T pseudosection.

The P–T pseudosection shows that the peak assemblage (g–st–bi–mu–pl–q–mt–ilm–H_2O) is stable at temperatures between 550 and 635°C at pressures from 3.6 to 6.5 kbar (Figs 13 and 4.5a). However, the possible interpretation that plagioclase is retrograde would stabilize the peak assemblage to higher pressure.

GSWA 88436: staurolite schist, Tommie Well

The observed peak metamorphic assemblage in GSWA 88436 comprises staurolite–biotite–muscovite–quartz–plagioclase–ilmenite(–H_2O). The stability of this assemblage (± garnet) is highly sensitive to variations in Fe^{3+} content; therefore, this sample is used to illustrate in more detail the influence of Fe^{3+} on the phase equilibria. An initial T–M_O pseudosection was constructed at 4 kbar (Fig. 4.6a) with M_O contents ranging from a very low Fe^{3+} content to the O content determined by Fe^{2+} titration (= 36% Fe as Fe^{3+}). The peak assemblage (+ minor magnetite) is stable within a temperature range of 560–580°C at M_O contents <0.55. Andalusite is stable at higher M_O contents for a similar range of temperature, and at M_O contents >0.75 staurolite is no longer stable. Based on these observations at 4 kbar, a M_O value of 0.3 (= 11% Fe as Fe^{3+}; grey bar in Fig. 4.6a) could be a suitable estimate of Fe^{3+} content during peak metamorphism.

A second $T–M_O$ pseudosection was constructed at 5 kbar (Fig. 4.6b). At these conditions, the peak assemblage (+ minor magnetite) is stable at temperatures above 575°C across the range of M_O contents. However, garnet is stabilized at temperatures between 555 and 575°C for M_O contents <0.7. The initial estimate of Fe^{3+} content (11% Fe as Fe^{3+}; Fig. 4.6a) predicts the growth of garnet during heating at 5 kbar, followed by its subsequent breakdown and growth of staurolite (Fig. 4.6b). Although garnet is observed in some compositional layers at this locality, the sample volume of GSWA 88436 does not contain any visible peak or relict garnet in the hand sample or in the thin section, suggesting that GSWA 88436 did not pass through garnet stability during metamorphism. These observations imply that either peak pressures did not reach 5 kbar or that the initial estimate of Fe^{3+} content was too low. A more appropriate estimate of Fe^{3+} content which is consistent with the absence of garnet in this sample is a higher M_O value of 0.75 (= 30% Fe as Fe^{3+}; grey bar in Fig. 4.6b).

The effect of these slight differences in Fe^{3+} content on the *P–T* stability of the inferred peak assemblage (st–bi–mu–q–pl–mt–ilm–H_2O) is shown in Figure 4.6c. The peak field extends to higher pressures and temperatures and is stable over a wider *P–T* range for more oxidized bulk compositions (Fig. 4.6c). Although a more reduced bulk composition provides a more conservative estimate of peak metamorphic conditions, there is no evidence for garnet stability in GSWA 88436. Based on these constraints, a slightly higher Fe^{3+} content (= 30% Fe as Fe^{3+}; Fig. 4.6b) is the preferred interpretation.

The *P–T* pseudosection was constructed using this higher O content (Fig. 4.6d). The peak assemblage is predicted to be stable at temperatures between 575 and 670°C at pressures from 4.2 to 7.9 kbar (Figs 13 and 4.6d). The appearance of chlorite and sillimanite at the expense of staurolite define the lower and upper temperature limits, respectively, and garnet is stable at pressures higher than 6 kbar.

GSWA 208362: garnet amphibolite, Tommie Well

The $T–M_O$ pseudosection (Fig. 4.7a) was constructed from a low M_O value to the O content determined by Fe^{2+} titration (= 15% Fe as Fe^{3+}). The observed metamorphic assemblage of hornblende–garnet–titanite–plagioclase–quartz–ilmenite(–H_2O) is stable at temperatures between 550 and 610°C at M_O contents less than 0.75. Epidote is stable at higher M_O contents. A M_O value of 0.20 (= 4% Fe as Fe^{3+}; grey bar in Fig. 4.7a) was used to construct the *P–T* pseudosection.

Using this value, the *P–T* pseudosection shows that the peak assemblage (hb–g–ttn–pl–ilm–q–H_2O) occurs between temperatures of 565 and 640°C and pressures of 4.65 and 6.2 kbar (Figs 13 and 4.7b). Diopside and epidote are predicted to be stable at higher and lower temperatures, respectively. The stability of titanite defines the lower pressure limit and ilmenite defines the higher pressure limit. Chlorite is predicted at temperatures less than 530°C (Fig. 4.7b,c), although the maximum temperatures for chlorite stability might be slightly underestimated due to the absence of a Mn-bearing end-member used in the modelling for this sample.

GSWA 183207: metamorphosed alkaline granite, New Well

The preserved assemblage in this sample comprises garnet–clinopyroxene–hornblende–epidote–plagioclase–titanite–(titano)magnetite–quartz. However, hornblende typically occurs as small inclusions in clinopyroxene and is not interpreted to be part of the peak equilibrium assemblage. The *P–T* pseudosection for GSWA 183207 (Fig. 4.8) has several small fields at temperatures below 600°C above 4 kbar as clino-amphiboles (e.g. actinolite and glaucophane) become stable. However, at higher temperatures the topology becomes increasingly simplified, with the appearance of garnet followed by the disappearance of epidote. Silicate melt may be stable at higher temperatures than those shown on the *P–T* pseudosection (Fig. 4.8). However, the current *a–x* model for silicate melt is only appropriate for haplogranitic compositions (e.g. White et al., 2007, 2011); therefore, phase relations involving melt cannot be reliably modelled for intermediate or mafic bulk compositions. The inferred peak assemblage (g–cpx–ep–pl–sph–mt–q–H_2O) is stable over 30°C across the entire range of modelled temperature (500–750°C) up to 8.5 kbar (Figs 13 and 4.8). Although the peak phase field defines a narrow temperature interval of 25°C over the range of modelled pressures, there is no pressure constraint provided by the sample.

GSWA 195826: monzogranitic gneiss, McCarthy Well

The preserved assemblage in this sample is biotite–K-feldspar–plagioclase–titanite–epidote–quartz–ilmenite. Evidence for incipient melting is well preserved in this sample, including inferred former melt films along grain boundaries (Fig. 6e,f) and resorbed biotite. These petrographic observations are also consistent with the presence of small crystallized melt pockets and veins at the outcrop scale (Fig. 4e,f). Therefore, the peak metamorphic assemblage would have included silicate melt. The *P–T* pseudosection for GSWA 195826 predicts a simple topology, with the main temperature constraint being the H_2O-saturated solidus between 650 and 700°C over the range of modelled pressures. The inferred peak assemblage (bi–ksp–pl–ttn–ep–q–ilm–liq) is stable at temperatures above 650°C between 4.4 and 7 kbar (Figs 13 and 4.9). The absence of titanite at higher pressures defines the maximum pressure for the peak assemblage, and the absence of epidote at lower pressures defines the minimum pressure.

Discussion

Pressure–temperature–time (*P–T–t*) evolution

The samples from north to south across the Mutherbukin Zone record progressively higher metamorphic grade, from greenschist to upper amphibolite facies conditions. The lowest *P–T* conditions are recorded by magnetite-bearing schists in the northern part of the Nick Belt, with temperatures below 550°C and pressures less than 6 kbar (Fig. 13). The highest conditions in the Nick Belt, recorded by staurolite(–garnet)-bearing schists in the south, broadly overlap with the *P–T* constraints from staurolite-bearing schists and garnet amphibolites at Tommie Well, with peak conditions estimated at 550–670°C and 3.6 – 7.9 kbar (Fig. 13). The highest grade rocks occur in the central part of the Mutherbukin Zone at McCarthy Well, where monzogranitic gneisses show evidence for in situ melting. Peak metamorphic conditions are estimated at >650°C at 4.4 – 7 kbar.

Garnet zoning

In garnet-bearing rocks, differences in chemical composition across garnet porphyroblasts (i.e. chemical zoning) potentially record changes in *P–T–X* conditions during mineral growth (e.g. Spear and Selverstone, 1983; St-Onge, 1987; Carlson, 2011). These chemical changes can be used to better define both peak metamorphic conditions and the *P–T* path of the rock. Garnet-bearing lithologies are present in the Nick Belt and at Tommie Well.

Nick Belt

The garnet porphyroblasts in the samples from the Nick Belt preserve a simple zonation pattern (Fig. 7c–j). The *P–T* pseudosection for the staurolite–garnet schist (GSWA 208364; Fig. 14a) is contoured for X_{Alm}, X_{Sps}, and garnet mode (approximate molar proportions (mol.%) equivalent to volume; Fig. 14b). The porphyroblasts show a gradual increase and decrease in X_{Alm} and X_{Sps} respectively, from core to rim, consistent with growth during prograde metamorphism. The composition of the cores ($X_{Alm} \geq 0.62$; $X_{Sps} \leq 0.28$; Fig. 7c–f) indicate approximate conditions of ~2.5 kbar and 520°C (Fig. 14b), although these isopleths for X_{Alm} and X_{Sps} do not precisely intersect, suggesting possible issues with the *a–x* models, diffusional relaxation and uncertainties in the bulk composition or mineral chemistry, particularly with Fe^{3+} contents. The rim compositions ($X_{Alm} \leq 0.75$; $X_{Sps} \geq 0.08$; Fig. 7c–f) are most consistent with equilibration in the narrow g–st–bi–chl–mu (+ q, mt, ilm, H_2O) field at ~7 kbar and 580°C, although the inferred peak assemblage of g–st–bi–mu (+ q, mt, ilm, H_2O ± pl) becomes stable at temperatures only 10°C higher (at the same pressure). However, the presence of plagioclase in the equilibrium assemblage would indicate peak conditions at slightly lower pressures. One possible explanation for the difference between the rim compositions and the observed assemblage is that a minor amount of garnet is predicted to be consumed

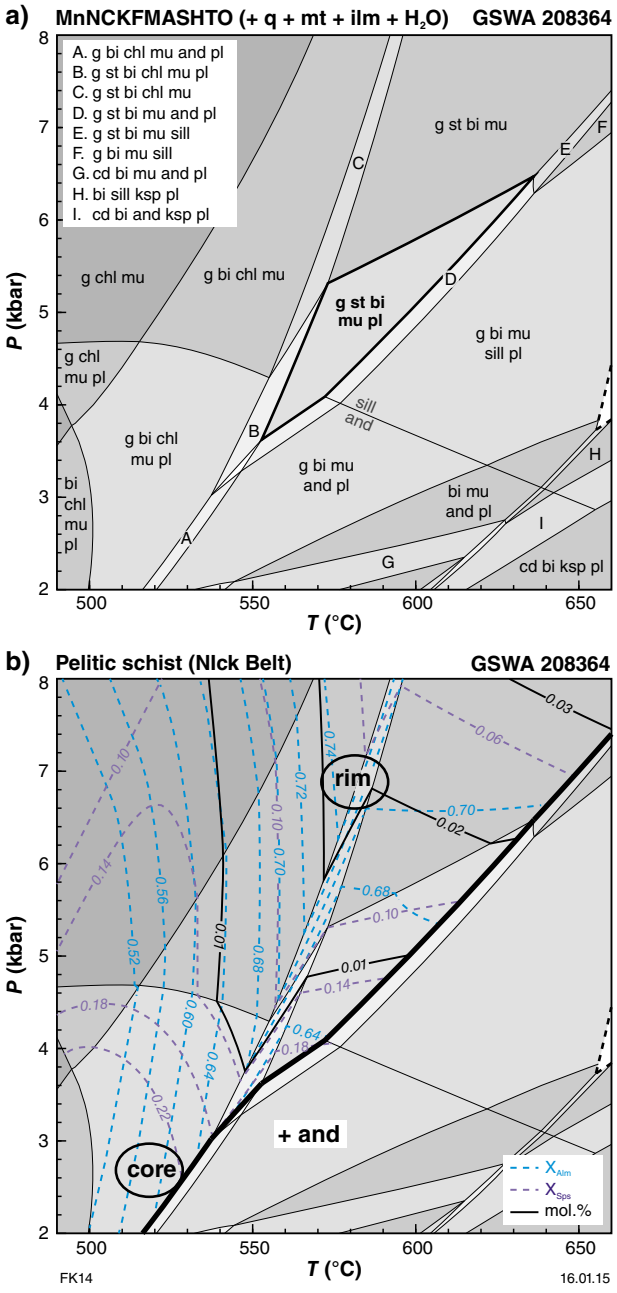

Figure 14. ***P–T*** **pseudosection for garnet-bearing pelitic schist from the Nick Belt (GSWA 208364): a) Labelled *P–T* pseudosection — peak field denoted by thicker lines; solidus shown by thicker dashed line; b) compositional isopleths and proportion (in mol.%) of garnet. Black ellipses denote approximate *P–T* conditions for garnet cores and rims; sizes are schematic and do not correspond to errors. Garnet data is not shown for andalusite-bearing assemblages to the right of the thick solid line (labelled '+ and')**

passing from the g–st–bi–chl–mu (+ q, mt, ilm, H_2O) field to the peak field (± pl), with additional garnet resorption during decompression. Therefore, it is likely that the garnet rims which equilibrated with the peak assemblage have not been preserved. Given these uncertainties, the

best estimate of peak metamorphic conditions ranges from 570°C, 5 kbar to 640°C, 7 kbar (Fig. 14b). These observations support an overall clockwise *P–T* trajectory with an increase in pressure and temperature to conditions of peak metamorphism.

Tommie Well

The *P–T* pseudosection for the garnet amphibolite (GSWA 208362; Fig. 15a) is contoured for X_{Alm}, X_{Grs}, X_{Sps}, and garnet mode (Fig. 15b). Four growth domains (gI, gII, gIII and gIV; Fig. 8a) are preserved in the garnet, which can be broadly correlated with predicted garnet compositions on the *P–T* pseudosection. The increase in X_{Grs} and decrease in X_{Alm} and X_{Sps} across garnet I and garnet II is suggestive of growth zoning during prograde metamorphism. However, with progressive garnet growth from core to rim, the predicted X_{Sps} component appears to increasingly deviate from observed values (Figs 7g–j and 15b). This deviation will also have an effect on the other garnet components, especially X_{Alm} because garnet and ilmenite are the only phases with Mn-bearing end-members used in the *a–x* models for this sample. There are three possible explanations for the discrepancy. First, uncertainties in the bulk composition, especially in the Fe^{3+} content, could cause a deviation between predicted and measured compositions. Second, the Mn-bearing *a–x* models used in this study are recognized as having large inherent inconsistencies. Updated Mn-bearing models for pelitic minerals have just recently become available (White et al., 2014b), although these updates do not currently include Mn-bearing *a–x* models for mafic systems. Therefore, the X_{Sps} contents (and consequently X_{Alm}) will have potentially significant uncertainties and care should be applied to appropriately interpret the data (e.g. Powell and Holland, 2008). A third factor for the discrepancy is that the presence of zoned porphyroblasts implies that the effective bulk composition will be incrementally modified during garnet growth. The effects of this fractionation will be minor for most components. However, most of the MnO in the bulk composition is hosted in garnet, and as the Mn-rich core becomes increasingly isolated during progressive growth, the effective bulk composition becomes more depleted in MnO compared with the bulk composition used in the phase equilibria modelling. Therefore, the predicted compositions will potentially overestimate the X_{Sps} component, especially during the later stages of garnet growth (i.e. the rim).

The X_{Grs} content likely provides the most reliable constraint since Ca diffuses more slowly in garnet than Fe, Mg and Mn (e.g. Carlson, 2006; Vielzeuf et al., 2007). In addition, compared with the measured composition, the predicted X_{Sps} and X_{Alm} contents at a specific X_{Grs} value appear to be, respectively, underestimated and overestimated. This issue may relate to the limitations of the *a–x* models, as discussed above. Decreasing X_{Alm} and increasing X_{Sps} by the same proportions generally provides a better fit with the measured X_{Grs} value, confirming the interdependence of these variables in the model. Taking these discrepancies into consideration, the intersection of the X_{Alm}, X_{Grs}, and X_{Sps} isopleths which generally define the composition of the garnet core (gI; $Alm_{39–43}Grs_{30–33}Sps_{22–27}Prp_3$), constrain *P–T* conditions

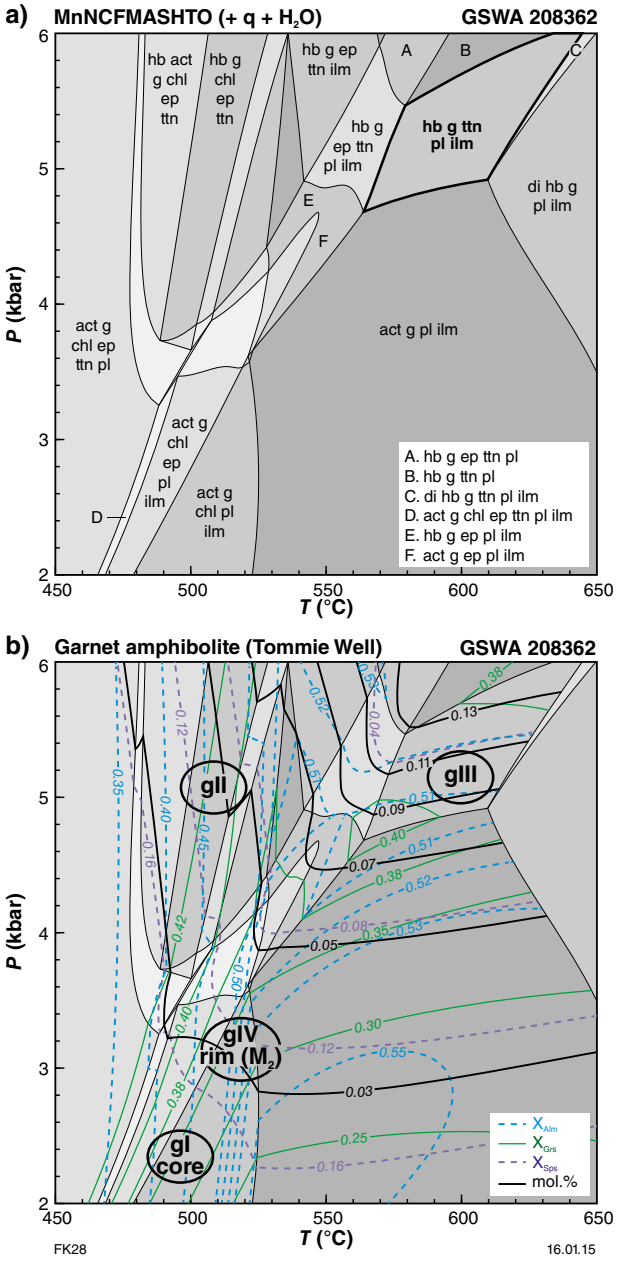

Figure 15. ***P–T*** **pseudosections for garnet-bearing amphibolite from Tommie Well (GSWA 208362): a) Labelled *P–T* pseudosection; peak field denoted by thicker lines. See Fig. 4.7 for fully labelled diagram; b) compositional isopleths and proportion (in mol.%) of garnet; black ellipses denote approximate *P–T* conditions for garnet domains shown in Fig. 8**

to ~2.2 kbar and 500°C (Fig. 15b). Extrapolating the 2σ errors of the calculated isopleths (not shown), the maximum pressure constraint for the intersection of these isopleths is about 2.5 kbar. The composition of the innermost inclusion-rich mantle (gII; $Alm_{36}Grs_{41}Sps_{21}Prp_2$) is consistent with conditions in the peak phase field (hb–g–ttn–pl–ilm–q–H_2O) around 5 kbar and 600°C. The predicted garnet composition in this field generally correlates with the measured X_{Grs} content, although X_{Sps}

and X_{Alm} contents are underestimated and overestimated by about 0.15. However, X_{Grs} contents do not change significantly at temperatures above 500°C at 5 kbar, which is the minimum temperature constraint provided by the garnet II composition. The composition of the rim (gIV; $Alm_{54}Grs_{31}Sps_{11}Prp_4$) records final equilibration of the garnet at ~3.2 kbar and 520°C (Fig. 15b), although this estimate potentially has significant uncertainty due to the effects of Mn fractionation during garnet growth. As shown by the mol.% garnet contours in Figure 15b, more than 30% of the garnet mode is predicted to be consumed between the maximum *P–T* conditions (~5 kbar, 600°C) and the lower grade conditions estimated from the composition of garnet IV. Therefore, the thin mantle of garnet III between garnet II and garnet IV cannot be new garnet growth, and is interpreted to be a zone of incomplete diffusive resetting. Based on these interpretations, the proposed *P–T* path has an overall clockwise trajectory with maximum conditions of ~5 kbar and 600°C, followed by decompression and cooling.

The flat X_{Grs} profile and distribution of quartz and titanite inclusions that distinguish the 40 µm-wide rim (gIV) from the adjacent domain (gIII) supports the interpretation that the rim zone is a second generation of garnet growth, which requires a concomitant increase in temperature and pressure (Fig. 15b). This generation of garnet growth must have occurred during thickening associated with a second, lower grade event (M2). The other minerals preserved in the sample provide additional information on the overall evolution. The changes in the relative proportion of phases along a clockwise *P–T* path are shown in Figure 16. The path is modelled as a simple two-stage trajectory, with isothermal thickening from 2 to 5 kbar at 500°C, followed by isobaric heating from 500 to 600°C. Although the actual *P–T* path may have been shallower than the one used here, the multivariant mineral reactions during prograde metamorphism would be similar. The modelling indicates that the assemblage in equilibrium at the minimum conditions of garnet II growth (~5 kbar, 500°C) include quartz, ilmenite, titanite, epidote, chlorite, and hornblende (+ inferred H_2O; Fig. 15b). With the exception of ilmenite, these phases occur as inclusions in garnet II in various proportions (Fig. 8). The relative scarcity of epidote and chlorite suggests that they were progressively consumed during garnet growth, as shown by the eventual disappearance of these phases during heating to peak temperature (Fig. 16). Assuming equilibrium, the multivariant reaction occurring during garnet growth at the conditions of M2 metamorphism involved the consumption of chlorite, plagioclase and minor ilmenite to form actinolite and quartz with garnet. Although titanite is predicted to have been completely consumed during retrogression from peak conditions, it occurs as inclusions in garnet and as a minor matrix phase, indicating that metastable titanite persisted to lower grade conditions. Some of the hornblende that makes up the majority of the rock would have grown during retrogression, as well as during the breakdown of chlorite and plagioclase during the M2 metamorphic event (Fig. 15b). However, a significant proportion would have been stable throughout much of the evolution, although its composition would have reequilibrated with the changing *P–T* conditions.

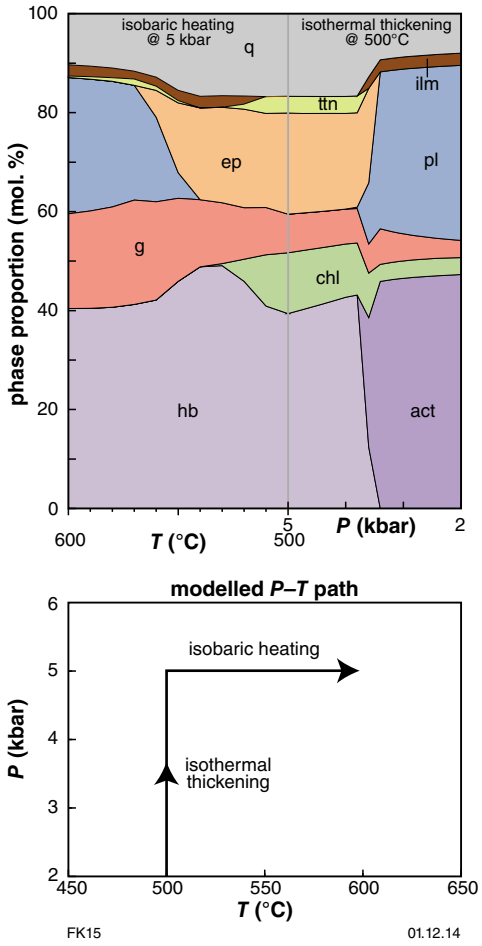

Figure 16. Changes in the relative proportion of phases along the prograde *P–T* path for garnet amphibolite (GSWA 208362; Fig. 15). Prograde path characterized by isothermal thickening from 2 to 5 kbar at 500°C and isobaric heating from 500 to 600°C at 5 kbar

Early thermal metamorphism?

Despite the relatively simple clockwise *P–T* history preserved in both the Nick Belt and at Tommie Well, it is noted that garnet cores from both localities record similar high-*T*, low-*P* conditions (2–2.5 kbar, 500–520°C). These results indicate that these garnet domains grew during metamorphism with apparent thermal gradients in excess of 70°C/km^{-1} before maximum thickening during the Mutherbukin Tectonic Event. Such thermal gradients are extreme for typical crustal thickening during regional metamorphism and more likely record the effects of contact metamorphism. Although the contacts between the schist and the host granites of the Davey Well batholith are commonly faulted, many of the samples were collected near contacts (GSWA 188998, 188999 and 208363) or from small rafts (GSWA 36493, 88436, 208362, 208364)

within the batholith itself (Fig. 3a). Geochronological evidence to support this model is sparse, although xenotime from GSWA 88436 contains some evidence for growth at c. 1670 Ma (n = 3; Group P; Table 1), similar to the age of the Davey Well Granite (Wingate et al., 2009, 2010, 2013; Sheppard et al., 2010b). Following contact metamorphism at c. 1670 Ma, it is likely that the schists cooled and reequilibrated with the ambient thermal gradient (Fig. 17a). Evidence of this cooling event is not preserved in the garnet chemistry, likely due to sluggish kinetics at low temperature. However, cooling would have involved garnet resorption, leading to embayed cores as imaged in the garnet porphyroblasts in GSWA 208364 at Tommie Well (between zones gI and gII; Fig. 8a).

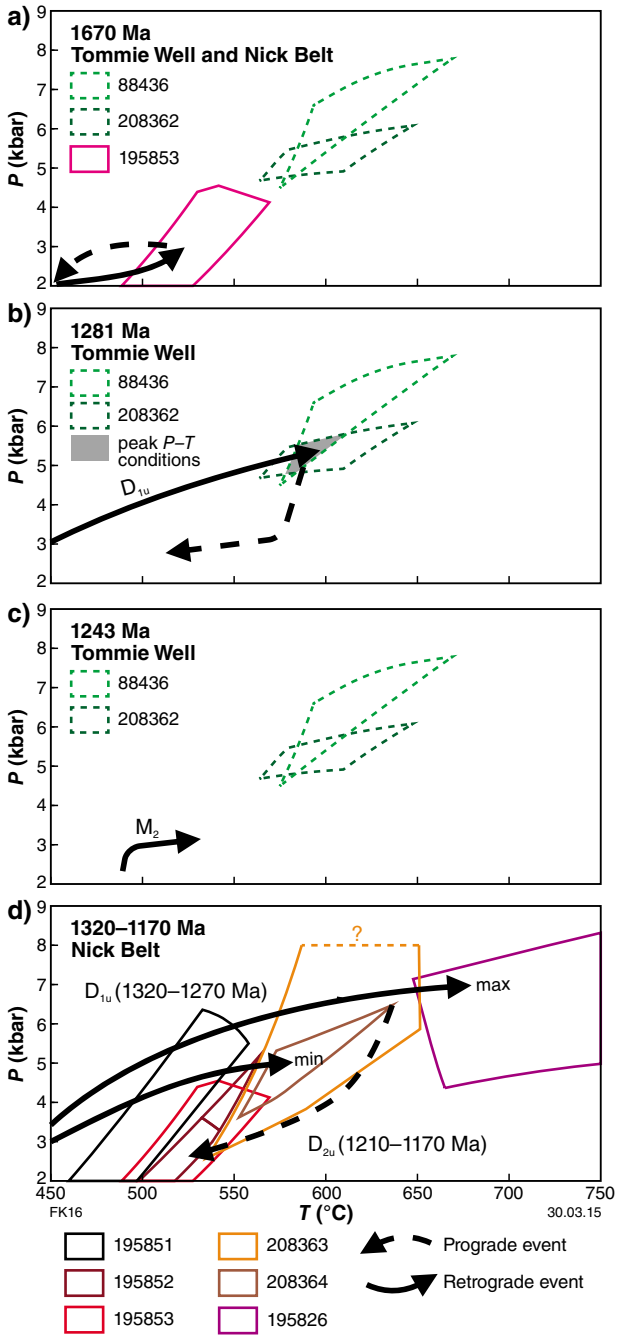

Prograde metamorphism during the Mutherbukin Tectonic Event would have likely started from much lower temperatures than those recorded by the garnet core compositions, although the evolving composition of garnet and associated mineral inclusions during prograde metamorphism would not be significantly different. Peak *P–T* conditions in the Nick Belt reached 570–640°C at 5–7 kbar, those to the south around McCarthy Well reached >650°C at 4.4–7 kbar (Fig. 17d), and those at Tommie Well reached 600°C at 5 kbar (Fig. 17b), with a second event at lower grade conditions (Fig. 17c). Despite the added complexity in the *P–T* path and timing of events at Tommie Well, all the rocks in the Mutherbukin Zone are characterized by a prograde clockwise *P–T* path along a crustal thermal gradient between 35 and 50°C/km^{-1} (Fig. 17).

Timing of events

Despite the prevalence of coaxial structures throughout the Mutherbukin Zone, the absolute timing of peak metamorphism and fabric development can be constrained at a few key localities. At McCarthy Well, high-grade granitic gneisses of the Davey Well batholith record two discrete episodes of fabric generation. The first is a strong gneissic fabric (S_{1u}) related to dextral transpressional shearing on northwest-trending structures, with a top-to-the-west sense of shear. This fabric is overprinted by coplanar transtensional shear fabrics (S_{2u}) that are associated with crystallization of incipient melt produced at peak metamorphic conditions (>650°C, 4.4–7 kbar; GSWA 195826). These rocks (GSWA 195826) record two periods of metamorphic zircon growth. The older component at 1321 ± 40 Ma is interpreted to record the generation of the S_{1u} gneissic fabric during prograde metamorphism and dextral transpression. The younger component at 1200 ± 3 Ma is interpreted to record melt crystallization and fabric/fold generation (S_{2u}) during transtensional deformation and post-peak metamorphic cooling.

Figure 17. Summary of *P–T* paths: a) *P–T* path related to contact metamorphism at c. 1670 Ma, recorded by garnet cores at Tommie Well and the Nick Belt. Schematic retrograde path shown as dashed line; b) *P–T* path from Tommie Well at c. 1281 Ma. Schematic retrograde path shown as dashed line, although trajectory is poorly constrained; c) *P–T* path from Tommie Well at c. 1243 Ma (M2); d) The dominant *P–T* path from the Mutherbukin Zone at c. 1200 Ma has a clockwise trajectory, although peak conditions will vary as a function of crustal depth. The prograde path (D_{1u}) is characterized by thickening of radiogenic crust at 1320–1270 Ma and related thermal response, with peak metamorphism at c. 1200 Ma. The actual *P–T* path may occur within the range defined by the two paths shown, due to uncertainty in the estimates of peak conditions. The termination of crustal heating is driven by extension (D_{2u}) at 1210–1170 Ma. See text for further details. Each figure shows the stability of the inferred peak assemblage fields appropriate for each event, based on the phase equilibria modelling

Numerous studies have shown that in rocks with little or no calcium, monazite is typically formed by at least low greenschist facies and can be stable throughout metamorphism (e.g. Overstreet, 1967; Wing et al., 2003; Rasmussen et al., 2010b; Janots and Rubatto, 2014). In these types of rocks, low-grade monazite may preserve detrital or early metamorphic cores and later metamorphic overgrowths (e.g. Wing et al., 2003; Rasmussen and Muhling, 2007; Rasmussen et al., 2007), which can persist to higher metamorphic grades with variable recrystallization. Likewise, xenotime may form during diagenesis (McNaughton et al., 1999), and low- to high-grade metamorphism, with incomplete recrystallization preserving evidence for multiple generations of growth (Rasmussen et al., 2011). The bulk compositions of the metasedimentary schists in the Nick Belt have low CaO contents (≤0.7 wt%; Table 2), comparable with those from other areas with lower greenschist facies monazite (Wing et al., 2003). Therefore, the monazite grains observed in the lower-grade samples from the northern Nick Belt are interpreted to have grown or been recrystallized during greenschist facies metamorphism. The lowest grade samples contain a strong S_{1u} schistosity with a locally well-developed L_{1u} lineation. These rocks contain an assemblage of chlorite–magnetite(–andalusite) attained during peak *P–T* conditions of 460–550°C at <6.4 kbar (GSWA 195851). Sample GSWA 188999 has a similar assemblage and yields a metamorphic monazite age of 1187 ± 7 Ma, interpreted as the age of peak metamorphism. Slightly higher grade samples, defined by chlorite–muscovite assemblages with cm-scale andalusite porphyroblasts that are partially aligned to an S_{2u} crenulation cleavage (490–570°C at >4.6 kbar; GSWA 195853), yield a metamorphic monazite age of 1220 ± 18 Ma (GSWA 188998), also interpreted to date the timing of peak metamorphism. An older age component at c. 1750 Ma (Table 1) indicates that pre-Mutherbukin-aged monazite has survived dissolution and re-precipitation during low-grade metamorphism. These older ages may record evidence of low-grade metamorphism during the 1820–1770 Ma Capricorn Orogeny (Sheppard et al., 2010a). The highest grade schists in the southern part of the belt have assemblages with randomly oriented staurolite and garnet porphyroblasts, which overgrow an earlier S_{1u} fabric. These rocks record peak metamorphic conditions of 550–635°C at 3.6–6.5 kbar (GSWA 208364) and yield a metamorphic monazite age of 1206 ± 6 Ma (GSWA 36493).

The *P–T* path defined by the lithologies at Tommie Well is more complicated, showing two periods of crustal thickening, each followed by cooling and exhumation (Fig. 17b,c). Peak metamorphic conditions are estimated from both the garnet amphibolite (GSWA 208362) and staurolite schist (GSWA 88436) at 5 kbar and 600°C, followed by a second lower grade event. Metamorphic monazite from the staurolite schist yields two age components at 1281 ± 3 Ma and 1243 ± 7 Ma. Although the possibility that these dates record protracted growth during a single event cannot be unequivocally ruled out, the garnet zoning profiles require two separate crustal thickening events. Based on this evidence, the discrete monazite age components are interpreted to record the approximate timing of the two events. However, the isolation of these rocks as a km-scale inclusion within the Davey Well batholith makes it difficult to place the temporal development of the fabrics into a regional context. Inclusion trails within staurolite porphyroblasts suggest that it grew during a period of progressive deformation, culminating in peak metamorphism at c. 1281 Ma. This date is roughly coincident with the timing of D_{1u} deformation recorded at McCarthy Well (1321 ± 40 Ma), as well as the range of poorly constrained ages from xenotime at 1353–1312 Ma. However, the age at c. 1243 Ma has yet to be identified anywhere else in the Mutherbukin Zone. The youngest range of ages provided by both monazite and xenotime at, respectively, 1215–1143 Ma and 1210–1159 Ma, are broadly coeval with peak metamorphism and the generation of S_{2u} fabrics elsewhere in the zone, which may broadly record the development of the locally preserved (S_3) crenulation cleavage.

Elsewhere in the Mutherbukin Zone the structural history of the rocks is less clear due to coaxial reworking; however, metamorphic ages similar to those at McCarthy Well and the Nick Belt have been obtained. A chlorite–andalusite-bearing pelitic schist from Nardoo Well (GSWA 46981) yields a metamorphic monazite age of 1272 ± 9 Ma and poorly constrained xenotime ages as young as c. 1168 Ma. Hydrothermally altered pelitic schist in the margins of a c. 958 Ma pegmatite dyke (GSWA 88475; Sheppard et al., 2007) yields metamorphic monazite dated at 1171 ± 4 Ma with poorly constrained xenotime dates from a single grain ranging from c. 1269 to 1182 Ma (Appendix 2).

The timing of fabric development across the Mutherbukin Zone is relatively well constrained, although lithologies from Tommie Well record a more complicated tectonic history. The earliest fabrics developed in the zone (S_{1u}–L_{1u}) were produced during top-to-the-west-directed crustal thickening between c. 1320 and 1270 Ma. Even though the lowest grade samples in the Nick Belt lack evidence for development of any D_{2u}-related fabrics (as they may be in a zone of low D_{2u}-strain), peak metamorphism across the Mutherbukin Zone appears to be coincident with transtensional D_{2u} deformation at 1210–1170 Ma. This implies that crustal thickening, or a thickened crustal profile, may have been attained for ≥100 Ma. The more complicated history recorded by lithologies at Tommie Well may reflect localized or discrete movements on the Ti Tree Shear Zone, within which the km-scale inclusion is located.

Thermal modelling

To identify the possible heat sources and driving forces for this prolonged event, the metamorphic evolution of the Mutherbukin Zone was investigated using a simple numerical model. The geological constraints include the *P–T* conditions estimated for the metamorphic rocks, the apparent duration of the Mutherbukin Tectonic Event based on the geochronological results, and the present-day crustal profile imaged by the deep seismic reflection survey (Johnson et al., 2011a; 2013b). Calculations were

performed using the software SHEMAT (Clauser, 2003). Heat production values and other rock parameters used in the modelling are listed in Table 3.

The simulation is presented as a two-stage model. The lithospheric profiles are shown in Figure 18a. The upper and lower boundaries of the models are fixed at 10°C at the surface and 1300°C at the base of the lithosphere, assumed to be at 180 km depth. In each of the models, the crust is layered with a sedimentary basin underlain by 4 km-thick Davey Well batholith, 14 km-thick middle crust, and 7 km-thick lower crust. The base of the crust is estimated at a depth of 40 km (Johnson et al., 2013b). The composition of the sedimentary basin is approximated by a representative pelitic rock from the Leake Spring Metamorphics, which has a similar composition to the abundant siltstones of the Edmund Group. The composition of the Davey Well batholith is based on a representative rock composition of the Davey Well Granite which comprises the largest component of the batholith. All data are available from the Geological Survey of Western Australia's GeoChem database (http://geochem.dmp.wa.gov.au/geochem/). The middle crust is assumed to be calc-alkaline granitic gneisses similar to the Dalgaringa Supersuite (e.g. Sheppard et al., 2004), which makes up a significant component of the Glenburgh Terrane (Johnson et al., 2011a; 2013b). The lower crust is inferred to be mafic granulite. Importantly, radiogenic heat production values for the sedimentary basin and the Davey Well batholith are high, with age-corrected values of 4.0 and 5.5 μW m^{-3} (Table 3), respectively. These values are consistent with elevated heat flow and heat production observed in many Australian Proterozoic terranes (e.g. McLaren et al., 2003, 2005).

In the first model, the initial thickness of the sedimentary basin is assumed to be 5 km (Fig. 18a), which is consistent with the low degree of metamorphism recorded in the Leake Spring Metamorphics across most of the Gascoyne Province (Sheppard et al., 2010b). The model is allowed to conductively cool for 300 Ma, representing the period of quiescence between the Mangaroon Orogeny and the Mutherbukin Tectonic Event. This thermal structure is imposed as the starting structure in the subsequent model. In the second model, the thickness of the sedimentary basin is increased to 15 km (Fig. 18a), which is most consistent with the pressure constraints provided by the staurolite(–garnet)-bearing schists and the underlying Davey Well batholith (Fig. 13). The thicknesses of the other units are the same as in the first model. The model is allowed to run for 140 Ma. Predicted surface heat flow based on the modelling ranges from 37 to 51 mW m^{-2}, which is similar to the estimated Proterozoic global average (Morgan, 1984), but less than modern-day average surface heat flow for Australian Proterozoic terranes (McLaren et al., 2005).

The predicted thermal gradients suggest that the temperatures within the Davey Well batholith do not significantly exceed the solidus temperature (~650–700°C) for granitic rocks (Fig. 18a), consistent with evidence for only localized incipient melting and the absence of Mutherbukin-age granites derived from the Durlacher Supersuite. The model also predicts that the base of the sedimentary basin would reach metamorphic temperatures of 550°C after 40 Ma and 620°C after 140 Ma (Fig. 18a). The *P–T* constraints from the staurolite(–garnet)-bearing schists in the Nick Belt and Tommie Well indicate minimum temperatures of 570°C at 5 kbar. Assuming this pressure corresponds to a depth of 14 km, the modelling predicts that at least 80 Ma of radiogenic heating is required to reach these temperatures (Fig. 18a). The peak metamorphic conditions retrieved from the granitic gneiss at deeper crustal levels are estimated above 650°C between 4.4 and 7 kbar, and require similar or longer time scales. Temperature increases most rapidly during the first 20 Ma of heating; after 40 Ma, the thermal gradient begins to stabilize and temperature does not significantly change. These results suggest that the spread of ages ranging from c. 1320 to 1210 Ma observed in the granitic gneiss and across the Mutherbukin Zone may be consistent with a prolonged tectonic event, initiated by crustal thickening at c. 1320 Ma. The upper crustal thickening is modelled as an instantaneous process, and protracted thickening over a series of compressional events could result in longer time scales than those suggested by the modelling, although the absence of multiple transpressional fabrics supports the hypothesis that the thickening might have occurred during a single event. However, the model does not account for removal of sediments by erosion, which would shorten the event duration.

Table 3. Rock parameters used in thermal modelling

Unit	*Th*	*U*	K_2O	*Q*	*k*	*C*
	ppm	*ppm*	*wt%*	*μW m^{-3}*	*W m^{-1} K^{-1}*	*MJ m^{-3} K^{-1}*
Leake Spring Metamorphics[(a)]	24	3.5	4.5	4	2	2.06
Davey Well Granite[(a)]	45	3	5.1	5.5	3	2.1
Glenburgh Terrane[(a)]	8	1.6	2	1.6	3	2.1
MacAdam (lower crust)				0.4	2.77	3
Mantle				0.02	3	4

NOTE: (a) age corrected to 1320 Ma

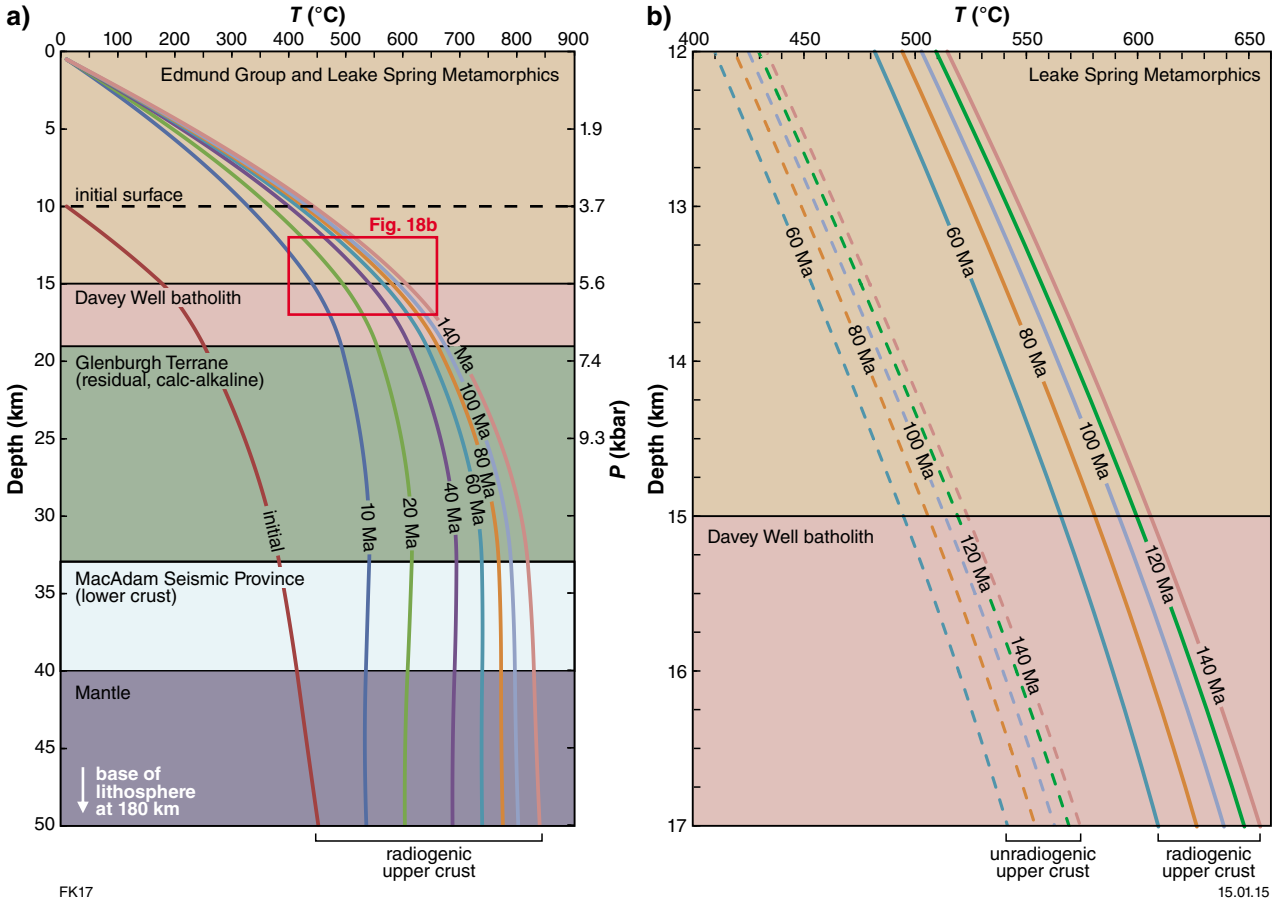

Figure 18. Results of thermal modelling: a) Calculated thermal gradients with time for a layered crustal profile. Model is based on instantaneous thickening of upper crust with an initial thickness of 5 km thickness to a final thickness of 15 km. Composition of upper crust represented by Edmund Group and Leake Spring Metamorphics, which have similar heat production values. Initial surface represented by dashed line. Base of lithosphere is modelled at 180 km, although only upper 50 km shown. Estimated pressure (right side of diagram) assumes density of 2.7 g cm^{-3}. Rock parameters used in the modelling are listed in Table 3; b) comparison between radiogenic and non-radiogenic upper crust. Solid lines based on heat production value of 4.0 µW m^{-3}; from a); dashed lines based on reduced heat production value of 2.3 µW m^{-3}, which is the age-corrected, upper continental crust average from Rudnick and Gao (2003)

Model uncertainties

Although the model is generally consistent with the geologic observations, there are notable sources of uncertainty. The results are very sensitive to the radiogenic heat production values used in the modelling. For example, the composition of the mid-crust in the Mutherbukin Zone is not well known. It is inferred to be the Glenburgh Terrane (Johnson et al., 2011a; 2013b), composed mainly of Archean–Paleoproterozoic granitic gneisses of the Halfway Gneiss (Johnson et al., 2011c, e). In the southern Gascoyne Province near the margin of the Yilgarn Craton, the Glenburgh Terrane also includes metagranitic rocks of the Dalgaringa Supersuite (Sheppard et al., 2004). In addition, the 1820–1775 Ma Moorarie Supersuite makes up a significant proportion of the crust across the Gascoyne Province (Occhipinti and Myers, 1999; Occhipinti and Sheppard, 2001; Martin et al., 2005; Sheppard et al., 2010b), and could also be a major mid-crustal component in the Mutherbukin Zone. The exposed equivalents to these units have a wide variety of lithologies and compositions, ranging from relatively unradiogenic time-corrected compositions (<1 µW m^{-3}) to very radiogenic compositions (>10 µW m^{-3}). Using a more elevated heat production value (≥4 µW m^{-3}) than the one used in Figure 18a (1.6 µW m^{-3}; Table 3) predicts unrealistic crustal thermal gradients. After 80 Ma, temperatures >900°C are predicted at depths below 18 km, and temperatures in excess of the granite liquidus (>1100°C) are achieved at 30 km. These estimates are not consistent with the *P–T* history recorded in the metamorphic rocks or the absence of widespread Mutherbukin-aged magmatism. Furthermore, the Hf–O isotopic compositions of zircons from the main magmatic suites across the Gascoyne Province, including the Moorarie and Durlacher Supersuites, suggest that the Glenburgh Terrane is an important source component for these intrusions (Johnson et al., 2013a). Each magmatic

event would progressively deplete the Glenburgh Terrane source at depth, such that the mid-crust would likely be quite residual during the Mutherbukin Tectonic Event. The value used in the modelling is derived from a representative composition of the Dalgaringa Supersuite, although it should be noted that these arc-related rocks formed exclusively along the southern margin of the Glenburgh Terrane (Sheppard et al., 2004) and do not extend into the Mutherbukin Zone. However, the relatively low heat production calculated from these lithologies is considered to be an appropriate estimate for the composition of the residual mid-crust in the Mutherbukin Zone.

There is also uncertainty in the true thickness of the Davey Well batholith during the Mutherbukin Tectonic Event, since the results of the seismic survey indicate that the batholith has been folded. The volume of granite at depth will have a significant effect on the predicted thermal gradients because the heat production estimated from the Davey Well batholith is the highest value used in the modelling (5.5 μW m^{-3}; Table 3). However, changing the thickness of the granite batholith from 4 to 7 km results in significantly higher thermal gradients than those estimated from the metamorphic rocks, suggesting that a maximum pluton thickness of ~4 km may be an appropriate estimate.

Potential variations in the thickness and composition of the sedimentary basin are additional sources of uncertainty. The basin is assumed to have a thickness of 15 km after the compressional event based on the estimates of peak pressure from the highest grade metasedimentary schists (Fig. 13); although this is a minimum estimate and true thickness of the basin could be slightly higher. There are also inherent uncertainties in the phase equilibria modelling, including uncertainties in the internally consistent dataset and in the *a–x* models used in the modelling, and uncertainties in the actual bulk composition, particularly the H_2O and O content (cf. Powell and Holland, 2008). These uncertainties could have an effect on the estimates of peak metamorphism and, consequently, the predicted time scales of heating based on the thermal modelling. Similarly, the Edmund Group and Leake Spring Metamorphics have a wide range of compositions and heat production values. To assess the effect of high heat producing crust on the predicted thermal gradients, a second simulation was performed using a lower heat production value for the upper crust. The heat production value for the sedimentary basin was reduced from 4.0 to 2.3 μW m^{-3} (Table 3), which is the age-corrected, upper continental crust average from Rudnick and Gao (2003). The predicted thermal gradients using a less radiogenic upper crust are consistently 70–80°C lower than those calculated with the highly radiogenic compositions of the Leake Spring Metamorphics (Fig. 18b). Based on these results, the presence of a highly radiogenic upper crust has a fundamental control on the apparent thermal gradient associated with the Mutherbukin Tectonic Event.

Last, it is difficult to correlate the spread of ages with the absolute timing of the initiation and termination of tectonic events; therefore, there is uncertainty in the event durations. Crustal thickening (D_{1u}) is assumed to have started at c. 1320 Ma, with accessory phase growth driven by fluid flow along active structures. However, it is possible that the D_{1u} transpression event did not start until closer to c. 1280 Ma (Fig. 19) and that the older ages simply record fluid flow along structures without significant thickening. Similarly, there is ambiguity in the precise timing of the event termination. Accessory phase growth at c. 1270 Ma is interpreted to record the waning stages of the D_{1u} event (Fig. 19), but active transpression may have continued later or have been terminated sooner. Nevertheless, the thermal gradients do not significantly change after 40 Ma of heating, suggesting that the absolute uncertainties in the starting age of the event have little effect on the proposed scenario, provided that thickened crust was sustained for ≥40 Ma.

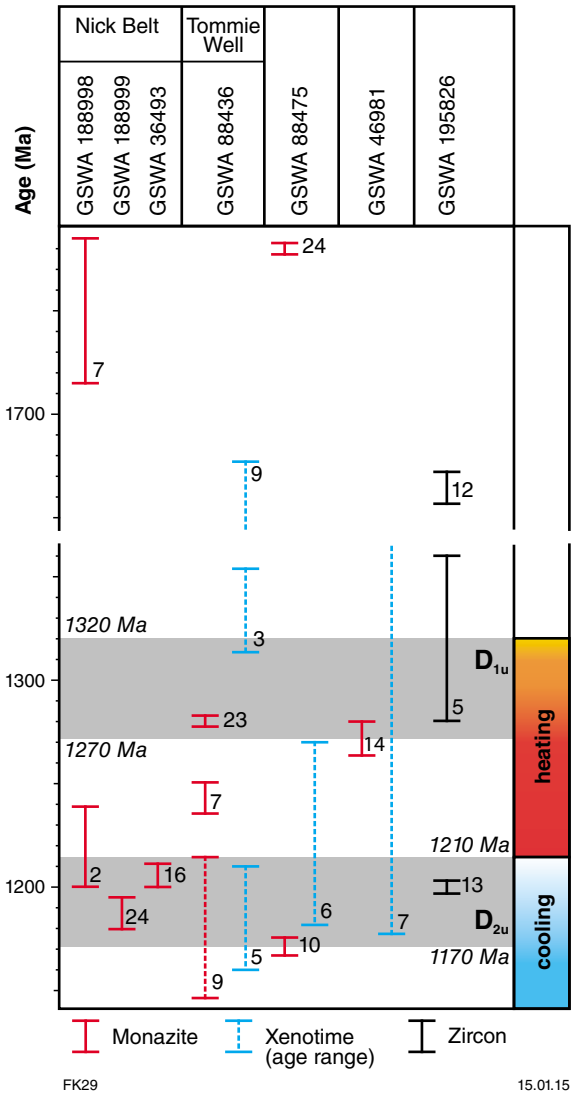

Figure 19. Age summary of dated samples: Crustal thickening during D_{1u} transpression across most of the Mutherbukin Zone was initiated at c. 1320 Ma, with accessory phase growth continuing to c. 1270 Ma. The thermal effects persisted for longer time scales than the deformation event. Peak metamorphism was terminated by D_{2u} extensional deformation at c. 1210 Ma, with subsequent cooling

Crustal evolution and tectonic setting

The model presented here shows that thin-skinned, upper crustal thickening of radiogenic crust, characteristic of the Gascoyne Province, can produce the metamorphic conditions preserved in the Mutherbukin Zone. The spread of ages ranging from c. 1320 to 1210 Ma are consistent with prolonged conductive heating. The ages are interpreted as the initiation of crustal thickening at c. 1320 Ma, with evidence for accessory phase growth during prolonged D_{1u} transpression continuing to c. 1270 Ma. However, the thermal effects would have persisted for longer than the deformation event (Fig. 19), due to conductive heating of thickened radiogenic crust. Peak metamorphism is terminated by D_{2u} extensional deformation at c. 1210 Ma, with subsequent cooling driven by the thinning of radiogenic crust. Zircon ages of c. 1200 Ma in the Davey Well Granite record melt crystallization at near-peak conditions, whereas slightly younger dates retrieved from monazite and xenotime likely record the renewed activity and possible fluid flow during the transition to D_{2u} extension. Evidence from Tommie Well implies that some parts of the crust were subject to a more complicated, polyphase evolution, characterized by cycles of crustal thickening and thinning. This suggests that parts of the crust, particularly those within the Ti Tree Shear Zone, were decoupled from the rocks within the Mutherbukin Zone, possibly recording individual movement episodes on the shear zone itself.

The absence of magmatism during this event distinguishes it from the other tectonothermal events (i.e. 'orogenies') associated with the prolonged reworking of the Capricorn Orogen. The model predicts that metamorphic temperatures would remain below the granitic wet solidus for up to 140 Ma of sustained thickened crust; therefore, significant crustal melts could not be produced from the fertile Davey Well batholith (Fig. 18a) during the time scales involved. Although the middle and lower crustal rocks of the Glenburgh Terrane and the MacAdam Seismic Province are predicted to reach temperatures up to 800°C, these units are the dry, refractory residuals of earlier Paleoproterozoic granite production and would require even higher temperatures to produce significant crustal melts.

The presence of an insulating thermal lid is a fundamental feature of the Mutherbukin Tectonic Event. In this case, a thickened sedimentary basin with elevated concentrations of high heat-producing elements (HPE) would have acted as a thermal lid for at least 100 Ma. The elevated thermal gradient would weaken the lithosphere, allowing the crust to deform horizontally. This weakened lithosphere would also not be able to sustain elevated topography, implying low erosion rates (e.g. McLaren et al., 2005). Another effect of a weak lithosphere is that it will be more responsive to far-field stresses (e.g. Sandiford and McLaren, 2002). Importantly, these far-field stresses could be the tectonic driving force for such intracrustal events. Notably, the timing of the Mutherbukin Tectonic Event was coincident with Stages I (1330–1260 Ma) and II (1225–1140 Ma) of the Albany–Fraser Orogeny, the 1345–1293 Ma Mount West Orogeny, the 1225–1150 Ma Musgrave Orogeny in the west Musgrave Province, and the 1205–1150 Ma Darling Orogeny in the Pinjarra Orogen (Johnson, 2013). The synchronicity of events around the margin of the entire Yilgarn Craton implies that continent-scale tectonics, which may relate to global-scale plate reorganizations during the break-up of the Nuna Supercontinent (Johnson, 2013), may be the cause of tectonism during the Mutherbukin Tectonic Event.

Hydrothermal fluid flow, mineralization and mineral systems

Very low-grade metasedimentary rocks of the 1680–1610 Ma Mount Augustus Sandstone and 1680–1455 Ma Edmund Group also show evidence for deformation and hydrothermal alteration during the Mutherbukin Tectonic Event, although these events are more cryptic than in the Gascoyne Province rocks due to the low to very low grade of metamorphism. More importantly, however, there is evidence for remobilization of pre-existing mineralization at the Abra polymetallic deposit during this event (Rasmussen et al., 2010a; Pirajno et al., 2010; Zi et al., 2015), implying a direct link between medium- to high-grade deformation and metamorphism in the middle crust and hydrothermal fluid flow and mineralization in the upper crust.

Hydrothermal monazite from an undeformed, very coarse sandstone unit toward the base of the Mount Augustus Sandstone (GSWA 156589) on Mount Phillips (Sheppard et al., 2008), yielded a U–Th–Pb SHRIMP monazite date of 1300 ± 10 Ma (Rasmussen, preliminary data). The sample is located close to the regional-scale Edmund Fault (Fig. 2), and the date is interpreted to record a period of hydrothermal fluid flow associated with fault movement. Geological mapping in the eastern part of the Edmund Basin has also shown that regional-scale tight folding and sinistral strike-slip faulting were produced during the Mutherbukin Tectonic Event (Cutten et al., 2011). Direct $^{40}K/^{40}Ar$ age constraints on synkinematic fault gouge illite from two of these faults yielded dates of 1171 ± 25 Ma (GSWA 189218; Wingate et al., 2012) and 1157 ± 23 Ma (GSWA 189264, Zwingmann, preliminary data).

The Abra polymetallic deposit, in the eastern part of the Edmund Basin (Figs 1 and 2), is a blind, hydrothermal deposit hosting Fe–Mn–Pb–Zn–Ba–Cu(–Au–Ag–Bi–W). The deposit is characterized by a funnel shaped brecciated zone, interpreted as a stockwork breccia feeder pipe, overlain by stratabound mineralization, including Fe-carbonate–quartz–barite–pyrite–magnetite–chalcopyrite, with abundant fluidized or jigsaw textures (Pirajno et al., 2010). These assemblages cut through a wider alteration envelope of chlorite–siderite (Pirajno et al., 2010). The deposit is located adjacent to the Quartzite Well Fault which is an extension of the crustal-scale Lyons River Fault, the main suture zone between the Pilbara Craton and the Glenburgh Terrane (Johnson et al., 2013b). Authigenic monazite from three altered sandstone samples of the Kiangi Creek Formation (GSWA 149085, 149086, and 149093) within the ore zone yield a weighted mean $^{207}Pb^*/^{206}Pb^*$ date of 1385 ± 20 Ma (Rasmussen et al., 2010a; Zi et al., 2015), interpreted

to represent a hydrothermal event postdating the main phase of mineralization at c. 1594 Ma (Zi et al., 2015). Monazites in samples distal to mineralization yield weighted mean $^{207}Pb^*/^{206}Pb^*$ dates of 1221 ± 14 Ma and 995 ± 18 Ma, interpreted as the timing of discrete episodes of hydrothermal fluid flow (Zi et al., 2015). Additionally, pyrite from the deposit yielded a $^{187}Re/^{188}Os$ date of 1284 ± 47 Ma (Pirajno et al., 2010). Xenotime crystals extracted from the nearby Tangadee Rhyolite yielded a SHRIMP U–Th–Pb date of 1235 ± 19 Ma (Rasmussen et al., 2010a), interpreted either as the date of extrusion of the rhyolite or the timing of subsequent hydrothermal alteration.

A deep crustal seismic reflection survey through the Capricorn Orogen identified the major suture zones associated with the amalgamation of the West Australian Craton, as well as a series of other major crustal structures which extend through the crust to the mantle (Fig. 2; Johnson et al., 2013b). In most cases, known sites of mineralization in the orogen lie along, close to, or within fault splays related to these major structures, highlighting the importance of these major faults as deep plumbing systems that allow the transport of fluid direct from the mantle, or mid- to lower crust (enriched source rocks), into the upper crust (Wyborn et al., 1994; Aitken et al., 2013; Johnson et al., 2013b; McCuaig and Hronsky, 2014). However, since the ages of these mineral deposits are not precisely known, the source of mineralizing fluids and driving force (energy) for mineral systems within the orogen are not fully understood. A better understanding of the dynamic interplay between metamorphism, deformation, fluid flow and mineralization would greatly increase the mineral prospectivity of the region (Aitken et al., 2013).

The ages obtained from the upper crustal metasedimentary basins demonstrates that faulting, folding and accompanying hydrothermal fluid flow were broadly synchronous with tectonic activity in the underlying Gascoyne Province basement (Fig. 20). Monazite from the Mount Augustus Sandstone indicates hydrothermal fluid flow associated with fault movement at c. 1300 Ma (Rasmussen, preliminary data), whereas the phosphate age data from the Abra deposit show three peaks of hydrothermal activity in the upper crust at c. 1385 Ma, 1220 Ma and 995 Ma (Rasmussen et al., 2010a; Zi et al., 2015). The oldest episode at c. 1385 Ma, recorded by hydrothermal monazite at Abra, precedes any recorded deformation or metamorphism in the Gascoyne Province by ~55 Ma (Fig. 19), and the driver for fluid flow is currently unknown. However, it is possible that localized upper crustal fluid flow and hydrothermal alteration may be related to discrete movements on the Quartzite Well–Lyons River Fault system, which had little to no effect on the basement rocks outside of the fault zone. The two younger events at c. 1300 and 1220 Ma correlate precisely with the onset of crustal thickening (D_{1u}), and peak metamorphism and extension (D_{2u}), respectively, in the underlying basement rocks (Figs 19 and 20). Furthermore, the termination of upper crustal hydrothermal/tectonic activity at c. 1170 Ma is also coincident with crustal thinning and cooling of the Gascoyne Province crust. Hydrothermal fluid flow is also coincident with medium-grade metamorphism and deformation during the younger 1030–955 Ma Edmundian Orogeny (Fig. 20; Sheppard et al., 2007).

These results demonstrate that low-temperature hydrothermal fluid flow in the upper crust of the orogen was driven, at least in part, by medium- to high-grade metamorphic and deformation events in the mid-crust. Although the origin of the hydrothermal fluids is currently unknown (i.e. metamorphic versus meteoric), the spatial association of hydrothermal activity and mineralization with crustal-scale faults implies that mass transfer of energy and fluid was focused through the crust during tectonism into discrete pre-existing upper crustal fault zones. These observations are critical and key features of the mineral systems concept (McCuaig and Hronsky, 2014). Further investigations into the composition and temperature of the hydrothermal fluid (i.e. from fluid inclusion studies) may help to constrain the origin of the fluid or the role of metamorphic heat transfer to fluids in the upper crust. Despite the transfer of energy and fluid being key components of the mineral systems approach to prospectivity analyses (Wyborn et al., 1994; McCuaig and Hronsky, 2014), few studies have attempted to include such data into prospectivity analyses. The data presented here demonstrate that understanding the timing and spatial distribution of metamorphic and deformation events and their reactivation effects on pre-existing fault systems in the upper crust are critical for constraining where and when mineral deposits might form.

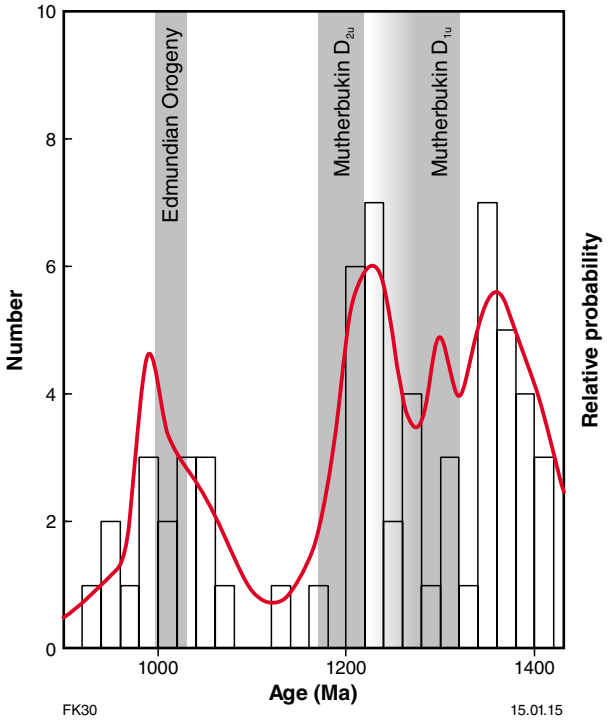

Figure 20. Relatively probability plot of phosphate data from the Mutherbukin Zone (this study), the Abra polymetallic deposit (Rasmussen et al., 2010a; Zi et al., 2015), and the Mount Augustus Sandstone (Rasmussen, preliminary data). Histogram bin size = 20 Ma

Conclusions

The 1320–1170 Ma Mutherbukin Tectonic Event represents a period of protracted intraplate deformation and metamorphism that affected rocks of the Gascoyne Province and overlying metasedimentary packages. Although the effects of the event are recorded throughout the Gascoyne Province, deformation and metamorphism were focused mainly within the Mutherbukin Zone which preserves a crustal profile, increasing in depth from north to south, away from the Ti Tree Shear Zone.

P–T analyses combined with in situ phosphate geochronology indicate that the prograde history across the Mutherbukin Zone was dominated by thin-skinned upper crustal thickening. This event (D_{1u}) was initiated at c. 1320 Ma, although geochronological evidence indicates the continued growth of accessory phases to c. 1270 Ma. The thermal effects of this event persisted for up to 100 Ma, culminating in peak metamorphism along an apparent thermal gradient of 45°C km^{-1} through the mid-crust. Peak metamorphism was terminated by crustal thinning during transtension (D_{2u}) at c. 1210 Ma, with evidence for protracted accessory phase growth between c. 1210 and 1170 Ma during cooling and continued deformation. Thermal modelling confirms that thin-skinned, upper crustal thickening of radiogenic crust typical of the Gascoyne Province forms a 'thermal lid' and can reproduce these metamorphic conditions over the appropriate time scales.

Although the evolution of the Mutherbukin Tectonic Event is most consistent with this model, not all parts of the Mutherbukin Zone record this relatively simple, prolonged history. Samples from a narrow fault-bound lens within the Ti Tree Shear Zone ('Tommie Well' locality) preserve a polyphase evolution, characterized by punctuated cycles of crustal thickening and thinning, implying that parts of the crust were decoupled during the Mutherbukin Tectonic Event.

The upper crustal metasedimentary rocks across the region also record evidence for faulting and hydrothermal fluid flow during this event, although this history is more cryptic due to the low to very low grade of metamorphism. The timing of upper crustal fluid flow and hydrothermal alteration was synchronous with deformation and metamorphic events in the underlying Gascoyne Province basement, indicating a strong, dynamic link between the mid and upper crust. These relationships are critical for understanding mineral systems and for constraining where and when mineral deposits might form.

References

Aitken, ARA, Joly, A, Johnson, SP, Dentith, M, Thorne, AM and Tyler, IM 2013, 3D architecture and mineral prospectivity of the Gascoyne Province, *in* GSWA 2013 extended abstracts: promoting the prospectivity of Western Australia: Geological Survey of Western Australia, Record 2013/2, p. 35–38.

Armstrong, JT 1988, Quantitative analysis of silicate and oxide minerals: comparison of Monte Carlo, ZAF and phi-rho-z procedures: Microbeam analysis, v. 23, p. 239–246.

Carlson, WD 2011, Porphyroblast crystallization: linking processes, kinetics, and microstructures: International Geology Review, v. 53, no. 3–4, p. 406–445.

Cawood, PA and Tyler, IM 2004, Assembling and reactivating the Proterozoic Capricorn Orogen: lithotectonic elements, orogenies, and significance: Precambrian Research, v. 128, p. 201–218.

Clauser, C 2003, Numerical simulation of reactive flow in hot aquifers: SHEMAT and processing SHEMAT: Springer, 332p.

Cutten, HN, Thorne, AM and Johnson, SP 2011, Geology of the Edmund and Collier Groups, *in* Capricorn Orogen seismic and magnetotelluric (MT) workshop 2011: extended abstracts *edited by* SP Johnson, AM Thorne and IM Tyler: Geological Survey of Western Australia, Record 2011/25, p. 41–48.

Dentith, MC, Johnson, SP, Evans, S, Aitken, ARA, Joly, A, Thiel, S and Tyler, IM 2014, A magnetotelluric traverse across the eastern part of the Capricorn Orogen: Geological Survey of Western Australia, Report 135, 54p.

Diener, JFA and Powell, R 2010, Influence of ferric iron on the stability of mineral assemblages: Journal of Metamorphic Geology, v. 28, no. 6, p. 599–613.

Diener, JFA, White, RW and Powell, R 2008, Granulite facies metamorphism and subsolidus fluid-absent reworking, Strangways Range, Arunta Block, central Australia: Journal of Metamorphic Geology, v. 26, no. 6, p. 603–622.

Holland, TJB and Powell, R 1998, An internally consistent thermodynamic data set for phases of petrological interest: Journal of Metamorphic Geology, v. 16, no. 3, p. 309–343.

Holland, TJB and Powell, R 2011, An improved and extended internally consistent thermodynamic dataset for phases of petrological interest, involving a new equation of state for solids: Journal of Metamorphic Geology, v. 29, no. 3, p. 333–383.

Janots, E and Rubatto, D 2014, U–Th–Pb dating of collision in the external Alpine domains (Urseren zone, Switzerland) using low temperature allanite and monazite: Lithos, v.184–187, p. 155–166.

Johnson, SP 2013, The birth of supercontinents and the Proterozoic assembly of Western Australia: Geological Survey of Western Australia, 78p.

Johnson, SP, Korhonen, FJ, Kirkland, CL, Cliff, JB, Belousova, EA, Sheppard, S, Murphy, R and Wingate, MTD 2013a, The application of oxygen isotopes of zircon in regional mapping: an example from Paleoproterozoic granites in the Gascoyne Province, *in* GSWA 2013 extended abstracts: promoting the prospectivity of Western Australia: Geological Survey of Western Australia, Record 2013/2, p. 27–30.

Johnson, SP, Thorne, AM and Tyler, IM (editors) 2011a, Capricorn Orogen seismic and magnetotelluric (MT) workshop 2011: extended abstracts: Geological Survey of Western Australia, Record 2011/25, 120p.

Johnson, SP, Sheppard, S, Krapf, CBE and Hocking, RM 2011b, Lockier, WA Sheet 2048: Geological Survey of Western Australia, 1:100 000 Geological Series.

Johnson, SP, Sheppard, S, Rasmussen, B, Wingate, MTD, Kirkland, CL, Muhling, JR, Fletcher, IR and Belousova, E 2010, The Glenburgh Orogeny as a record of Paleoproterozoic continent–continent collision: Geological Survey of Western Australia, Record 2010/5, 54p.

Johnson, SP, Sheppard, S, Rasmussen, B, Wingate, MTD, Kirkland, CL, Muhling, JR, Fletcher, IR and Belousova, EA 2011c, Two collisions, two sutures: punctuated pre-1950 Ma assembly of the West Australian Craton during the Ophthalmian and Glenburgh Orogenies: Precambrian Research, v. 189, no. 3–4, p. 239–262, doi: 10.1016/j.precamres.2011.07.011.

Johnson, SP, Sheppard, S, Thorne, AM, Rasmussen, B, Fletcher, IR, Wingate, MTD and Cutten, HN 2011d, The role of the 1280–1250 Ma Mutherbukin Tectonic Event in shaping the crustal architecture and mineralization history of the Capricorn Orogen, *in* GSWA 2011 extended abstracts: promoting the prospectivity of Western Australia: Geological Survey of Western Australia, Record 2011/2, p. 1–3.

Johnson, SP, Sheppard, S, Wingate, MTD, Kirkland, CL and Belousova, EA 2011e, Temporal and hafnium isotopic evolution of the Glenburgh Terrane basement: an exotic crustal fragment in the Capricorn Orogen: Geological Survey of Western Australia, Report 110, 27p.

Johnson, SP, Thorne, AM, Tyler, IM, Korsch, RJ, Kennett, BLN, Cutten, HN, Goodwin, J, Blay, OA, Blewett, RS, Joly, A, Dentith, MC, Aitken, ARA, Holzschuh, J, Salmon, M, Reading, A, Heinson, G, Boren, G, Ross, J, Costelloe, RD and Fomin, T 2013b, Crustal architecture of the Capricorn Orogen, Western Australia and associated metallogeny: Australian Journal of Earth Sciences, v. 60, no. 6–7, p. 681–705, doi:10.1080/08120099.2013.826735.

Korhonen, FJ, Powell, R and Stout, JH 2012, Stability of sapphirine + quartz in the oxidized rocks of the Wilson Lake terrane, Labrador: calculated equilibria in NCKFMASHTO: Journal of Metamorphic Geology, v. 30, no. 1, p. 21–36.

Korsch, RJ, Johnson, SP, Tyler, IM, Thorne, AM, Blewett, RS, Cutten, HN, Joly, A, Dentith, MC, Aitken, ARA, Goodwin, JA and Kennett, BLN 2011, Geodynamic implications of the Capricorn deep seismic survey: from the Pilbara Craton to the Yilgarn Craton, *in* Capricorn Orogen seismic and magnetotelluric (MT) workshop 2011: extended abstracts *edited by* SP Johnson, AM Thorne and IM Tyler: Geological Survey of Western Australia, Record 2011/25, p. 107–114.

Mahar, EM, Baker, JM, Powell, R, Holland, TJB and Howell , N 1997, The effect of Mn on mineral stability in metapelites: Journal of Metamorphic Geology, v. 15, no. 2, p. 223–238.

Martin, DM and Thorne, AM 2004, Tectonic setting and basin evolution of the Bangemall Supergroup in the northwestern Capricorn Orogen: Precambrian Research, v. 128, p. 385–409.

Martin, DM, Sheppard, S and Thorne, AM 2005, Geology of the Maroonah, Ullawarra, Capricorn, Mangaroon, Edmund, and Elliott Creek 1:100 000 sheets: Geological Survey of Western Australia, 1:100 000 Geological Series Explanatory Notes, 65p.

McCuaig, TC and Hronsky, JMA 2014, The mineral system concept: Society of Economic Geologists Special Publication 18, p. 153–175.

McLaren, S, Sandiford, M, Hand, M, Neumann, N, Wyborn, L and Bastrakova, I 2003, The hot southern continent: heat flow and heat production in Australian Proterozoic terranes: Geological Society of America Special Papers, v. 372, p. 157–167.

McLaren, S, Sandiford, M and Powell, R 2005, Contrasting styles of Proterozoic crustal evolution: a hot-plate tectonic model for Australian terranes: Geology, v. 33, p. 673–676.

McNaughton, NJ, Rasmussen, B and Fletcher, IR 1999, SHRIMP uranium-lead dating of diagenetic xenotime in sliciclastic sedimentary rocks: Science, v. 285, p. 78–80.

Morgan, P 1984, The thermal structure and thermal evolution of the continental lithosphere: Physics and Chemistry of the Earth, v. 15, p. 107–193.

Myers, JS, Shaw, RD and Tyler, IM 1996, Tectonic evolution of Proterozoic Australia: Tectonics, v. 15, p. 1431–1146.

Occhipinti, SA and Myers, JS 1999, Geology of the Moorarie 1:100 000 sheet: Geological Survey of Western Australia, 1:100 000 Geological Series Explanatory Notes, 20p.

Occhipinti, SA and Sheppard, S 2001, Geology of the Glenburgh 1:100 000 sheet: Geological Survey of Western Australia, 1:100 000 Geological Series Explanatory Notes, 37p.

Occhipinti, SA, Sheppard, S, Passchier, C, Tyler, IM and Nelson, DR 2004, Palaeoproterozoic crustal accretion and collision in the southern Capricorn Orogen: the Glenburgh Orogeny: Precambrian Research, v. 128, p. 237–255.

Overstreet, WC 1967, The geological occurrence of monazite: US Geological Survey Professional Paper 530, 327p.

Pirajno, F, Thorne, AM, Mernagh, TP, Creaser, RA, Hell, A and Cutten, H 2010, The Abra deposit: a polymetallic mineral system in the Edmund Basin, Capricorn Orogen, Western Australia, *in* 13th Quadrennial IAGOD Symposium Proceedings *edited by* NJ Cook and Others : International Association on Genesis of Ore Deposits (IAGOD); Giant Ore Deposits Down-Under, Adelaide, South Australia, 6 April 2010, p. 112–114.

Powell, R and Holland, TJB 1988, An internally consistent dataset with uncertainties and correlations: 3. Applications to geobarometry, worked examples and a computer program: Journal of Metamorphic Geology, v. 6, no. 2, p. 173–204.

Powell, R and Holland, TJB 2008, On thermobarometry: Journal of Metamorphic Geology, v. 26, no. 2, p. 155–179.

Rasmussen, B, Fletcher, IR and Muhling, JR 2007, U–Pb dating and element mapping of three generations of monazite: Unravelling cryptic tectonothermal events in low-grade terranes: Geochimica et Cosmochimica Acta, v. 71, p. 670–690.

Rasmussen, B, Fletcher, IR and Muhling, JR 2011, Response of xenotime to prograde metamorphism: Contributions to Mineralogy and Petrology, v. 162, p. 1259–1277.

Rasmussen, B, Fletcher, IR, Muhling, JR, Thorne, AM, Cutten, HN, Pirajno, F and Hell, A 2010a, In situ U–Pb monazite and xenotime geochronology of the Abra polymetallic deposit and associated sedimentary and volcanic rocks, Bangemall Supergroup, Western Australia: Geological Survey of Western Australia, Record 2010/12, 31p.

Rasmussen, B, Fletcher, IR, Muhling, JR and Wilde, SA 2010b, In situ U–Th–Pb geochronology of monazite and xenotime from the Jack Hills belt: implications for the age of deposition and metamorphism of Hadean zircons: Precambrian Research, v. 180, no. 1–2, p. 26–46.

Rasmussen, B and Muhling, JR 2007, Monazite begets monazite: evidence for dissolution of detrital monazite and reprecipitation of syntectonic monazite during low-grade regional metamorphism: Contributions to Mineralogy and Petrology, v. 54, no. 6, p. 675–689.

Rudnick, RL and Gao, S 2003, Composition of the continental crust: Treatise of Geochemistry, v. 3, p. 1–64.

Sandiford, M and McLaren, S 2002, Tectonic feedback and the ordering of heat producing elements within the continental lithosphere: Earth and Planetary Science Letters, v. 204, no. 1–2, p. 133–150.

Schumacher, JC 1991, Empirical ferric iron corrections: necessity, assumptions, and effects on selected geothermobarometers: Mineralogical Magazine, v. 55, no. 378, p. 3–18.

Sheppard, S, Bodorkos, S, Johnson, SP, Wingate, MTD and Kirkland, CL 2010a, The Paleoproterozoic Capricorn Orogeny: intracontinental reworking not continent–continent collision: Geological Survey of Western Australia, Report 108, 33p.

Sheppard, S, Farrell, TR, Martin, DM, Thorne, AM and Bagas, L 2008, Mount Phillips, WA Sheet 2149 (2nd edition): Geological Survey of Western Australia, 1:100 000 Geological Series.

Sheppard, S, Johnson, SP, Wingate, MTD, Kirkland, CL and Pirajno, F 2010b, Explanatory notes for the Gascoyne Province: Geological Survey of Western Australia, 336p.

Sheppard, S, Occhipinti, SA and Nelson, DR 2005, Intracontinental reworking in the Capricorn Orogen, Western Australia: the 1680–1620 Ma Mangaroon Orogeny: Australian Journal of Earth Sciences, v. 52, p. 443–460.

Sheppard, S, Occhipinti, SA and Tyler, IM 2004, A 2005–1970 Ma Andean-type batholith in the southern Gascoyne Complex, Western Australia: Precambrian Research, v. 128 (Assembling the Palaeoproterozoic Capricorn Orogen), p. 257–277.

Sheppard, S, Rasmussen, B, Muhling, JR, Farrell, TR and Fletcher, IR 2007, Grenvillian-aged orogenesis in the Palaeoproterozoic Gascoyne Complex, Western Australia: 1030–950 Ma reworking of the Proterozoic Capricorn Orogen: Journal of Metamorphic Geology, v. 25, p. 477–494.

Spear, FS and Selverstone, J 1983, Quantitative PT paths from zoned minerals: theory and tectonic applications: Contributions to Mineralogy and Petrology, v. 83, no. 3–4, p. 348–357.

St-Onge, MR 1987, Zoned poikiloblastic garnets: PT paths and syn-metamorphic uplift through 30 km of structural depth, Wopmay Orogen, Canada: Journal of Petrology, v. 28, p. 1–21.

Tinkham, DK, Zuluaga, CA and Stowell, HH 2001, Metapelitic phase equilibria modelling in MnNCKFMASH: the effect of variable Al_2O_3 and MgO/(MgO + FeO) on mineral stability: Geological Materials Research, v. 3, p. 1–42.

Tyler, IM and Thorne, AM 1990, The northern margin of the Capricorn Orogen, Western Australia — an example of an early Proterozoic collision zone: Journal of Structural Geology, v. 12, p. 685–701.

White, RW, Powell, R and Halpin, JA 2004, Spatially-focussed melt formation in aluminous metapelites from Broken Hill, Australia: Journal of Metamorphic Geology, v. 22, no. 9, p. 825–845.

White, RW, Powell, R and Holland, TJB 2001, Calculation of partial melting equilibria in the system Na_2O-CaO-K_2O-FeO-MgO-Al_2O_3–SiO_2–H_2O (NCKFMASH): Journal of Metamorphic Geology, v. 19, no. 2, p. 139–153.

White, RW, Powell, R and Holland, TJB 2007, Progress relating to calculation of partial melting equilibria for metapelites: Journal of Metamorphic Geology, v. 25, no. 5, p. 511–527.

White, RW, Powell, R, Holland, TJB, Johnson, TE and Green, ECR 2014a, New mineral activity–composition relations for thermodynamic calculations in metapelitic systems: Journal of Metamorphic Geology, v. 32, no. 3, p. 261–286.

White, RW, Powell, R and Johnson, TE 2014b, The effect of Mn on mineral stability in metapelites revisited: new *a–x* relations for manganese-bearing minerals: Journal of Metamorphic Geology, doi:10.1111/jmg.12095.

White, RW, Stevens, G and Johnson, W 2011, Is the crucible reproducible? Reconciling melting experiments with thermodynamic calculations: Elements, v. 7, no. 4, p. 241–246.

Williams, SJ 1985, Geology of the Gascoyne Province (1:1 000 000 scale) in Geology of the Gascoyne Province, Western Australia by SJ Williams: Geological Survey of Western Australia, Report 15, Plate 1.

Williams, SJ 1986, Geology of the Gascoyne Province, Western Australia: Geological Survey of Western Australia, Report 15, 85p.

Wing, BA, Ferry, JM and Harrison, TM 2003, Prograde destruction and formation of monazite and allanite during contact and regional metamorphism of pelites: petrology and geochronology: Contributions to Mineralogy and Petrology, v. 145, p. 228–250.

Wingate, MTD, Cutten, HN, Zwingmann, H, Todd, AJ and Kirkland, CL 2012, 189218: siltstone fault-rock, Brumby Creek; Geochronology Record 1117: Geological Survey of Western Australia, 3p.

Wingate, MTD, Kirkland, CL, Bodorkos, S, Sheppard, S and Farrell, TR 2009, 183215: porphyritic metamonzogranite, Davey Well; Geochronology Record 771: Geological Survey of Western Australia, 4p.

Wingate, MTD, Kirkland, CL and Johnson, SP 2013, 195826: monzogranitic gneiss, McCarthy Well; Geochronology Record 1104: Geological Survey of Western Australia, 5p.

Wingate, MTD, Kirkland, CL, Johnson, SP and Sheppard, S 2010, 185944: porphyritic metamonzogranite, Mombo Creek; Geochronology Record 900: Geological Survey of Western Australia, 4p.

Wingate, MTD and Kirkland, CL 2013, Introduction to geochronology information released in 2013: Geological Survey of Western Australia, 5p.

Wyborn, LAI, Heinrich, CA and Jaques, AL 1994, Australian Proterozoic mineral systems: essential ingredients and mappable criteria, *in* Australian mining looks north — the challenges and choices *edited by* PC Hallenstein: Australian Institute of Mining and Metallurgy; 1994 AusIMM Annual Conference, Darwin, Northern Territory, 5 August 1994, p. 109–115.

Zi, J-W, Rasmussen, B, Muhling, JR, Fletcher, IR, Dunkley, DJ, Johnson, SP, Thorne, AM, Cutten, HN, and Korhonen, FJ 2015, In situ U–Pb geochronology of xenotime and monazite from the Abra polymetallic deposit in the Capricorn Orogen, Australia: Dating hydrothermal mineralization and fluid flow in a long-lived crustal structure: Precambrian Research, v. 260, p. 91–112.

Appendix 1

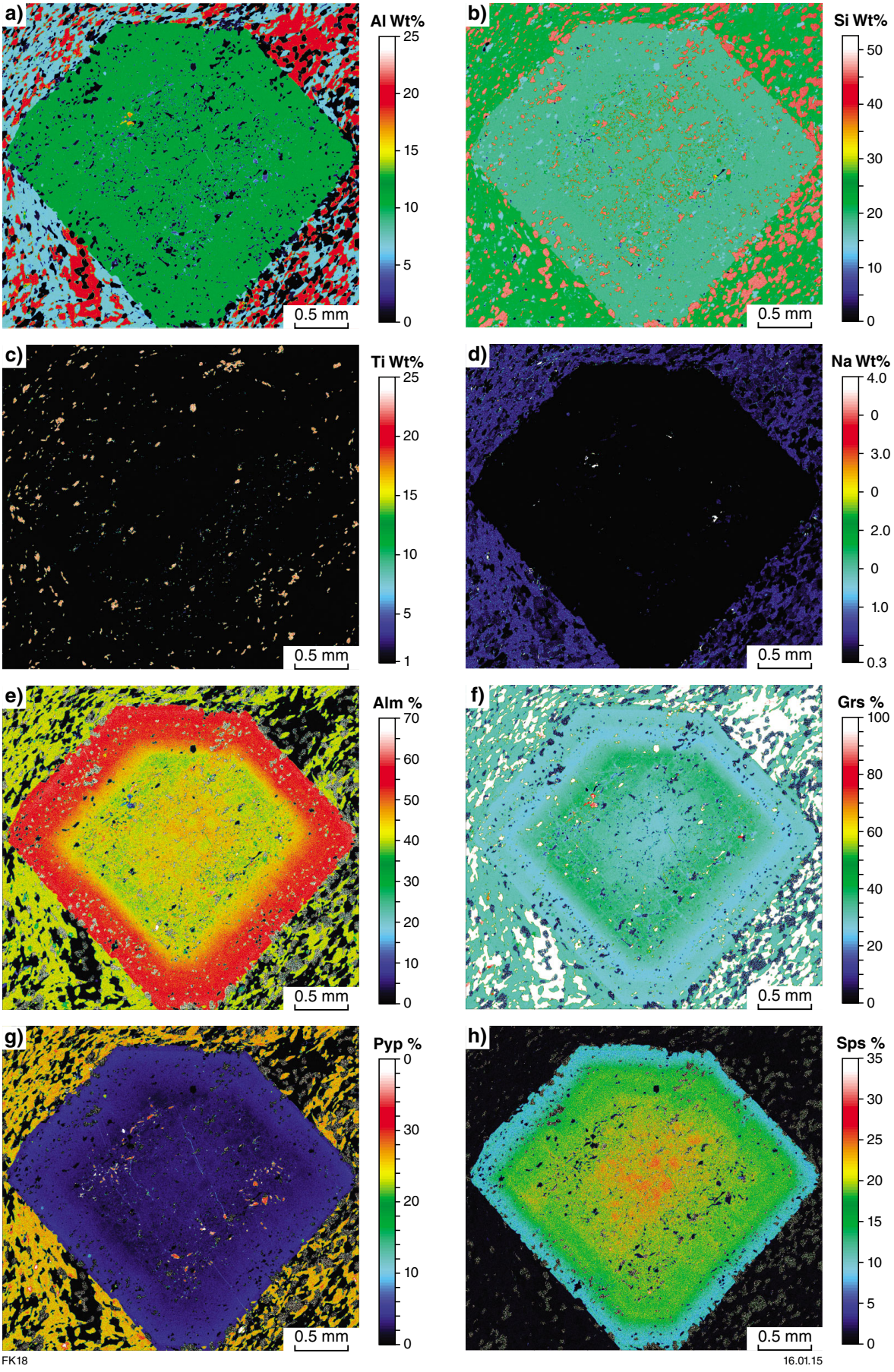
a)
Al Wt%
25
20
15
10
5
0
0.5 mm
b)
Si Wt%
50
40
30
20
10
0
0.5 mm
c)
Ti Wt%
25
20
15
10
5
1
0.5 mm
d)
Na Wt%
4.0
0
3.0
0
2.0
0
1.0
0.3
0.5 mm
e)
Alm %
70
60
50
40
30
20
10
0
0.5 mm
f)
Grs %
100
80
60
40
20
0
0.5 mm
g)
Pyp %
0
30
20
10
0
0.5 mm
h)
Sps %
35
30
25
20
15
10
5
0
0.5 mm
FK18
16.01.15

Table 1.1. Representative garnet analyses

Sample	*208362*																	
Grain	*g2*									*g3*								
SiO_2	37.28	36.48	37.06	36.16	36.92	36.70	37.03	36.73	36.83	37.02	37.13	36.26	36.04	36.81	36.26	36.25	36.13	36.48
TiO_2	0.00	0.00	0.12	0.14	0.16	0.25	0.11	0.11	0.00	0.00	0.00	0.00	0.00	0.00	0.19	0.19	0.07	0.00
Al_2O_3	20.92	21.37	21.03	21.58	20.55	21.15	20.84	21.10	21.25	21.29	21.27	21.70	21.95	21.24	21.13	21.43	21.78	21.69
Cr_2O_3	0.00	0.06	0.00	0.00	0.00	0.00	0.00	0.00	0.00	0.06	0.00	0.04	0.00	0.00	0.00	0.00	0.00	0.00
FeO	24.29	21.20	19.58	18.49	20.56	19.81	20.54	23.66	24.21	24.89	24.86	24.72	22.03	19.90	19.04	18.80	21.54	25.57
MnO	4.99	9.69	10.01	11.86	10.54	10.27	9.45	8.10	7.01	4.95	4.83	6.72	7.78	9.51	11.69	10.50	7.98	4.83
MgO	0.83	0.78	0.68	0.64	0.77	0.71	0.72	0.87	0.93	0.92	0.95	0.88	0.70	0.75	0.69	0.62	0.74	0.99
CaO	11.65	10.15	11.56	10.83	9.71	10.68	10.53	9.23	9.70	10.88	10.83	10.14	11.28	11.69	10.32	12.02	11.18	10.40
Na_2O	0.00	0.00	0.00	0.00	0.00	0.00	0.00	0.00	0.00	0.00	0.00	0.00	0.00	0.00	0.00	0.00	0.00	0.00
Total	99.97	99.72	100.03	99.68	99.22	99.58	99.22	99.80	99.93	100.02	99.87	100.47	99.78	99.90	99.32	99.81	99.42	99.97
Number of cations based on 12 O																		
Si	2.98	2.93	2.96	2.90	2.99	2.95	2.99	2.95	2.95	2.96	2.97	2.89	2.88	2.94	2.92	2.90	2.90	2.91
Ti	0.00	0.00	0.01	0.01	0.01	0.02	0.01	0.01	0.00	0.00	0.00	0.00	0.00	0.00	0.01	0.01	0.00	0.00
Al	1.97	2.02	1.98	2.04	1.96	2.00	1.98	2.00	2.01	2.00	2.00	2.04	2.07	2.00	2.01	2.02	2.06	2.04
Cr	0.00	0.00	0.00	0.00	0.00	0.00	0.00	0.00	0.00	0.00	0.00	0.00	0.00	0.00	0.00	0.00	0.00	0.00
Fe^{2+}	1.54	1.30	1.22	1.10	1.34	1.26	1.35	1.51	1.53	1.58	1.60	1.46	1.30	1.21	1.16	1.10	1.31	1.58
Fe^{3+}	0.08	0.12	0.09	0.14	0.05	0.07	0.04	0.08	0.09	0.08	0.06	0.18	0.17	0.12	0.12	0.16	0.13	0.13
Mn	0.34	0.66	0.68	0.81	0.72	0.70	0.65	0.55	0.48	0.33	0.33	0.45	0.53	0.64	0.80	0.71	0.54	0.33
Mg	0.10	0.09	0.08	0.08	0.09	0.08	0.09	0.10	0.11	0.11	0.11	0.10	0.08	0.09	0.08	0.07	0.09	0.12
Ca	1.00	0.87	0.99	0.93	0.84	0.92	0.91	0.80	0.83	0.93	0.93	0.87	0.97	1.00	0.89	1.03	0.96	0.89
Na	0.00	0.00	0.00	0.00	0.00	0.00	0.00	0.00	0.00	0.00	0.00	0.00	0.00	0.00	0.00	0.00	0.00	0.00
Total	8	8	8	8	8	8	8	8	8	8	8	8	8	8	8	8	8	8
X_{Alm}	0.52	0.45	0.41	0.38	0.45	0.43	0.45	0.51	0.52	0.53	0.54	0.51	0.45	0.41	0.40	0.38	0.45	0.54
X_{Pyp}	0.03	0.03	0.03	0.03	0.03	0.03	0.03	0.04	0.04	0.04	0.04	0.04	0.03	0.03	0.03	0.03	0.03	0.04
X_{Grs}	0.33	0.30	0.33	0.32	0.28	0.31	0.30	0.27	0.28	0.31	0.31	0.30	0.34	0.34	0.30	0.35	0.33	0.31
X_{Sps}	0.11	0.22	0.23	0.28	0.24	0.24	0.22	0.19	0.16	0.11	0.11	0.16	0.18	0.22	0.27	0.24	0.19	0.11

NOTE: Fe^{3+} contents determined using stoichiometric method of Schumacher (1991)

Table 1.1. continued

Sample	*208364*									*195852*	
Grain			*g2*				*g3*			*g1–6*	*g1–10*
SiO_2	36.95	36.03	35.06	35.71	35.39	36.62	35.11	35.90	36.02	35.16	36.54
TiO_2	0.00	0.00	0.00	0.00	0.00	0.00	0.00	0.00	0.00	0.00	0.12
Al_2O_3	20.89	21.33	21.72	21.71	21.78	21.13	21.69	21.16	21.29	21.70	20.73
Cr_2O_3	0.00	0.00	0.00	0.06	0.00	0.00	0.00	0.00	0.07	0.00	0.00
FeO	32.55	30.66	29.87	30.95	34.58	34.25	30.73	29.46	32.98	31.51	28.77
MnO	5.33	8.48	10.64	8.16	3.76	3.59	8.38	10.82	5.79	7.77	10.51
MgO	1.96	1.54	1.40	1.59	2.41	2.38	1.53	1.36	1.97	2.03	1.71
CaO	2.29	2.23	1.61	2.39	2.11	2.23	2.38	1.71	2.28	1.94	1.86
Na_2O	0.00	0.00	0.00	0.00	0.00	0.03	0.00	0.02	0.00	0.02	0.00
Total	99.96	100.27	100.31	100.57	100.05	100.24	99.82	100.43	100.41	100.13	100.25
Number of cations based on 12 O											
Si	3.00	2.92	2.85	2.88	2.86	2.95	2.86	2.91	2.91	2.85	2.97
Ti	0.00	0.00	0.00	0.00	0.00	0.00	0.00	0.00	0.00	0.00	0.01
Al	2.00	2.04	2.08	2.07	2.07	2.01	2.08	2.02	2.03	2.07	1.98
Cr	0.00	0.00	0.00	0.00	0.00	0.00	0.00	0.00	0.00	0.00	0.00
Fe^{2+}	2.19	1.96	1.81	1.93	2.13	2.23	1.89	1.86	2.08	1.90	1.88
Fe^{3+}	0.01	0.12	0.22	0.16	0.21	0.08	0.21	0.15	0.15	0.23	0.07
Mn	0.37	0.58	0.73	0.56	0.26	0.25	0.58	0.74	0.40	0.53	0.72
Mg	0.24	0.19	0.17	0.19	0.29	0.29	0.19	0.16	0.24	0.25	0.21
Ca	0.20	0.19	0.14	0.21	0.18	0.19	0.21	0.15	0.20	0.17	0.16
Na	0.00	0.00	0.00	0.00	0.00	0.00	0.00	0.00	0.00	0.00	0.00
Total	8	8	8	8	8	8	8	8	8	8	8
X_{Alm}	0.73	0.67	0.63	0.67	0.74	0.75	0.66	0.64	0.71	0.67	0.63
X_{Pyp}	0.08	0.06	0.06	0.07	0.10	0.10	0.07	0.06	0.08	0.09	0.07
X_{Grs}	0.07	0.07	0.05	0.07	0.06	0.07	0.07	0.05	0.07	0.06	0.05
X_{Sps}	0.12	0.20	0.26	0.19	0.09	0.08	0.20	0.26	0.14	0.19	0.24

NOTE: Fe^{3+} contents determined using stoichiometric method of Schumacher (1991)

Appendix 2

In situ U–Pb geochronology of monazite and xenotime

Monazite and xenotime grains were identified in polished thin sections using back-scattered electron imaging and energy dispersive X-ray spectroscopy, drilled out in ~3 mm discs and cast in 25 mm epoxy mounts for SHRIMP analysis, preserving their petrographic context. Standards were in a separate mount to the unknown grains. Wavelength-dispersive X-ray element distribution maps of selected monazite grains were obtained for La, Y and Th using a JEOL JSM 6400R SEM/EPMA at the Centre for Microscopy, Characterisation and Analysis, The University of Western Australia. Operating conditions of 20 kV accelerating voltage and 100 nA beam current were employed. SHRIMP data acquisition procedures for the xenotime and monazite analyses followed the methods described in Fletcher et al. (2004) and Fletcher et al. (2010), respectively. The only procedural variation is that Y contents were not monitored in monazite, but differences in Y are unlikely to have significant matrix effects in these data.

Data were reduced using Squid-2 software (Ludwig, 2009). Corrections for instrumental mass fractionation in Pb/Pb data and for matrix effects in Pb/U and Pb/Th were made separately, using spreadsheet templates. Subsequent calculations and plotting were carried out using Isoplot software (Ludwig, 2001). Normal criteria for data selection/rejection were applied wherever possible, and any variations are indicated for each sample. In most cases, common Pb up to 1% (in ^{206}Pb) and discordance up to 5% (or 1σ if this is larger) are tolerated.

Unless specified otherwise, ^{207}Pb/^{206}Pb ages are weighted mean dates, with 95% statistical confidence limits. In some cases the latter possibly underestimate the true uncertainty because of the requirement for data selection and grouping. The ^{206}Pb/^{238}U and ^{208}Pb/^{232}Th age uncertainties include the (averaged) uncertainty in the corresponding standards reference data, and a notional 1% intermount systematic uncertainty.

Data in plots are shown with 1σ precision. Dark-shaded ellipses are data with ≥10% apparent discordance or >1% common ^{206}Pb; light shaded are >5% discordant.

References

Fletcher, IR, McNaughton, NJ, Aleinikoff, JA, Rasmussen, B and Kamo, SL 2004, Improved calibration procedures and new standards for U–Pb and Th–Pb dating of Phanerozoic xenotime by ion microprobe: Chemical Geology, v. 209, no. 3, p. 295–314.

Fletcher, IR, McNaughton, NJ, Davis, WJ, and Rasmussen, B 2010, Matrix effects and calibration limitations in ion probe U–Pb and Th–Pb dating of monazite: Chemical Geology, v. 270, no. 1, p. 1–44.

Ludwig, KR 2001, User's manual for Isoplot / Ex v. 3.0: a geochronological toolkit for Microsoft Excel: Berkeley Geochronological Center, Special Publication 1a, 56p.

Ludwig, KR 2009, Squid 2.50: a user's manual: Berkeley Geochronology Centre, Berkeley, California, USA, 95p. (unpublished).

Table 2.1. Ion microprobe analytical results for monazite from sample 188998: semipelitic schist, Nick Belt

Group ID	Mount no.	Grain spot	^{238}U (ppm)	^{232}Th (ppm)	$^{232}Th/^{238}U$	f204 (%)	$^{238}U/^{206}Pb$ ± 1s		$^{207}Pb/^{206}Pb$ ± 1s		$^{238}U/^{206}Pb^*$ ± 1s		$^{207}Pb^*/^{206}Pb^*$ ± 1s		$^{238}U/^{206}Pb^*$ date (Ma) ±1s		$^{207}Pb^*/^{206}Pb^*$ date (Ma) ±1s		Disc. (%)
M	1101	E.1-1	252	25603	101.6	1.570	–	–	–	–	3.484	0.075	0.10570	0.00320	1627	31	1727	56	5.8
M	1101	C.1-1	292	16767	57.4	1.640	–	–	–	–	3.330	0.125	0.10600	0.00250	1693	56	1732	43	2.3
M	1101	A.1-2	340	17509	51.5	1.520	–	–	–	–	3.564	0.086	0.10620	0.00260	1594	34	1734	46	8.1
M	1101	A.1-1	354	24380	68.9	1.150	–	–	–	–	3.431	0.062	0.10670	0.00330	1649	26	1744	57	5.4
M	1101	K.1-3	409	21506	52.6	0.830	–	–	–	–	3.686	0.079	0.10710	0.00210	1547	29	1751	36	11.7
M	1101	E.1-2	276	18959	68.7	1.220	–	–	–	–	3.632	0.092	0.10870	0.00250	1568	35	1778	43	11.8
M	1101	F.1-2	180	13473	74.9	1.740	–	–	–	–	3.396	0.083	0.10980	0.00390	1664	36	1796	65	7.3
M2	1101	B.1-2	1921	62792	32.7	0.100	–	–	–	–	4.895	0.093	0.08080	0.00050	1198	21	1218	13	1.6
M2	1101	I.1-1	2024	61078	30.2	0.090	–	–	–	–	5.020	0.103	0.08120	0.00050	1171	22	1226	13	4.5
P	1101	B.1-1	1317	54290	41.2	0.300	–	–	–	–	4.812	0.081	0.08390	0.00130	1217	19	1291	30	5.7
P	1101	L.2-1	1004	31553	31.4	0.590	–	–	–	–	4.427	0.084	0.08880	0.00100	1313	23	1401	22	6.3
P	1101	K.1-1	440	37132	84.4	0.880	–	–	–	–	4.543	0.095	0.09100	0.00210	1282	24	1447	44	11.4
P	1101	D.1-2	487	37492	77.0	0.450	–	–	–	–	4.344	0.077	0.09100	0.00130	1336	21	1448	27	7.7
P	1101	D.1-3	730	33402	45.8	0.600	–	–	–	–	4.527	0.102	0.09180	0.00130	1287	26	1462	27	12.0
P	1101	K.1-2	462	39323	85.1	1.060	–	–	–	–	4.254	0.087	0.09330	0.00230	1361	25	1494	47	8.9
P	1101	J.1-1	288	23043	80.0	1.580	–	–	–	–	4.228	0.079	0.09350	0.00300	1368	23	1498	61	8.7
P	1101	G.1-2	364	23141	63.6	1.510	–	–	–	–	3.882	0.087	0.09410	0.00230	1478	30	1511	46	2.2
P	1101	F.1-1	682	28343	41.6	0.770	–	–	–	–	3.986	0.091	0.09670	0.00130	1443	29	1561	26	7.6
P	1101	G.1-1	387	27411	70.8	1.340	–	–	–	–	3.918	0.071	0.09810	0.00260	1465	24	1589	50	7.8
D	1101	J.2-1	63	13931	221.1	8.120	–	–	–	–	4.531	0.127	0.07330	0.01250	1286	33	1021	344	-26.0
D	1101	L.1-1	1034	30099	29.1	0.720	–	–	–	–	5.203	0.114	0.08420	0.00120	1133	23	1298	28	12.7
D	1101	I.1-2	526	38417	73.0	0.780	–	–	–	–	5.058	0.090	0.08650	0.00220	1163	19	1350	50	13.9
D	1101	M.1-1	146	16167	110.7	4.120	–	–	–	–	4.766	0.123	0.08990	0.00720	1228	29	1423	152	13.7
D	1101	D.1-4	262	22383	85.4	1.930	–	–	–	–	4.429	0.096	0.09320	0.00310	1312	26	1493	64	12.1
D	1101	D.1-1	418	36697	87.8	0.640	–	–	–	–	4.730	0.119	0.09380	0.00180	1236	28	1504	36	17.8
D	1101	J.2-2	111	16383	147.6	2.970	–	–	–	–	4.363	0.095	0.09720	0.00660	1330	26	1572	127	15.4
D	1101	C.2-2	260	23280	89.5	1.070	–	–	–	–	4.305	0.082	0.09960	0.00230	1347	23	1617	44	16.7
D	1101	C.2-1	137	14388	105.0	3.290	–	–	–	–	3.799	0.115	0.10280	0.00570	1506	41	1675	102	10.1

Table 2.2. Ion microprobe analytical results for monazite from sample 188999: semipelitic schist, Nick Belt

Group ID	Mount no.	Grain spot	^{238}U (ppm)	^{232}Th (ppm)	$^{232}Th/^{238}U$	f204 (%)	$^{238}U/^{206}Pb$ ± 1s		$^{207}Pb/^{206}Pb$ ± 1s		$^{238}U/^{206}Pb^*$ ± 1s		$^{207}Pb^*/^{206}Pb^*$ ± 1s		$^{238}U/^{206}Pb^*$ date (Ma) ±1s		$^{207}Pb^*/^{206}Pb^*$ date (Ma) ±1s		Disc. (%)
M	1102	H.2-2	2486	13054	5.3	0.170	–	–	–	–	5.173	0.091	0.07850	0.00070	1139	18	1160	18	1.8
M	1102	H.2-1	1800	15511	8.6	0.350	–	–	–	–	5.015	0.088	0.07870	0.00090	1172	19	1164	24	-0.7
M	1102	A.1-3	2088	4258	2.0	0.120	–	–	–	–	4.978	0.087	0.07880	0.00050	1180	19	1166	13	-1.2
M	1102	D.3-3	3245	5703	1.8	0.080	–	–	–	–	5.028	0.091	0.07890	0.00040	1169	19	1169	11	0.0
M	1102	G.1-3	2286	16922	7.4	0.160	–	–	–	–	4.869	0.090	0.07890	0.00050	1204	20	1169	13	-3.0
M	1102	A.1-2	2448	5687	2.3	0.150	–	–	–	–	4.924	0.099	0.07900	0.00050	1192	22	1171	12	-1.8
M	1102	G.1-2	3463	15909	4.6	0.090	–	–	–	–	4.792	0.087	0.07900	0.00040	1222	20	1173	10	-4.2
M	1102	D.1-3	2267	27878	12.3	0.180	–	–	–	–	4.890	0.088	0.07910	0.00060	1199	20	1174	14	-2.1
M	1102	D.1-1	2341	14220	6.1	0.190	–	–	–	–	4.990	0.087	0.07920	0.00060	1178	19	1177	14	-0.1
M	1102	D.3-1	3219	8961	2.8	0.130	–	–	–	–	5.285	0.092	0.07920	0.00050	1117	18	1178	13	5.2
M	1102	H.1-2	2730	15798	5.8	0.230	–	–	–	–	4.924	0.095	0.07940	0.00050	1192	21	1182	13	-0.8
M	1102	I.1-1	1841	10107	5.5	0.160	–	–	–	–	4.975	0.092	0.07950	0.00070	1181	20	1185	16	0.3
M	1102	I.2-1	3025	15001	5.0	0.100	–	–	–	–	5.128	0.087	0.07960	0.00050	1148	18	1187	12	3.3
M	1102	D.3-2	2638	8763	3.3	0.070	–	–	–	–	5.176	0.086	0.07970	0.00050	1139	17	1189	12	4.2
M	1102	H.1-1	1915	16700	8.7	0.230	–	–	–	–	4.926	0.092	0.07980	0.00070	1191	20	1192	16	0.1
M	1102	D.1-2	1921	13690	7.1	0.110	–	–	–	–	5.120	0.089	0.08000	0.00050	1150	18	1198	13	4.0
M	1102	I.2-2	3269	6679	2.0	0.080	–	–	–	–	5.023	0.083	0.08010	0.00040	1171	18	1199	11	2.3
M	1102	I.1-2	2090	13171	6.3	0.090	–	–	–	–	5.053	0.084	0.08010	0.00050	1164	18	1200	13	3.0
M	1102	D.2-1	4209	7625	1.8	0.090	–	–	–	–	4.921	0.082	0.08020	0.00040	1193	18	1202	11	0.7
M	1102	H.1-3	2091	13300	6.4	0.240	–	–	–	–	4.960	0.086	0.08030	0.00080	1184	19	1205	19	1.7
M	1102	H.2-3	2035	12154	6.0	0.210	–	–	–	–	4.876	0.088	0.08030	0.00060	1203	20	1205	15	0.2
M	1102	A.1-1	2338	7013	3.0	0.140	–	–	–	–	5.005	0.090	0.08050	0.00060	1174	19	1208	14	2.8
M	1102	D.2-2	2927	8109	2.8	0.030	–	–	–	–	4.919	0.090	0.08050	0.00040	1193	20	1209	10	1.3
M	1102	G.1-1	1763	15466	8.8	0.150	–	–	–	–	4.916	0.089	0.08080	0.00060	1194	20	1217	15	1.9
D	1102	C.1-3	2724	19792	7.3	0.210	–	–	–	–	5.342	0.097	0.08080	0.00080	1106	18	1215	18	9.0
D	1102	C.1-1	2193	14471	6.6	0.600	–	–	–	–	5.071	0.093	0.08100	0.00210	1160	19	1222	50	5.1
D	1102	C.1-2	4095	102427	25.0	-0.140	–	–	–	–	8.850	0.172	0.08330	0.00190	690	13	1276	45	45.9

Table 2.3. Ion microprobe analytical results for monazite from sample 36493: pelitic schist, Nick Belt

Group ID	Mount no.	Grain spot	^{238}U (ppm)	^{232}Th (ppm)	$\frac{^{232}Th}{^{238}U}$	f204 (%)	$^{238}U/^{206}Pb$ ± 1s		$^{207}Pb/^{206}Pb$ ± 1s		$^{238}U/^{206}Pb^*$ ± 1s		$^{207}Pb^*/^{206}Pb^*$ ± 1s		$^{238}U/^{206}Pb^*$ date (Ma) ±1s		$^{207}Pb^*/^{206}Pb^*$ date (Ma) ±1s		Disc. (%)
M	0672	B.1-1	14919	35380	2.4	0.259	–	–	–	–	4.801	0.059	0.07973	0.00063	1220	14	1190	15	-2.5
M	0672	E.1-1	2045	75323	36.8	0.273	–	–	–	–	4.652	0.065	0.07973	0.00068	1255	16	1190	17	-5.4
M	0672	B.2-1	9895	42002	4.2	0.077	–	–	–	–	4.792	0.064	0.07979	0.00027	1222	15	1192	7	-2.5
M	0672	B.1-3	6665	38751	5.8	0.459	–	–	–	–	4.939	0.067	0.08013	0.00072	1189	15	1200	18	1.0
M	0672	B.1-2	1879	47620	25.3	0.171	–	–	–	–	4.998	0.067	0.08019	0.00052	1176	14	1202	13	2.2
M	0672	J.1-1	1662	48706	29.3	0.176	–	–	–	–	4.957	0.065	0.08022	0.00060	1185	14	1202	15	1.5
M	0672	C.1-3	2747	23551	8.6	0.039	–	–	–	–	4.951	0.062	0.08052	0.00042	1186	13	1210	10	2.0
M	0672	E.4-1	1443	69571	48.2	0.198	–	–	–	–	4.747	0.062	0.08058	0.00085	1232	15	1211	21	-1.7
M	0672	H.1-3	1584	38703	24.4	0.163	–	–	–	–	5.059	0.064	0.08059	0.00057	1163	13	1211	14	4.0
M	0672	C.1-2	2931	32348	11.0	0.069	–	–	–	–	4.802	0.062	0.08071	0.00041	1219	14	1214	10	-0.4
M	0672	L.1-2	2340	45320	19.4	0.711	–	–	–	–	4.714	0.058	0.08082	0.00107	1240	14	1217	26	-1.9
M	0672	H.1-1	1698	42714	25.2	0.134	–	–	–	–	4.787	0.067	0.08089	0.00081	1223	16	1219	20	-0.3
M	0672	B.2-2	2754	42672	15.5	0.184	–	–	–	–	4.837	0.080	0.08094	0.00062	1211	18	1220	15	0.7
M	0672	C.1-1	2120	13652	6.4	0.102	–	–	–	–	4.854	0.061	0.08094	0.00050	1208	14	1220	12	1.0
M	0672	H.1-2	1574	38975	24.8	0.156	–	–	–	–	4.918	0.065	0.08096	0.00058	1193	14	1220	14	2.2
M	0672	E.3-1	1725	63099	36.6	0.138	–	–	–	–	4.722	0.055	0.08100	0.00060	1238	13	1221	14	-1.4
M	0672	L.1-1	2105	90297	42.9	0.074	–	–	–	–	4.895	0.078	0.08200	0.00050	1198	17	1245	12	3.8
D	0672	J.1-1	2010	29378	14.6	0.098	–	–	–	–	5.145	0.135	0.08074	0.00048	1145	27	1215	12	5.8
D	0672	J.1-2	1290	67379	52.2	1.827	–	–	–	–	5.034	0.071	0.08218	0.00123	1168	15	1250	29	6.6

Table 2.4. Ion microprobe analytical results for monazite from sample 88436: staurolite schist, Tommie Well

Group ID	Mount no.	Grain spot	^{238}U (ppm)	^{232}Th (ppm)	$\frac{^{232}Th}{^{238}U}$	f204 (%)	$^{238}U/^{206}Pb$ ± 1s		$^{207}Pb/^{206}Pb$ ± 1s		$^{238}U/^{206}Pb^*$ ± 1s		$^{207}Pb^*/^{206}Pb^*$ ± 1s		$^{238}U/^{206}Pb^*$ date (Ma) ±1s		$^{207}Pb^*/^{206}Pb^*$ date (Ma) ±1s		Disc. (%)
M	1425	C.2-1	2023	45935	22.7	0.397	–	–	–	–	4.992	0.088	0.08273	0.00057	1177	19	1263	13	6.8
M	1425	I.1-1	6116	11363	1.9	0.036	–	–	–	–	4.501	0.066	0.08299	0.00019	1293	17	1269	4	-1.9
M	1425	I.1-3	5698	12692	2.2	0.042	–	–	–	–	4.821	0.069	0.08309	0.00020	1215	16	1271	5	4.4
M	0673	F.1-1	4957	14800	3.0	0.063	–	–	–	–	4.411	0.051	0.08312	0.00034	1317	14	1272	8	-3.5
M	0673	K.2-1	2055	48055	23.4	0.147	–	–	–	–	4.571	0.067	0.08314	0.00058	1275	17	1272	14	-0.2
M	1425	D.2-1	2182	43158	19.8	0.102	–	–	–	–	4.426	0.068	0.08317	0.00035	1313	18	1273	8	-3.1
M	1425	A.1-1	3352	1345	0.4	0.021	–	–	–	–	4.535	0.071	0.08335	0.00024	1285	18	1278	6	-0.6
M	0673	E.1-3	4337	3529	0.8	0.021	–	–	–	–	4.457	0.063	0.08346	0.00033	1305	17	1280	8	-1.9
M	1425	D.1-1	2466	48421	19.6	0.066	–	–	–	–	4.663	0.066	0.08359	0.00034	1253	16	1283	8	2.4
M	0673	C.1-2	2013	22157	11.0	0.040	–	–	–	–	4.683	0.067	0.08361	0.00043	1248	16	1283	10	2.8
M	0673	E.1-1	6021	3948	0.7	0.022	–	–	–	–	4.551	0.061	0.08362	0.00029	1280	16	1284	7	0.3
M	1425	A.1-2	3015	2753	0.9	0.005	–	–	–	–	4.579	0.066	0.08363	0.00025	1273	17	1284	6	0.8
M	1425	A.1-7	5483	1649	0.3	0.017	–	–	–	–	4.419	0.063	0.08364	0.00019	1315	17	1284	4	-2.4
M	1425	A.1-6	6185	2640	0.4	0.001	–	–	–	–	4.489	0.068	0.08365	0.00017	1296	18	1284	4	-0.9
M	1425	A.1-5	2833	1998	0.7	0.018	–	–	–	–	4.509	0.067	0.08368	0.00026	1291	18	1285	6	-0.5
M	0815	H.1-2	2137	35460	16.6	0.068	–	–	–	–	4.569	0.079	0.08370	0.00032	1276	20	1286	7	0.8
M	1425	A.1-4	5314	4975	0.9	0.016	–	–	–	–	4.426	0.064	0.08373	0.00019	1313	17	1286	4	-2.1
M	0673	C.1-3	3172	25596	8.1	0.040	–	–	–	–	4.516	0.054	0.08376	0.00036	1289	14	1287	8	-0.2
M	1425	I.1-4	4920	7574	1.5	0.013	–	–	–	–	4.648	0.066	0.08380	0.00034	1256	16	1288	8	2.5
M	0673	F.1-2	2801	12433	4.4	0.042	–	–	–	–	4.577	0.060	0.08383	0.00039	1274	15	1289	9	1.1
M	0673	C.1-1	1819	19465	10.7	0.050	–	–	–	–	4.565	0.065	0.08386	0.00045	1277	17	1289	11	1.0
M	0673	E.1-2	6537	3125	0.5	0.009	–	–	–	–	4.419	0.059	0.08389	0.00028	1315	16	1290	7	-2.0
M	0673	K.1-1	1798	62303	34.6	0.114	–	–	–	–	4.591	0.069	0.08412	0.00053	1270	17	1295	12	1.9

Table 2.4. continued

Group ID	Mount no.	Grain spot	^{238}U (ppm)	^{232}Th (ppm)	$^{232}Th/^{238}U$	f204 (%)	$^{238}U/^{206}Pb$ ± 1s		$^{207}Pb/^{206}Pb$ ± 1s		$^{238}U/^{206}Pb^*$ ± 1s		$^{207}Pb^*/^{206}Pb^*$ ± 1s		$^{238}U/^{206}Pb^*$ date (Ma)	±1s	$^{207}Pb^*/^{206}Pb^*$ date (Ma)	±1s	Disc. (%)
M2	1425	I.1-2	5051	36081	7.1	0.047	–	–	–	–	4.784	0.070	0.08153	0.00022	1224	16	1234	5	0.9
M2	0673	L.1-1	1745	74615	42.8	0.224	–	–	–	–	4.540	0.052	0.08202	0.00086	1283	13	1246	20	-3.0
M2	0673	L.1-2	2150	50742	23.6	0.069	–	–	–	–	4.668	0.082	0.08207	0.00046	1251	20	1247	11	-0.3
M2	0673	K.2-2	2288	69247	30.3	0.119	–	–	–	–	4.533	0.060	0.08208	0.00064	1285	15	1247	15	-3.0
M2	0815	F.1-2	2467	28171	11.4	0.053	–	–	–	–	4.670	0.077	0.08214	0.00040	1251	19	1249	10	-0.2
M2	0673	L.1-3	1655	56289	34.0	0.145	–	–	–	–	4.648	0.052	0.08215	0.00057	1256	13	1249	14	-0.6
M2	0815	D.1-2	2487	50894	20.5	0.092	–	–	–	–	4.730	0.076	0.08221	0.00031	1237	18	1251	7	1.1
P	1425	C.4-1	4527	43606	9.6	0.075	–	–	–	–	5.336	0.076	0.07787	0.00026	1107	14	1143	7	3.2
P	0815	D.1-1	6730	47708	7.1	0.413	–	–	–	–	4.917	0.090	0.07917	0.00035	1194	20	1176	9	-1.5
P	0815	H.1-1	4940	43587	8.8	0.042	–	–	–	–	4.879	0.076	0.07969	0.00024	1202	17	1189	6	-1.0
P	1425	B.2-1	9716	44234	4.6	0.022	–	–	–	–	4.851	0.070	0.07976	0.00015	1208	16	1191	4	-1.4
P	1425	B.1-1	9605	47495	4.9	0.013	–	–	–	–	4.909	0.069	0.07986	0.00014	1195	15	1213	6	1.4
P	0815	F.1-1	8051	52768	6.6	0.016	–	–	–	–	4.788	0.067	0.08023	0.00022	1223	16	1215	5	-0.6
P	1425	C.3-1	4098	44344	10.8	0.022	–	–	–	–	4.813	0.066	0.08063	0.00024	1217	15	1213	6	-0.3
P	1425	A.1-3	4333	3059	0.7	0.001	–	–	–	–	4.695	0.064	0.08074	0.00021	1245	16	1215	5	-2.5
D	1425	B.3-1	6091	37403	6.1	0.045	–	–	–	–	5.665	0.427	0.07834	0.00249	1048	73	1155	63	9.3

Table 2.5. Ion microprobe analytical results for xenotime from sample 88436: staurolite schist, Tommie Well

Group ID	Mount no.	Grain spot	^{238}U (ppm)	^{232}Th (ppm)	$^{232}Th/^{238}U$	f204 (%)	$^{238}U/^{206}Pb$ ± 1s		$^{207}Pb/^{206}Pb$ ± 1s		$^{238}U/^{206}Pb^*$ ± 1s		$^{207}Pb^*/^{206}Pb^*$ ± 1s		$^{238}U/^{206}Pb^*$ date (Ma) ±1s		$^{207}Pb^*/^{206}Pb^*$ date (Ma) ±1s		Disc. (%)
M	0815	F.3-2	5439	915	0.168	0.091	–	–	–	–	4.390	0.072	0.08485	0.00030	1323	20	1312	7	-0.8
M	1425	J.1-1	3577	633	0.177	0.000	–	–	–	–	4.418	0.072	0.08603	0.00043	1315	19	1339	10	1.7
M	0815	F.1-2	3977	763	0.192	0.028	–	–	–	–	4.496	0.095	0.08664	0.00061	1295	25	1353	13	4.3
M2	1425	J.1-2	5266	500	0.095	0.052	–	–	–	–	5.075	0.083	0.07847	0.00027	1159	17	1159	7	0.0
M2	0815	I.1-1	5700	480	0.084	0.012	–	–	–	–	4.806	0.110	0.07867	0.00023	1219	25	1164	6	-4.7
M2	0815	H.1-1	4864	456	0.094	0.040	–	–	–	–	4.709	0.077	0.07974	0.00037	1241	19	1191	9	-4.3
M2	0673	C.1-1	5707	652	0.114	0.026	–	–	–	–	5.172	0.098	0.07979	0.00026	1140	20	1192	6	4.4
M2	1425	M.1-2	3945	1184	0.300	0.013	–	–	–	–	4.902	0.080	0.08055	0.00031	1197	18	1210	7	1.1
P	0815	I.1-2	3909	1038	0.266	0.236	–	–	–	–	3.704	0.095	0.09347	0.00082	1541	35	1497	17	-2.9
P	1425	N.1-1	4872	1139	0.234	0.025	–	–	–	–	3.695	0.061	0.09673	0.00028	1544	23	1562	5	1.1
P	1425	K.2-1	4332	894	0.206	0.000	–	–	–	–	3.588	0.059	0.09928	0.00027	1585	23	1611	5	1.6
P	1425	K.1-1	5641	952	0.169	0.012	–	–	–	–	3.648	0.060	0.09955	0.00024	1562	23	1616	4	3.3
P	1425	L.1-1	4816	1087	0.226	0.009	–	–	–	–	3.311	0.054	0.10106	0.00046	1701	25	1644	8	-3.5
P	1425	K.1-2	5193	1109	0.214	0.010	–	–	–	–	3.593	0.066	0.10114	0.00035	1583	26	1645	6	3.8
P	1425	M.1-1	4535	696	0.154	0.012	–	–	–	–	3.366	0.062	0.10215	0.00027	1677	27	1664	5	-0.8
P	1425	L.1-2	5916	1405	0.238	0.000	–	–	–	–	3.269	0.073	0.10242	0.00024	1720	34	1668	4	-3.1
P	1425	M.1-3	3919	561	0.143	0.009	–	–	–	–	3.469	0.056	0.10288	0.00029	1633	23	1677	5	2.6
D	0815	F.3-1	5357	643	0.120	0.143	–	–	–	–	5.211	0.086	0.07339	0.00052	1132	17	1025	14	-10.4
D	0815	F.2-1	6690	622	0.093	0.037	–	–	–	–	5.297	0.102	0.07424	0.00032	1115	20	1048	9	-6.4
D	0815	F.3-3	4880	566	0.116	0.003	–	–	–	–	5.152	0.084	0.07542	0.00050	1144	17	1080	13	-5.9
D	1425	L.2-1	3611	701	0.194	0.032	–	–	–	–	4.285	0.089	0.07934	0.00038	1352	25	1181	9	-14.5
D	0673	C.1-2	5540	1471	0.266	0.005	–	–	–	–	4.207	0.069	0.09298	0.00061	1375	20	1488	12	7.6

Table 2.6. Ion microprobe analytical results for monazite from sample 88475: metasomatic schist, New Well 10

Group ID	Mount no.	Grain spot	^{238}U (ppm)	^{232}Th (ppm)	$^{232}Th/^{238}U$	f204 (%)	$^{238}U/^{206}Pb$ ± 1s		$^{207}Pb/^{206}Pb$ ± 1s		$^{238}U/^{206}Pb^*$ ± 1s		$^{207}Pb^*/^{206}Pb^*$ ± 1s		$^{238}U/^{206}Pb^*$ date (Ma) ±1s		$^{207}Pb^*/^{206}Pb^*$ date (Ma) ±1s		Disc. (%)
M	0563	K.1-2	3491	45129	12.9	0.008	–	–	–	–	3.023	0.038	0.10840	0.00035	1842	20	1773	6	-3.9
M	0563	H.1-3	6352	53276	8.4	0.020	–	–	–	–	3.063	0.040	0.10843	0.00025	1821	20	1773	4	-2.7
M	0563	J.1-2	3883	43663	11.2	0.032	–	–	–	–	3.061	0.040	0.10850	0.00034	1822	21	1774	6	-2.7
M	0563	E.1-1	9842	46602	4.7	-0.001	–	–	–	–	3.112	0.042	0.10850	0.00020	1797	21	1774	3	-1.2
M	0563	D.1-3	7311	59104	8.1	0.004	–	–	–	–	3.117	0.040	0.10857	0.00024	1794	20	1775	4	-1.0
M	0563	G.1-1	9036	46481	5.1	0.006	–	–	–	–	3.094	0.038	0.10862	0.00021	1805	19	1776	4	-1.6
M	0563	D.1-1	4910	69665	14.2	0.024	–	–	–	–	3.171	0.039	0.10863	0.00032	1767	19	1777	5	0.5
M	0563	G.1-3	9916	52878	5.3	0.005	–	–	–	–	3.139	0.043	0.10869	0.00020	1783	21	1778	3	-0.3
M	0563	L.1-3	8581	58976	6.9	0.009	–	–	–	–	3.184	0.037	0.10870	0.00017	1761	18	1778	3	1.0
M	0563	E.1-2	6167	45641	7.4	0.005	–	–	–	–	3.114	0.042	0.10884	0.00026	1795	21	1780	4	-0.8
M	0509	H.1-10	2579	66553	25.8	0.022	–	–	–	–	3.110	0.048	0.10885	0.00071	1797	24	1780	12	-1.0
M	0563	C.1-2	7592	52368	6.9	0.015	–	–	–	–	3.177	0.043	0.10885	0.00034	1764	21	1780	6	0.9
M	0509	H.1-9	2842	71102	25.0	0.019	–	–	–	–	3.154	0.043	0.10891	0.00071	1776	21	1781	12	0.3
M	0509	H.1-12	1773	41615	23.5	-0.001	–	–	–	–	3.071	0.052	0.10902	0.00073	1817	27	1783	12	-1.9
M	0563	E.1-3	5647	65492	11.6	0.033	–	–	–	–	3.204	0.039	0.10903	0.00029	1751	19	1783	5	1.8
M	0563	D.1-2	9379	43385	4.6	0.009	–	–	–	–	3.164	0.048	0.10906	0.00020	1771	23	1784	3	0.7
M	0509	F.1-12	6676	52966	7.9	0.014	–	–	–	–	3.116	0.039	0.10906	0.00067	1794	20	1784	11	-0.6
M	0509	H.2-6	5415	38849	7.2	0.013	–	–	–	–	3.195	0.046	0.10912	0.00068	1755	22	1785	11	1.7
M	0563	G.1-2	5767	60677	10.5	-0.009	–	–	–	–	3.113	0.040	0.10918	0.00027	1796	20	1786	5	-0.6
M	0509	H.1-13	2473	51130	20.7	0.007	–	–	–	–	3.211	0.056	0.10921	0.00082	1748	27	1786	14	2.1
M	0563	L.1-1	10161	74894	7.4	0.008	–	–	–	–	3.127	0.034	0.10926	0.00021	1789	17	1787	3	-0.1
M	0563	L.1-2	6086	60122	9.9	0.012	–	–	–	–	3.115	0.038	0.10929	0.00027	1795	19	1788	5	-0.4
M	0563	J.1-1	4027	46225	11.5	0.011	–	–	–	–	3.095	0.038	0.10929	0.00029	1805	19	1788	5	-1.0
M	0563	J.1-3	4108	43462	10.6	-0.004	–	–	–	–	2.993	0.035	0.10944	0.00031	1858	19	1790	5	-3.8
M2	0509	I.2-2	16133	51769	3.2	0.010	–	–	–	–	4.842	0.079	0.07843	0.00020	1210	18	1158	5	-4.5
M2	0509	I.1-8	15577	46084	3.0	0.027	–	–	–	–	4.927	0.070	0.07855	0.00048	1191	16	1161	12	-2.6
M2	0509	I.2-6	14208	49574	3.5	0.020	–	–	–	–	4.901	0.067	0.07872	0.00048	1197	15	1165	12	-2.7
M2	0509	B.1-4	12154	45622	3.8	0.039	–	–	–	–	4.966	0.067	0.07885	0.00052	1183	15	1168	13	-1.2
M2	0509	H.1-4	17909	50858	2.8	0.016	–	–	–	–	4.776	0.074	0.07886	0.00013	1225	17	1169	3	-4.9
M2	0509	H.1-7	16116	44029	2.7	0.020	–	–	–	–	4.815	0.072	0.07897	0.00048	1216	17	1171	12	-3.9
M2	0509	F.1-3	19524	46348	2.4	0.016	–	–	–	–	4.798	0.073	0.07900	0.00012	1220	17	1172	3	-4.1
M2	0509	F.1-2	15969	52262	3.3	0.018	–	–	–	–	4.722	0.073	0.07916	0.00013	1238	17	1176	3	-5.3
M2	0509	F.1-13	18943	41333	2.2	0.017	–	–	–	–	4.845	0.078	0.07925	0.00048	1210	18	1178	12	-2.7
M2	0509	I.1-9	10840	42869	4.0	0.015	–	–	–	–	4.885	0.070	0.07928	0.00049	1201	16	1179	12	-1.8

Table 2.6. continued

Group ID	Mount no.	Grain spot	^{238}U (ppm)	^{232}Th (ppm)	$^{232}Th/^{238}U$	f204 (%)	$^{238}U/^{206}Pb$ ± 1s		$^{207}Pb/^{206}Pb$ ± 1s		$^{238}U/^{206}Pb^*$ ± 1s		$^{207}Pb^*/^{206}Pb^*$ ± 1s		$^{238}U/^{206}Pb^*$ date (Ma)	±1s	$^{207}Pb^*/^{206}Pb^*$ date (Ma)	±1s	Disc. (%)
M3	0509	I.2-4	5332	56562	10.6	0.054	–	–	–	–	6.409	0.097	0.07099	0.00020	935	13	957	6	2.3
M3	0509	I.2-7	1501	54489	36.3	0.179	–	–	–	–	6.502	0.128	0.07154	0.00071	922	17	973	20	5.2
M3	0509	B.1-5	6262	47323	7.6	0.294	–	–	–	–	5.832	0.085	0.07233	0.00064	1020	14	995	18	-2.5
M3	0509	F.1-10	1571	54111	34.5	0.178	–	–	–	–	6.211	0.093	0.07248	0.00071	962	13	999	20	3.7
P	0509	I.1-4	9887	40072	4.1	0.042	–	–	–	–	5.991	0.092	0.07275	0.00046	995	14	1007	13	1.2
P	0509	I.1-3	11522	62097	5.4	0.016	–	–	–	–	5.623	0.076	0.07326	0.00023	1055	13	1021	6	-3.3
P	0509	I.1-4	12812	71250	5.6	0.030	–	–	–	–	5.417	0.104	0.07389	0.00014	1092	19	1039	4	-5.2
P	0509	B.1-1	11780	45909	3.9	0.020	–	–	–	–	5.353	0.080	0.07524	0.00019	1104	15	1075	5	-2.7
P	0509	I.2-3	14481	53087	3.7	0.018	–	–	–	–	5.214	0.085	0.07587	0.00013	1131	17	1092	3	-3.6
P	0509	I.2-1	16313	57264	3.5	0.018	–	–	–	–	4.999	0.068	0.07684	0.00013	1176	15	1117	3	-5.2
P	0563	C.1-1	16605	57900	3.5	0.027	–	–	–	–	4.941	0.054	0.08001	0.00019	1188	12	1197	5	0.8
P	0509	F.1-9	4105	57501	14.0	0.141	–	–	–	–	4.328	0.060	0.08715	0.00096	1340	17	1364	21	1.7
P	0509	F.1-1	3142	68255	21.7	0.353	–	–	–	–	3.782	0.099	0.09359	0.00172	1513	35	1500	35	-0.8
P	0509	H.1-3	2839	65650	23.1	0.013	–	–	–	–	3.322	0.054	0.10449	0.00025	1696	24	1705	4	0.5
P	0509	F.1-7	8941	56593	6.3	-0.001	–	–	–	–	3.112	0.048	0.10594	0.00023	1796	24	1731	4	-3.8
P	0509	H.1-5	2364	59001	25.0	0.014	–	–	–	–	3.107	0.045	0.10611	0.00040	1799	23	1734	7	-3.8
P	0563	H.1-1	6309	32057	5.1	0.013	–	–	–	–	3.375	0.039	0.10634	0.00019	1673	17	1738	3	3.7
P	0509	H.2-3	2045	43571	21.3	-0.003	–	–	–	–	3.247	0.045	0.10667	0.00026	1731	21	1743	4	0.7
P	0563	K.1-1	2870	34663	12.1	-0.006	–	–	–	–	3.430	0.055	0.10675	0.00033	1649	23	1745	6	5.5
P	0509	H.1-2	4516	66312	14.7	-0.009	–	–	–	–	3.203	0.052	0.10688	0.00033	1752	25	1747	6	-0.3
P	0509	H.1-6	2080	49062	23.6	-0.021	–	–	–	–	3.060	0.056	0.10690	0.00040	1823	29	1747	7	-4.3
P	0509	H.2-2	3026	46623	15.4	0.012	–	–	–	–	3.166	0.046	0.10706	0.00023	1770	23	1750	4	-1.1
P	0509	B.1-3	3034	41164	13.6	0.018	–	–	–	–	3.035	0.058	0.10711	0.00025	1836	30	1751	4	-4.9
P	0509	F.1-4	13692	51029	3.7	0.002	–	–	–	–	3.059	0.050	0.10732	0.00015	1823	26	1754	3	-3.9
P	0509	B.1-2	8046	47740	5.9	0.003	–	–	–	–	3.067	0.058	0.10758	0.00028	1819	30	1759	5	-3.4
P	0509	H.2-4	5433	43453	8.0	0.013	–	–	–	–	3.300	0.053	0.10768	0.00067	1707	24	1760	11	3.1
P	0509	F.1-5	8299	57623	6.9	0.001	–	–	–	–	3.040	0.047	0.10784	0.00035	1833	25	1763	6	-4.0
P	0509	H.2-1	8684	44486	5.1	0.006	–	–	–	–	3.124	0.050	0.10785	0.00025	1790	25	1763	4	-1.5
P	0563	C.1-3	8861	46425	5.2	0.020	–	–	–	–	3.191	0.038	0.10793	0.00022	1757	18	1765	4	0.4
P	0509	F.1-6	10517	53123	5.1	0.005	–	–	–	–	3.088	0.048	0.10799	0.00016	1809	25	1766	3	-2.4
P	0509	F.1-8	10805	51203	4.7	0.002	–	–	–	–	3.127	0.044	0.10823	0.00027	1789	22	1770	5	-1.1

Table 2.6. continued

Group ID	Mount no.	Grain spot	^{238}U (ppm)	^{232}Th (ppm)	$^{232}Th/^{238}U$	f204 (%)	$^{238}U/^{206}Pb$ ± 1s		$^{207}Pb/^{206}Pb$ ± 1s		$^{238}U/^{206}Pb^*$ ± 1s		$^{207}Pb^*/^{206}Pb^*$ ± 1s		$^{238}U/^{206}Pb^*$ date (Ma)	±1s	$^{207}Pb^*/^{206}Pb^*$ date (Ma)	±1s	Disc. (%)
D	0509	I.1-6	1071	45035	42.1	0.408	–	–	–	–	6.532	0.146	0.07300	0.00106	918	19	1014	29	9.4
D	0509	H.1-8	7595	54146	7.1	0.040	–	–	–	–	6.254	0.106	0.07320	0.00049	956	15	1019	13	6.2
D	0509	F.1-11	1429	51214	35.8	0.103	–	–	–	–	6.280	0.096	0.07345	0.00067	953	14	1026	19	7.2
D	0509	I.1-5	1389	58210	41.9	0.355	–	–	–	–	6.270	0.101	0.07420	0.00089	954	14	1047	24	8.9
D	0509	H.1-1	18046	48770	2.7	0.015	–	–	–	–	4.756	0.070	0.07858	0.00016	1230	16	1162	4	-5.9
D	0509	H.1-11	9385	53737	5.7	0.390	–	–	–	–	3.679	0.103	0.10208	0.00107	1550	39	1662	19	6.8
D	0563	K.1-3	8998	48891	5.4	0.006	–	–	–	–	3.487	0.386	0.10847	0.00426	1626	159	1774	72	8.4
D	0563	H.1-2	6170	54532	8.8	-0.006	–	–	–	–	2.937	0.037	0.10899	0.00025	1889	21	1783	4	-6.0

Table 2.7. Ion microprobe analytical results for xenotime from sample 88475: metasomatic schist, New Well 10

Group ID	Mount no.	Grain spot	^{238}U (ppm)	^{232}Th (ppm)	$^{232}Th/^{238}U$	f204 (%)	$^{238}U/^{206}Pb$ ± 1s		$^{207}Pb/^{206}Pb$ ± 1s		$^{238}U/^{206}Pb^*$ ± 1s		$^{207}Pb^*/^{206}Pb^*$ ± 1s		$^{238}U/^{206}Pb^*$ date (Ma)	±1s	$^{207}Pb^*/^{206}Pb^*$ date (Ma)	±1s	Disc. (%)
M	0508	I.1-2a	10829	1606	0.15	0.003	–	–	–	–	2.968	0.061	0.11096	0.00044	1872	33	1815	7	-3.1
M	0508	I.1-3a	12043	1730	0.14	0.001	–	–	–	–	2.987	0.060	0.11052	0.00026	1862	33	1808	4	-3.0
M	0508	I.1-3b	–	–	–	0.005	–	–	–	–	–	–	0.11012	0.00027	–	–	1801	4	–
M	0508	I.1-2b	–	–	–	0.002	–	–	–	–	–	–	0.11004	0.00035	–	–	1800	6	–
M2	0508	G.1-2a	11696	534	0.05	0.007	–	–	–	–	4.478	0.087	0.08298	0.00038	1299	23	1269	9	-2.4
M2	0508	G.1-2b	–	–	–	-0.001	–	–	–	–	–	–	0.08178	0.00040	–	–	1240	9	–
M2	0508	G.1-4a	7371	498	0.07	0.012	–	–	–	–	4.795	0.081	0.08028	0.00026	1221	19	1204	6	-1.4
M2	0508	G.1-3a	8299	494	0.06	-0.007	–	–	–	–	4.819	0.082	0.08021	0.00025	1215	19	1202	6	-1.1
M2	0508	G.1-1a	7529	551	0.07	0.004	–	–	–	–	4.995	0.090	0.08008	0.00025	1176	19	1199	6	1.9
M2	0508	G.1-3b	–	–	–	0.012	–	–	–	–	–	–	0.07939	0.00026	–	–	1182	7	–
P	0508	I.1-1a	10319	1128	0.11	0.003	–	–	–	–	3.253	0.068	0.10561	0.00062	1728	32	1725	11	-0.2
P	0508	I.1-1b	–	–	–	0.001	–	–	–	–	–	–	0.09979	0.00092	–	–	1620	17	–

Table 2.8. Ion microprobe analytical results for monazite from sample 46981: pelitic schist, Nardoo Well

Group ID	Mount no.	Grain spot	^{238}U (ppm)	^{232}Th (ppm)	$\frac{^{232}Th}{^{238}U}$	f204 (%)	$^{238}U/^{206}Pb$ ± 1s		$^{207}Pb/^{206}Pb$ ± 1s		$^{238}U/^{206}Pb^*$ ± 1s		$^{207}Pb^*/^{206}Pb^*$ ± 1s		$^{238}U/^{206}Pb^*$ date (Ma) ±1s		$^{207}Pb^*/^{206}Pb^*$ date (Ma) ±1s		Disc. (%)
M	0674	J.1-1	1349	73696	54.6	0.207	–	–	–	–	4.578	0.121	0.08197	0.00063	1274	31	1245	15	-2.3
M	0674	G.1-2	1742	70803	40.6	0.213	–	–	–	–	4.713	0.131	0.08233	0.00070	1241	31	1253	17	1.0
M	0674	G.1-1	809	42299	52.3	0.250	–	–	–	–	4.437	0.124	0.08235	0.00076	1310	33	1254	18	-4.5
M	0674	I.1-2	991	45503	45.9	0.174	–	–	–	–	4.576	0.121	0.08238	0.00062	1274	31	1255	15	-1.5
M	0674	J.1-2	642	34320	53.4	0.251	–	–	–	–	4.548	0.125	0.08258	0.00084	1281	32	1259	20	-1.7
M	0674	A.1-1	1978	20592	10.4	0.092	–	–	–	–	4.535	0.118	0.08268	0.00059	1285	30	1262	14	-1.8
M	0674	F.1-2	2330	7124	3.1	0.075	–	–	–	–	4.808	0.131	0.08298	0.00041	1218	30	1269	10	4.0
M	0674	A.1-2	1459	49442	33.9	0.079	–	–	–	–	4.358	0.113	0.08319	0.00048	1332	31	1274	11	-4.5
M	0674	D.1-2	985	46927	47.6	0.198	–	–	–	–	4.606	0.127	0.08324	0.00083	1267	32	1275	20	0.7
M	0674	D.1-1	988	64945	65.7	0.210	–	–	–	–	4.574	0.120	0.08340	0.00068	1275	30	1279	16	0.3
M	0674	E.1-2	1708	62673	36.7	0.123	–	–	–	–	4.659	0.131	0.08344	0.00051	1254	32	1280	12	2.0
M	0674	E.1-1	851	30077	35.4	0.045	–	–	–	–	4.937	0.135	0.08361	0.00067	1189	30	1284	16	7.4
M	0674	F.1-1	2658	5925	2.2	0.053	–	–	–	–	4.553	0.120	0.08375	0.00039	1280	31	1287	9	0.5
M	0674	I.1-1	929	67029	72.2	0.249	–	–	–	–	4.645	0.123	0.08487	0.00080	1257	30	1313	18	4.3

Table 2.9. Ion microprobe analytical results for xenotime from sample 46981: pelitic schist, Nardoo Well

Group ID	Mount no.	Grain spot	^{238}U (ppm)	^{232}Th (ppm)	$\frac{^{232}Th}{^{238}U}$	f204 (%)	$^{238}U/^{206}Pb$ ± 1s		$^{207}Pb/^{206}Pb$ ± 1s		$^{238}U/^{206}Pb^*$ ± 1s		$^{207}Pb^*/^{206}Pb^*$ ± 1s		$^{238}U/^{206}Pb^*$ date (Ma) ±1s		$^{207}Pb^*/^{206}Pb^*$ date (Ma) ±1s		Disc. (%)
M	0676	H.1-4	1313	4677	3.56	0.060	–	–	–	–	3.823	0.168	0.09723	0.00099	1498	59	1572	19	4.7
M	0676	H.1-3	4390	3514	0.80	0.000	–	–	–	–	4.841	0.204	0.08300	0.00050	1210	47	1269	12	4.6
M	0676	H.3-2	3097	2359	0.76	0.061	–	–	–	–	4.877	0.205	0.07979	0.00093	1202	46	1192	23	-0.9
M	0676	H.1-2	5516	3477	0.63	0.018	–	–	–	–	5.352	0.227	0.07885	0.00044	1104	43	1168	11	5.5
M	0676	H.3-1	4242	3187	0.75	0.012	–	–	–	–	5.054	0.213	0.07882	0.00086	1164	45	1168	22	0.3
D	0676	H.2-1	1587	5481	3.45	0.029	–	–	–	–	4.489	0.196	0.09534	0.00091	1297	51	1535	18	15.5
D	0676	H.1-1	5419	3007	0.55	-0.011	–	–	–	–	6.074	0.257	0.07438	0.00046	982	39	1052	13	6.6

Table 3.1. Ion microprobe analytical results for zircons from sample 195826: monzogranitic gneiss, McCarthy Well

Group ID	Spot no.	Grain spot	^{238}U (ppm)	^{232}Th (ppm)	$^{232}Th/^{238}U$	f204 (%)	$^{238}U/^{206}Pb$	± 1s	$^{207}Pb/^{206}Pb$	± 1s	$^{238}U/^{206}Pb^*$	± 1s	$^{207}Pb^*/^{206}Pb^*$	± 1s	$^{238}U/^{206}Pb^*$ date (Ma)	±1s	$^{207}Pb^*/^{206}Pb^*$ date (Ma)	±1s	Disc. (%)
I	27	22.1	150	130	0.90	-0.016	3.402	0.039	0.10093	0.00062	3.402	0.039	0.10107	0.00063	1661	17	1644	12	-1.1
I	28	23.1	197	162	0.85	0.103	3.468	0.038	0.10223	0.00219	3.471	0.038	0.10133	0.00222	1632	16	1649	41	1.0
I	31	25.1	385	2	0.01	-0.007	3.365	0.032	0.10147	0.00040	3.364	0.032	0.10153	0.00041	1678	14	1652	7	-1.5
I	15	12.1	221	231	1.08	0.050	3.421	0.035	0.10238	0.00049	3.423	0.035	0.10195	0.00052	1652	15	1660	10	0.5
I	26	21.1	100	82	0.85	0.069	3.426	0.044	0.10259	0.00074	3.428	0.044	0.10199	0.00082	1650	19	1661	15	0.6
I	21	17.1	129	97	0.77	0.037	3.513	0.042	0.10236	0.00362	3.515	0.042	0.10204	0.00363	1614	17	1662	66	2.9
I	9	8.1	285	280	1.01	0.032	3.440	0.034	0.10237	0.00046	3.441	0.034	0.10209	0.00048	1645	14	1662	9	1.1
I	14	11.1	231	222	0.99	0.038	3.422	0.034	0.10253	0.00048	3.423	0.035	0.10220	0.00050	1652	15	1664	9	0.7
I	19	15.1	363	256	0.73	0.020	3.418	0.031	0.10251	0.00040	3.418	0.031	0.10234	0.00041	1654	14	1667	7	0.8
I	1	1.1	141	114	0.83	-0.059	3.381	0.055	0.10235	0.00076	3.379	0.055	0.10286	0.00081	1671	24	1676	15	0.3
I	11	9.1	138	155	1.16	0.032	3.427	0.039	0.10363	0.00062	3.428	0.039	0.10336	0.00065	1650	17	1685	12	2.1
I	24	19.1	136	110	0.84	0.000	3.420	0.040	0.10362	0.00065	3.420	0.040	0.10362	0.00065	1653	17	1690	12	2.2
P	12	4.4	42	0	0.00	0.549	4.910	0.086	0.08131	0.00667	4.937	0.087	0.07669	0.00697	1189	19	1113	181	-6.8
P	16	4.5	67	2	0.02	0.104	4.928	0.072	0.08051	0.00093	4.933	0.072	0.07963	0.00112	1190	16	1188	28	-0.2
P	23	18.1	119	91	0.79	0.000	3.871	0.047	0.09583	0.00070	3.871	0.047	0.09583	0.00070	1481	16	1544	14	4.1
P	25	20.1	162	121	0.77	0.059	3.375	0.038	0.10074	0.00058	3.376	0.038	0.10023	0.00064	1672	17	1628	12	-2.7
M	32	26.1	15	1	0.05	0.270	4.960	0.144	0.08471	0.00222	4.973	0.145	0.08241	0.00320	1181	32	1255	76	5.9
M	4	4.1	23	0	0.00	0.000	4.966	0.130	0.08378	0.00173	4.966	0.130	0.08378	0.00173	1183	29	1287	40	8.1
M	2	2.1	26	0	0.01	-0.159	4.825	0.124	0.08365	0.00188	4.817	0.124	0.08500	0.00232	1216	29	1316	53	7.6
M	8	7.1	28	0	0.00	-0.479	4.751	0.100	0.08222	0.00145	4.728	0.100	0.08630	0.00249	1237	24	1345	56	8.0
M	18	14.1	96	7	0.08	0.412	4.510	0.064	0.09010	0.00094	4.529	0.064	0.08659	0.00151	1286	17	1351	34	4.8

Table 3.1. continued

Group ID	Spot no.	Grain spot	^{238}U (ppm)	^{232}Th (ppm)	$^{232}Th/^{238}U$	f204 (%)	$^{238}U/^{206}Pb$ ± 1s		$^{207}Pb/^{206}Pb$ ± 1s		$^{238}U/^{206}Pb^*$ ± 1s		$^{207}Pb^*/^{206}Pb^*$ ± 1s		$^{238}U/^{206}Pb^*$ date (Ma) ±1s		$^{207}Pb^*/^{206}Pb^*$ date (Ma) ±1s		Disc. (%)
M2	33	27.1	3796	23	0.01	0.016	4.647	0.039	0.07983	0.00016	4.648	0.039	0.07969	0.00017	1256	10	1189	4	-5.6
M2	39	28.3	3380	14	0.00	0.027	4.470	0.038	0.08011	0.00018	4.471	0.038	0.07988	0.00019	1301	10	1194	5	-9.0
M2	40	4.9	1195	3	0.00	0.043	4.923	0.044	0.08025	0.00030	4.925	0.044	0.07989	0.00033	1192	10	1194	8	0.2
M2	35	27.2	1086	5	0.01	0.242	5.020	0.046	0.08200	0.00185	5.032	0.046	0.07995	0.00189	1169	10	1196	47	2.3
M2	34	28.1	4179	22	0.01	0.010	4.538	0.038	0.08012	0.00016	4.538	0.038	0.08004	0.00016	1284	10	1198	4	-7.2
M2	6	5.1	3710	17	0.00	0.011	4.564	0.064	0.08019	0.00016	4.564	0.064	0.08009	0.00016	1277	16	1199	4	-6.5
M2	42	4.7	4157	19	0.00	0.021	4.545	0.038	0.08028	0.00016	4.546	0.038	0.08010	0.00016	1282	10	1200	4	-6.8
M2	43	4.8	3850	18	0.00	0.011	4.535	0.038	0.08024	0.00016	4.536	0.038	0.08015	0.00017	1284	10	1201	4	-7.0
M2	36	28.2	3824	17	0.00	0.009	4.572	0.038	0.08029	0.00016	4.572	0.038	0.08021	0.00017	1275	10	1202	4	-6.1
M2	5	4.2	2682	8	0.00	0.012	4.598	0.063	0.08039	0.00015	4.598	0.063	0.08029	0.00015	1269	16	1204	4	-5.4
M2	37	27.3	2565	18	0.01	0.009	4.750	0.040	0.08042	0.00020	4.750	0.040	0.08034	0.00020	1232	10	1205	5	-2.2
M2	41	4.6	3093	16	0.01	0.012	4.572	0.038	0.08051	0.00018	4.572	0.038	0.08041	0.00018	1275	10	1207	4	-5.6
M2	38	27.4	1292	13	0.01	0.134	4.890	0.044	0.08165	0.00030	4.896	0.044	0.08052	0.00038	1198	10	1210	9	1.0
D	10	4.3	33	0	0.00	1.569	5.032	0.097	0.08270	0.00141	5.112	0.101	0.06964	0.00395	1152	21	918	117	-25.5
D	22	17.2	26	0	0.01	1.609	4.947	0.110	0.08589	0.00178	5.028	0.114	0.07244	0.00469	1169	25	998	132	-17.1
D	30	7.2	31	1	0.03	2.113	5.509	0.124	0.09230	0.00195	5.628	0.132	0.07457	0.00582	1054	23	1057	157	0.3
D	17	13.1	63	1	0.02	0.100	5.349	0.076	0.08280	0.00092	5.354	0.076	0.08195	0.00110	1104	15	1244	26	11.3
D	3	3.1	56	0	0.00	-0.507	4.905	0.097	0.08200	0.00113	4.881	0.097	0.08633	0.00198	1202	22	1345	44	10.7
D	13	10.1	34	3	0.11	0.000	6.850	0.136	0.08857	0.00198	6.850	0.136	0.08857	0.00198	878	17	1395	43	37.0
D	20	16.1	104	22	0.22	-0.059	4.387	0.054	0.08822	0.00075	4.385	0.054	0.08872	0.00083	1324	15	1398	18	5.3
D	7	6.1	15	0	0.01	-0.930	6.390	0.179	0.08529	0.00986	6.331	0.180	0.09328	0.01079	945	26	1493	219	36.7
D	29	24.1	23	0	0.02	-0.083	4.692	0.113	0.18171	0.15185	4.688	0.120	0.18245	0.15191	1246	30	2675	1378	53.4

Table 4.1. Phases and *a–x* models used in the phase equilibria modelling

		Chemical system			
Phase	*Abbreviation*	*NCFMASHTO*	*MnNCFMASHTO*	*NCKFMASHTO*	*MnNCKFMASHTO*[(a)]
actinolite	act	Diener et al. (2007)	Diener et al. (2007)	–	–
biotite	bi	–	–	White et al. (2007)	White et al. (2005)
chlorite	chl	Holland et al. (1998)	Holland et al. (1998)	Holland et al. (1998)	combination of Mahar et al. (1997) and Holland et al. (1998)
chloritoid	ctd	–	–	White et al. (2000)	combination of White et al. (2000) and Mahar et al. (1997)
clinopyroxene	cpx	Green et al. (2007)	Green et al. (2007)	–	–
cordierite	cd	–	–	Holland and Powell (1998)	combination of Mahar et al. (1997) and Holland and Powell (1998)
epidote	ep	Holland and Powell (1998)	Holland and Powell (1998)	Holland and Powell (1998)	–
garnet	g	White et al. (2007)	White et al. (2005)	White et al. (2007)	White et al. (2005)
glaucophane	gl	Diener et al. (2007)	Diener et al. (2007)	–	–
hornblende	hb	Diener et al. (2007)	Diener et al. (2007)	–	–
ilmenite	ilm	White et al. (2000)	White et al. (2005)	White et al. (2000)	White et al. (2005)
K-feldspar	ksp	–	–	Holland and Powell (2003)	Holland and Powell (2003)
magnetite	mt	White et al. (2000)	White et al. (2000)	White et al. (2002)	White et al. (2000)
muscovite	mu	–	–	Coggon and Holland (2002)	Coggon and Holland (2002)
orthopyroxene	opx	–	–	White et al. (2002)	White et al. (2002)
plagioclase	pl	Holland and Powell (2003)	Holland and Powell (2003)	Holland and Powell (2003)	Holland and Powell (2003)
silicate melt	liq	–	–	White et al. (2007)	White et al. (2007)
staurolite	st	–	–	Holland and Powell (1998)	combination of Mahar et al. (1997) and Holland and Powell (1998)

NOTES: pure end-member phases include: albite (ab); andalusite (and); kyanite (ky); sillimanite (sill); quartz (q); rutile (ru); titanite (ttn)

see text for description of samples and corresponding chemical system

– not included

(a) compiled by RW White (08/01/08); provided at www.metamorph.geo.uni-mainz.de

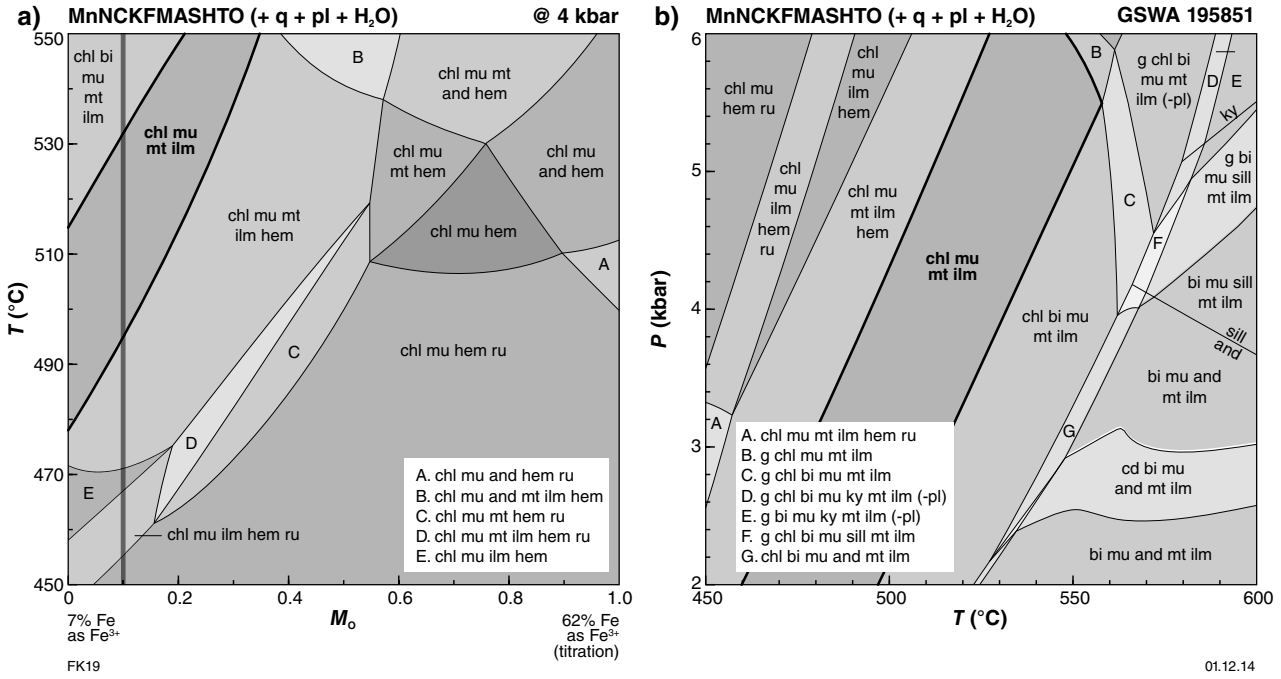

Figure 4.1 **Pseudosections for semipelitic schist from the Nick Belt (GSWA 195851): a) *T–M*$_O$ diagram constructed at 4 kbar. Peak field denoted by thicker lines. Grey bar indicates Fe^{3+} content used for subsequent modelling: b) *P–T* diagram**

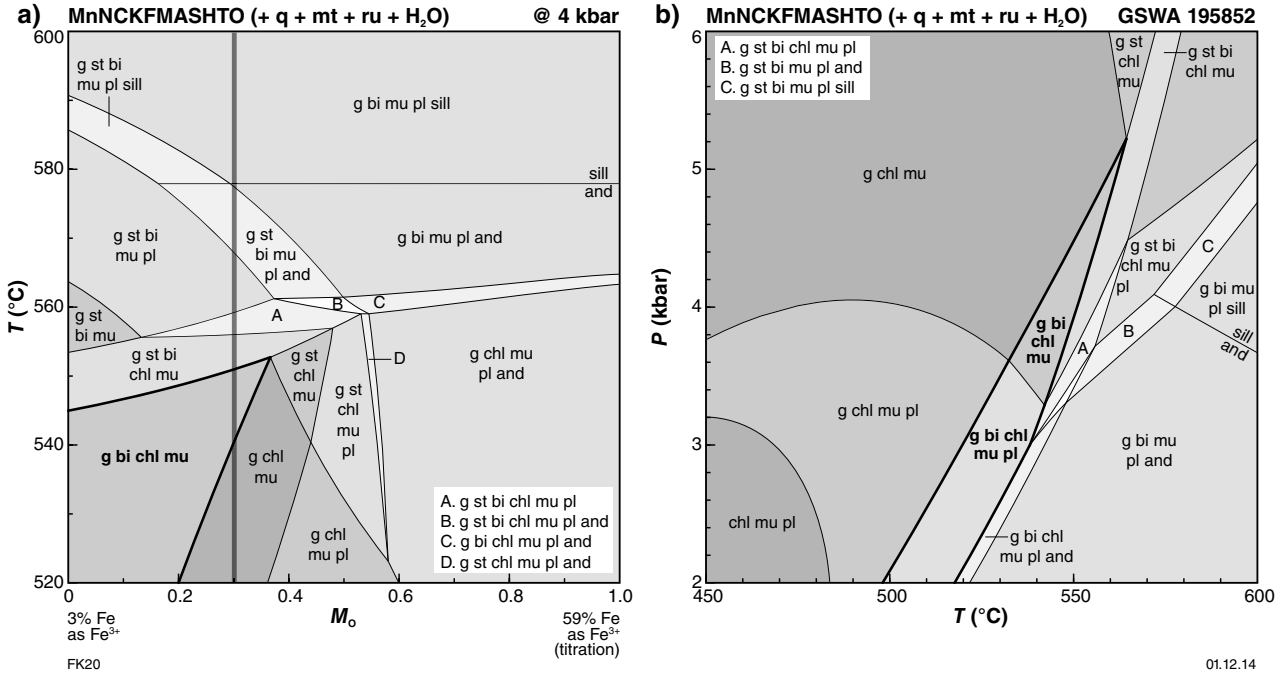

Figure 4.2 **Pseudosections for semipelitic schist from the Nick Belt (GSWA 195852): a) *T–M*$_O$ diagram constructed at 4 kbar. Peak fields (–plagioclase) denoted by thicker lines. Grey bar indicates Fe^{3+} content used for subsequent modelling; b) *P–T* diagram**

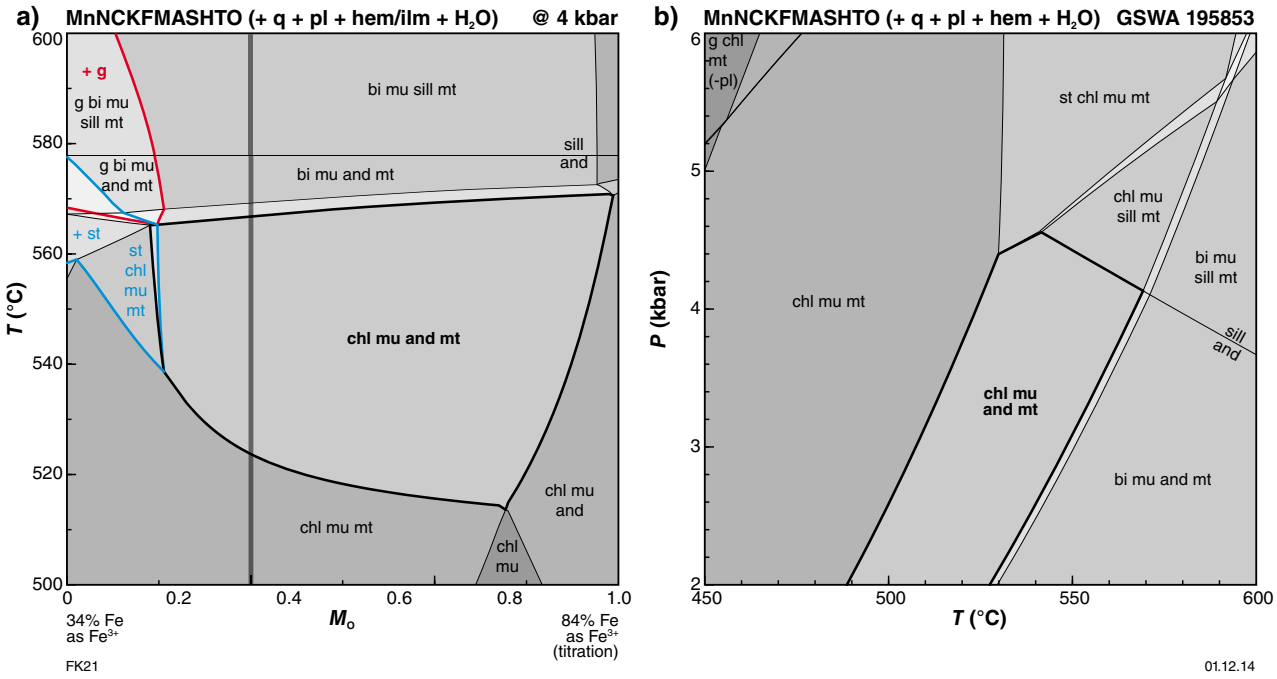

Figure 4.3 **Pseudosections for semipelitic schist from the Nick Belt (GSWA 195853): a) *T–M*$_O$ diagram constructed at 4 kbar. Peak field denoted by thicker lines. Grey bar indicates Fe^{3+} content used for subsequent modelling. Garnet-bearing fields are stable at lower Fe^{3+} contents (to the left of red lines); staurolite-bearing fields are stable at slightly lower temperatures (to the left of blue lines); b) *P–T* diagram**

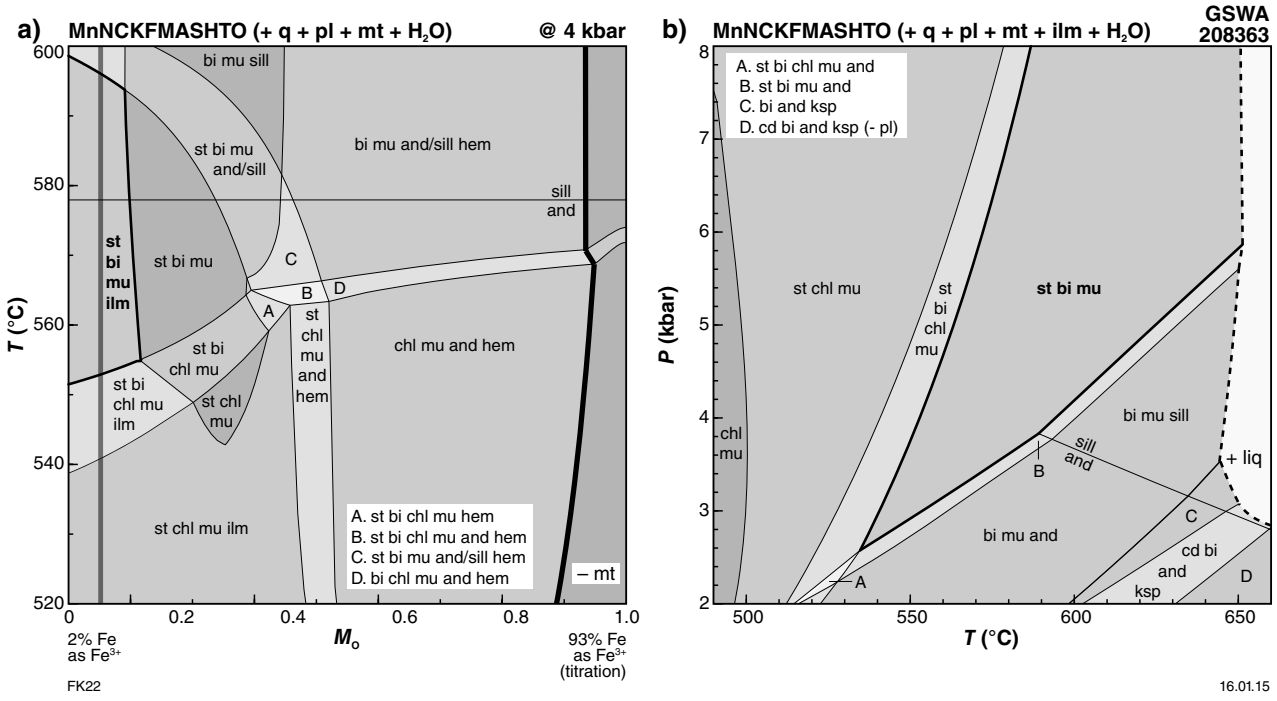

Figure 4.4 **Pseudosections for staurolite schist from the Nick Belt (GSWA 208363): a) *T–M*$_O$ diagram constructed at 4 kbar. Peak field denoted by thicker lines. Grey bar indicates Fe^{3+} content used for subsequent modelling. Magnetite is not stable at higher Fe^{3+} contents (to the right of heavy line, labelled '–mt'); b) *P–T* diagram. Solidus shown by heavy dashed line, labelled '+ liq'**

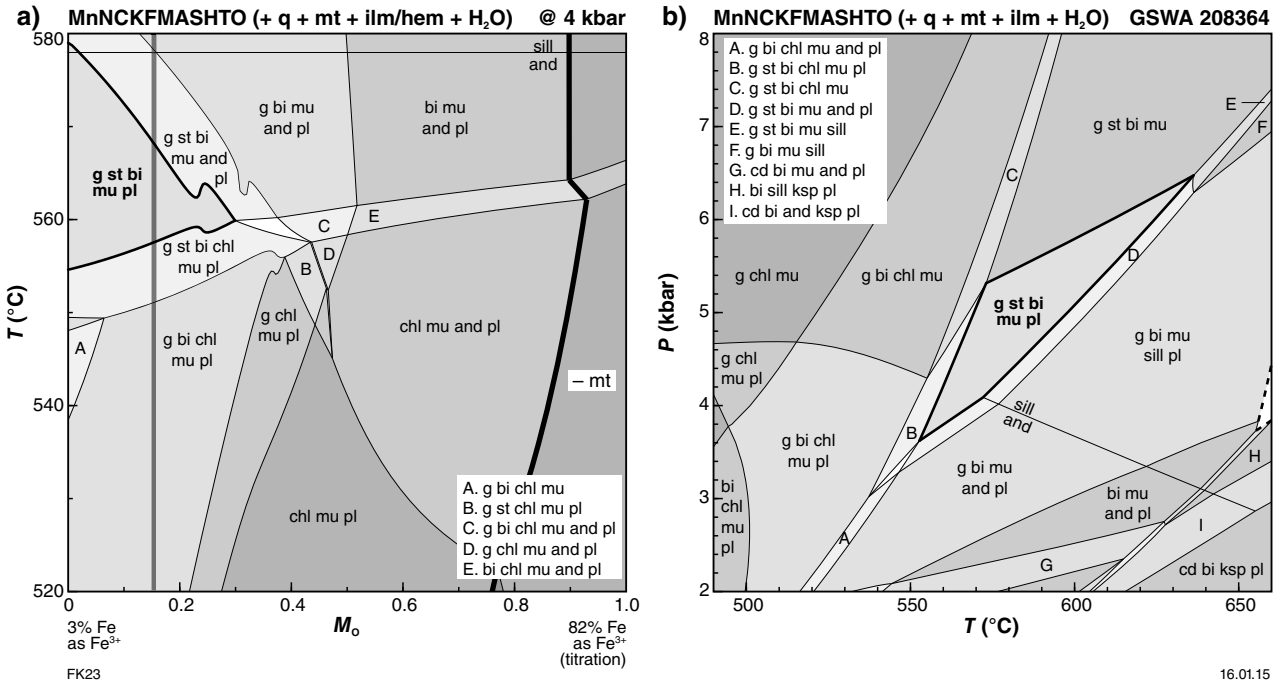

Figure 4.5 **Pseudosections for pelitic schist from the Nick Belt (GSWA 208364): a) *T–M*$_O$ diagram constructed at 4 kbar. Peak field denoted by thicker lines. Grey bar indicates Fe^{3+} content used for subsequent modelling. Magnetite is not stable at higher Fe^{3+} contents (to the right of heavy line, labelled '–mt'); b) *P–T* diagram. Solidus shown by heavy dashed line**

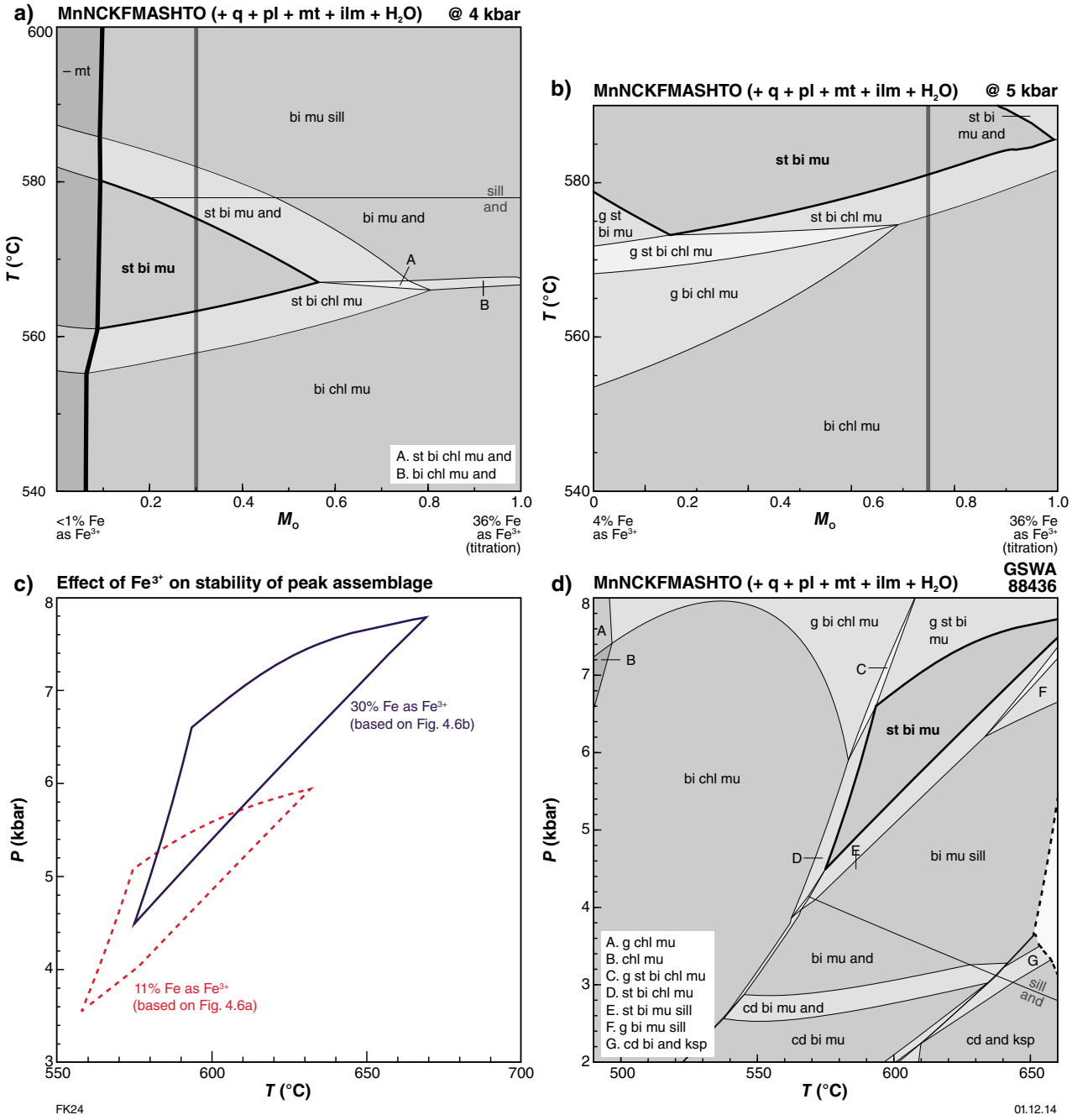

Figure 4.6 **Pseudosections for staurolite schist from Tommie Well (GSWA 88436): a) *T–M*$_O$ diagram constructed at 4 kbar. Peak field denoted by thicker lines. Grey bar indicates Fe^{3+} content used for subsequent modelling. Magnetite is not stable at lower Fe^{3+} contents (to the left of heavy line, labelled '–mt'); b) *T–M*$_O$ diagram constructed at 5 kbar; c) Variations in the stability of the field assemblage due to variations of Fe^{3+} content in the bulk composition; d) *P–T* diagram based on 30% Fe as Fe^{3+}. Solidus shown by heavy dashed line. See text for additional information**

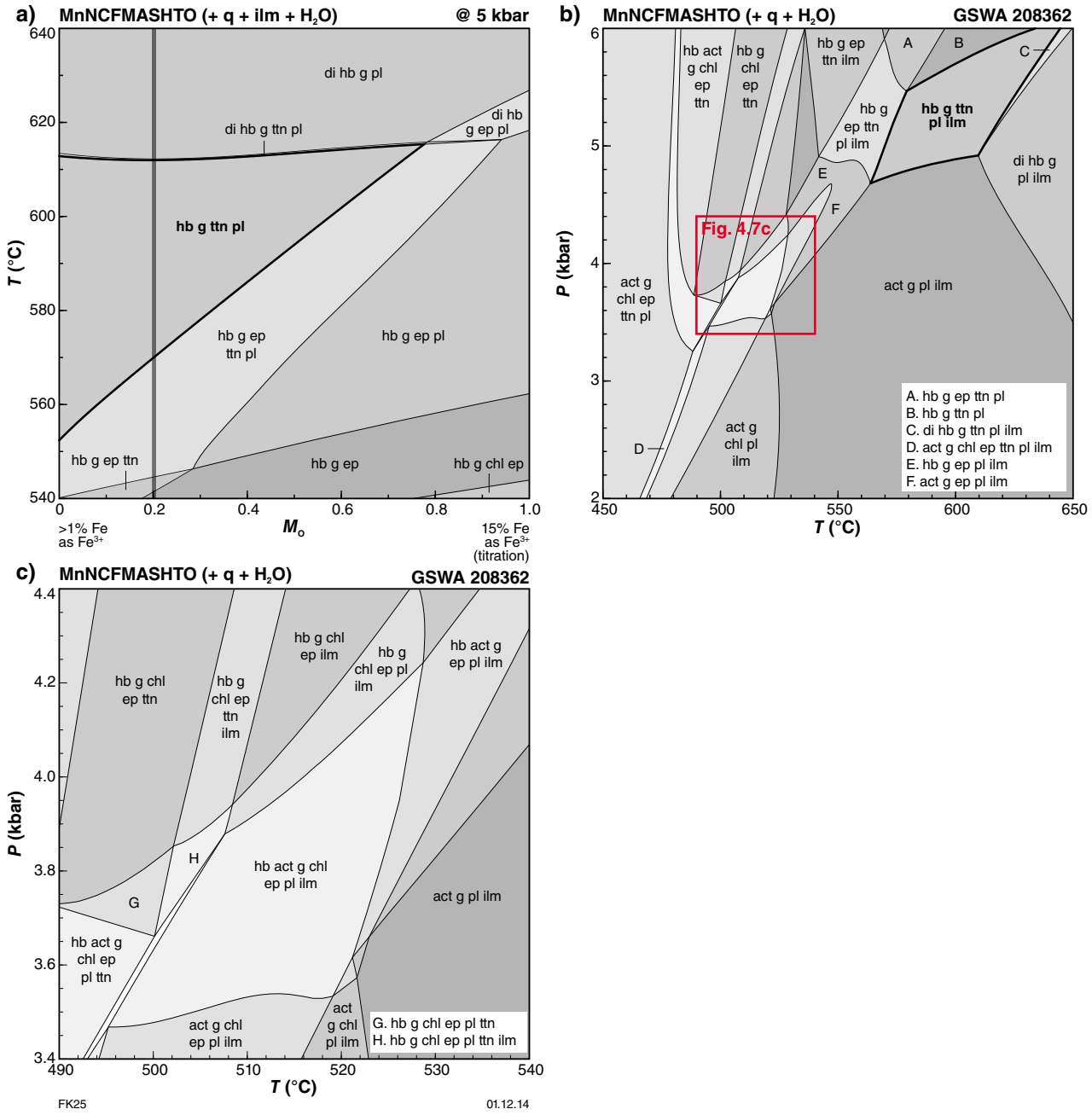

Figure 4.7 Pseudosections for garnet amphibolite from Tommie Well (GSWA 208362): a) T–M_O diagram constructed at 5 kbar. Peak field denoted by thicker lines. Grey bar indicates Fe^{3+} content used for subsequent modelling; b) P–T diagram; c) close-up of small fields from b)

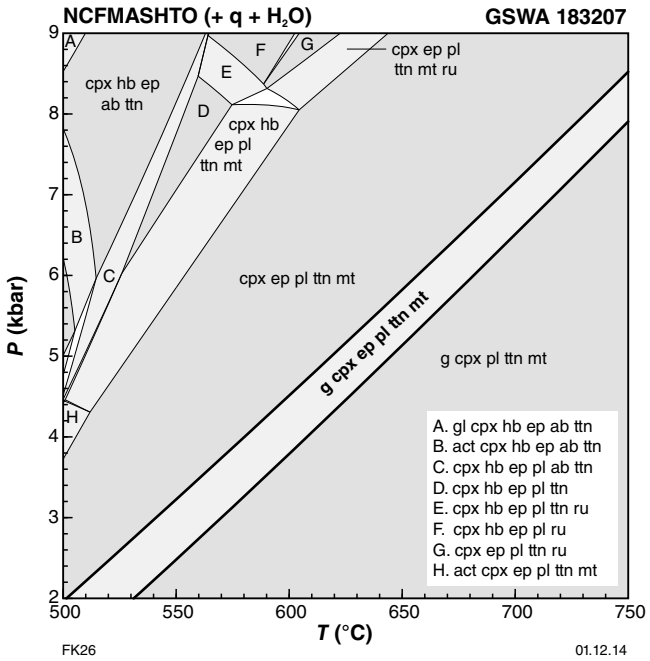

Figure 4.8 ***P–T*** **pseudosection for metamorphosed alkaline granite from New Well (GSWA 183207). Peak field denoted by thicker lines**

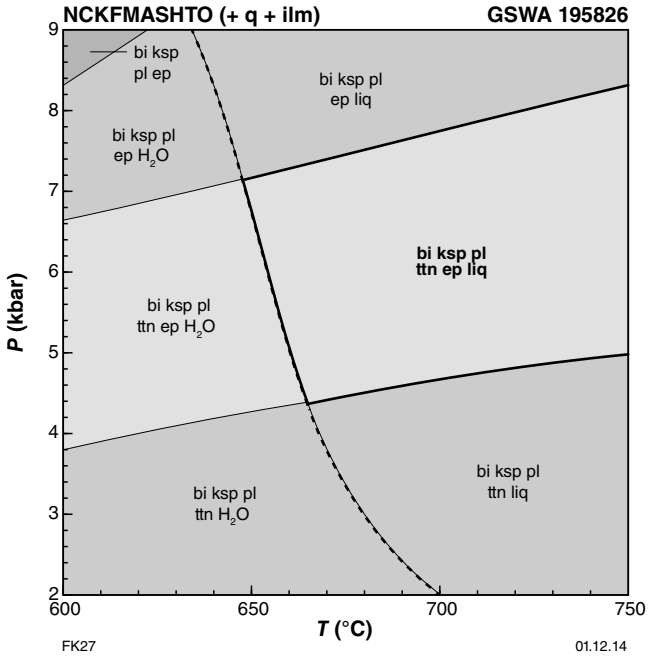

Figure 4.9 ***P–T*** **pseudosection for monzogranitic gneiss from McCarthy Well (GSWA 195826). Peak field denoted by thicker lines. Solidus shown by heavy dashed line**

Appendix 4 references

Coggon, R and Holland, TJB 2002, Mixing properties of phengitic micas and revised garnet-phengite thermobarometers: Journal of Metamorphic Geology, v. 20, no. 7, p. 683–696.

Diener, JFA, Powell, R, White, RW and Holland, TJB 2007, A new thermodynamic model for clino- and orthoamphiboles in the system Na_2O–CaO–FeO–MgO–Al_2O_3–SiO_2–H_2O–O: Journal of Metamorphic Geology, v. 25, no. 6, p. 631–656, doi:10.1111/j.1525-1314.2007.00720.x.

Green, E, Holland, TJB and Powell, R 2007, An order–disorder model for omphacitic pyroxenes in the system jadeite–diopside–hedenbergite–acmite, with applications to eclogitic rocks: American Mineralogist, v. 92, no. 7, p. 1181–1189.

Holland, TJB, Baker, J and Powell, R 1998, Mixing properties and activity-composition relationships of chlorites in the system MgO–FeO–Al_2O_3–SiO_2–H_2O: European Journal of Mineralogy, v. 10, no. 3, p. 395–406.

Holland, TJB and Powell, R 1998, An internally consistent thermodynamic data set for phases of petrological interest: Journal of Metamorphic Geology, v. 16, no. 3, p. 309–343.

Holland, TJB and Powell, R 2003, Activity–composition relations for phases in petrological calculations: an asymmetric multicomponent formulation: Contributions to Mineralogy and Petrology, v. 142, p. 492–501.

Mahar, EM, Baker, JM, Powell, R, Holland, TJB and Howell , N 1997, The effect of Mn on mineral stability in metapelites: Journal of Metamorphic Geology, v. 15, no. 2, p. 223–238.

White, RW, Pomroy, NE and Powell, R 2005, An in situ metatexite–diatexite transition in upper amphibolite facies rocks from Broken Hill, Australia: Journal of Metamorphic Geology, v. 23, no. 7, p. 579–602.

White, RW, Powell, R, Holland, TJB and Worley, BA 2000, The effect of TiO_2 and Fe_2O_3 on metapelitic assemblages at greenschist and amphibolite facies conditions: mineral equilibria calculations in the system K_2O–FeO–MgO–Al_2O_3–SiO_2–H_2O–TiO_2–Fe_2O_3: Journal of Metamorphic Geology, v. 18, no. 5, p. 497–511.

White, RW, Powell, R and Holland, TJB 2007, Progress relating to calculation of partial melting equilibria for metapelites: Journal of Metamorphic Geology, v. 25, no. 5, p. 511–527.

White, RW, Powell, R and Clarke, GL 2002, The interpretation of reaction textures in Fe-rich metapelitic granulites of the Musgrave Block, central Australia: constraints from mineral equilibria calculations in the system K_2O–FeO–MgO–Al_2O_3–SiO_2–H_2O–TiO_2–Fe_2O_3: Journal of Metamorphic Geology, v. 20, no. 1, p. 41–55.

This Report outlines the metamorphic, structural and temporal evolution of the Capricorn Orogen during the 1320–1170 Ma Mutherbukin Tectonic Event. This event represents a protracted period of intraplate reworking and offers significant insight into the tectonic drivers and heat sources during the evolution of long-lived intraplate orogens and their relationships with mineral systems.

Mineral assemblages and tectonic fabrics related to this event occur within a 50 km-wide fault-bound corridor in the central part of the Gascoyne Province. This zone preserves a crustal profile, with greenschist facies rocks in the north grading to upper amphibolite facies rocks in the south. Upper crustal rocks across the region also record evidence for faulting and hydrothermal fluid flow at this time, including zones of mineralization.

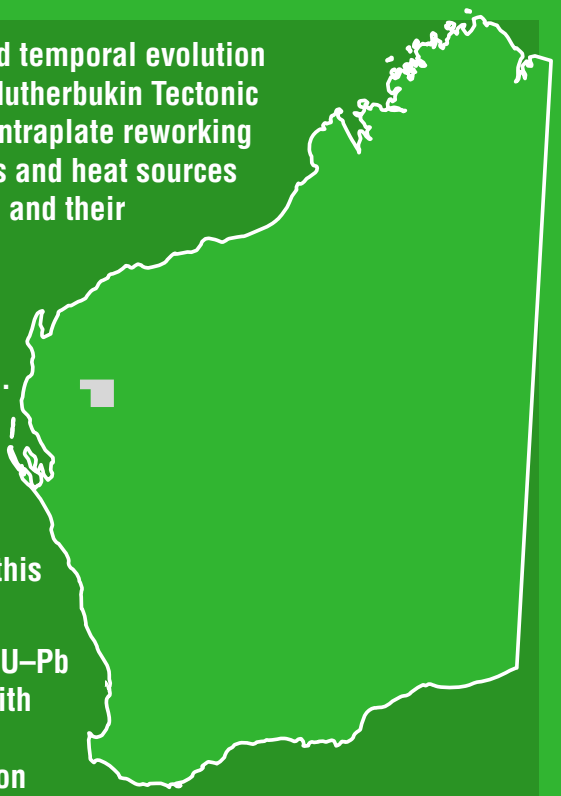

Sensitive high-resolution ion microprobe (SHRIMP) U–Pb dating of accessory phosphate phases, integrated with phase equilibria modelling and garnet chemistry, reveals a dominant history of prolonged transpression and crustal thickening between c. 1320 and 1270 Ma, followed by transtension and crustal thinning from c. 1210 to 1170 Ma. Fluid flow and hydrothermal alteration in the upper crust was synchronous with these deformation and metamorphic events, indicating a strong, dynamic link between events in the middle and upper crust. These relationships are critical for understanding mineral systems in the province and for constraining where and when mineral deposits might form.

Korhonen et al.

PRESSURE–TEMPERATURE–TIME EVOLUTION OF THE MUTHERBUKIN TECTONIC EVENT, CAPRICORN OROGEN

REPORT 146

Further details of geological products and maps produced by the Geological Survey of Western Australia are available from:

Information Centre
Department of Mines and Petroleum
100 Plain Street
EAST PERTH WA 6004
Phone: (08) 9222 3459 Fax: (08) 9222 3444

www.dmp.wa.gov.au/GSWApublications